Porous and Viscous Modeling of Cerebrospinal Fluid Flow in the Spinal Canal Associated with Syringomyelia

by

IDA NORDERHAUG DRØSDAL

THESIS

for the degree of

MASTER OF SCIENCE

(Master i Anvendt matematikk og mekanikk)

Faculty of Mathematics and Natural Sciences
University of Oslo

December 2011

Det matematisk- naturvitenskapelige fakultet
Universitetet i Oslo

Acknowledgements

This work would not have been possible without the help and support of others. My deepest gratitude goes to my supervisor, Kent-André Mardal, for all the guidance throughout this period, and for having an open door for questions and discussions whenever needed. Further thanks goes to co-supervisor, Karen-Helene Støverud; the help on medical background, porous flow modeling in the spinal cord and providing background literature has been very valuable. I would also like to thank Victor Haughton for sharing his knowledge on the medical problems, as well as helping me with my scientific writing.

Finally, I would like to thank my family, friends and boyfriend. ♡

List of Abbreviations

Medical

CM ..... Chiari Malformation

CSF ..... Cerebrospinal fluid

ISF ..... Interstitial fluid

MR ..... Magnetic resonance

MRI ..... Magnetic resonance imaging

PC-MRI ..... Phase-contrast magnetic resonance imaging

SAS ..... Subarachnoid space

Mathematical

BJS ..... Beavers-Joseph-Saffmann

CFD ..... Computational fluid dynamics

FEM ..... Finite element method(s)

IPCS ..... Incremental pressure correction scheme

PDE ..... Partial differential equation

REV ..... Representative elementary volume

UFL ..... Unified form language

Contents

Chapter 1

Introduction

Syringomyelia Associated with the Chiari Malformation

The Chiari Malformation is a medical condition characterized by a downwards displacement of the brain, causing part of the cerebellum to protrude into the spinal cavity. Among other clinical manifestations, a Chiari Malformation is frequently accompanied by fluid-filled spinal cord cysts—a condition known as syringomyelia. The cysts typically expand and strain the surrounding nerve tissue, potentially inflicting permanent damage to the central nervous system. Syringomyelia associated with the Chiari Malformation is not fully understood. The underlying mechanism of the cyst formation is unknown, and clinical signs distinguishing Chiari Malformations that lead to syringomyelia from those who do not is yet to be discovered.

Current theories relate the pathogenesis to a disruption of cerebrospinal fluid flow. Cerebrospinal fluid (CSF) resides in the subarachnoid space (SAS) surrounding the brain and spinal cord. It flows in an oscillating manner between the cranium and spinal canal, driven by the brain's expansion and contraction with the cardiac cycles. A Chiari Malformation obstructs this flow, hypothetically causing the formation of cysts. Several theories on the underlying mechanism have been proposed (e.g. Oldfield et al., 1994; Heiss et al., 1999; Levine, 2004; Greitz, 2006). There are essentially two different angles of approach. Theories either suggest a net CSF flow into the spinal cord, or some source of stress on the cord tissue followed by accumulation of excess fluid secreted from blood vessels within the cord.

Mathematical Modeling of Cerebrospinal Fluid Flow

Phase-contrast magnetic resonance imaging (PC-MRI), measuring flow velocities, is used to characterize abnormal CSF dynamics associated with the Chiari Malformation (e.g. Haughton et al., 2003; Quigley et al., 2004; Shah et al., 2011). However, this description is incomplete. Spatial and temporal resolution is poor, and imaging is limited to a few cross sections. Fur-

thermore, PC-MRI does not measure CSF pressure, possibly more directly related to cyst formation. Aimed at a more complete characterization, computational fluid dynamics (CFD) has been introduced. Models based on patient-specific computational geometries of the SAS have been created from high-resolution magnetic resonance images (Roldan et al., 2009; Gupta et al., 2009). These potentially provide full, three-dimensional descriptions of both velocity and pressure distributions in the SAS. Models based on idealized geometries have also been developed (Linge et al., 2010, 2011). Eliminating interindividual variations, these are used to study how changes in geometry affect CSF dynamics. Results from both patient-specific and idealized models agree well with typical flow characteristics measured by PC-MRI. However, only including the spinal cord as a rigid, impermeable structure, these models do not include deformations or flow within the cord tissue.

Strain on the spinal cord has been investigated in several studies by fluid-structure interaction models on simplified geometries (e.g. Carpenter et al., 2003; Bertram et al., 2005; Bertram, 2010). To our knowledge, fluid flow within the spinal cord tissue has been considered only in a few recent studies (e.g. Bilston et al., 2009; Støverud et al., 2011).

The Spinal Cord Central Canal

The central canal is a narrow channel in the spinal cord, only partly present in most adults. A recent study by Støverud et al. (2011) indicates this to have an important role in the pathogenesis of syringomyelia, redirecting excess fluid away from the level of the CSF obstruction.

Støverud et al. applied a poroelastic model to study deformations and fluid flow within the spinal cord, resulting from abnormal pressure distributions in the SAS. The spinal cord was modeled as a cylindrical poroelastic structure, the central canal represented by a narrow channel of high permeability; boundary conditions were set to resemble abnormal pressure gradients observed in patient-specific and idealized geometry models. With a homogeneous cord, increased inflow at the level of obstruction was balanced by a corresponding outwards flow. However, introducing a patent segment of the central canal, excess fluid at the level of obstruction was redirected downwards and accumulated in the area below, indicating the formation of a cyst.

The Present Study

In the present study, we aim to further investigate the role of the central canal by including a porous spinal cord in already existing patient-specific or idealized models of the SAS. In this respect, we develop a coupled viscous and porous model based on the Navier-Stokes/Darcy system; the spinal cord is considered a rigid porous medium saturated by the surrounding fluid in

the SAS, the central canal represented by a cavity in the porous tissue. Compared to the model used in the study of Støverud et al., this yields more realistic spinal cord geometries and a more accurate representation of pressure conditions on the spinal cord surface. However, because of the rigid representation, fluid cannot accumulate within the cord.

The model equations are solved by the finite element method, implemented using the FEniCS software package. Different numerical schemes are investigated. First, we develop a unified, mixed formulation, allowing for Taylor-Hood elements to be applied over the entire computational domain. Based on this formulation, we develop an incremental pressure correction scheme, decoupling the original system into separate equations for velocity and pressure. Finally, we consider a simpler strategy based on the Brinkman porous media model, enabling us to represent the porous cord by a discontinuous drag term added to the viscous equations; an incremental pressure correction scheme is applied on the governing equations. Small variations of the latter two schemes are made when searching for stable methods on initial flow simulation tests. Accuracy and convergence properties of the numerical schemes are investigated through numerical experiments by the method of manufactured solutions. Then the schemes are compared on a simple two-dimensional model, in order to conclude on which is the most appropriate for further investigations on realistic, three dimensional geometries.

The model equations include unknown parameters related to the porous media representation of spinal cord tissue. The importance of these parameters is investigated through tests on the two-dimensional model. We have not been able to apply the viscous and porous model on realistic, three dimensional geometries. However, some results are drawn from the simpler two-dimensional model—regarding how normal spinal canal dynamics are affected by the presence of a spinal cord cavity, representing a cyst or a patent segment of the central canal.

Outline

In chapter 2, necessary anatomical and physiological background is provided, and we give further introduction to the medical problem. The mathematical model is presented in chapter 3, together with a background on the model equations. In chapter 4, we give a short presentation of the finite element method and the FEniCS software package, and we present the applied numerical schemes. Numerical experiments on accuracy and convergence properties are presented in chapter 5. In chapter 6, investigations on the two-dimensional model are presented. Finally, discussion and conclusions are given in chapter 7.

Source code can be found at http://folk.uio.no/idand/. These are written for a development version following FEniCS 1.0.0.

Chapter 2

Medical Background

This chapter gives an introduction to the medical problem, as well as providing anatomical and physiological background for the applied mathematical model.

2.1 Anatomy and Physiology

2.1.1 The Spinal Cord

The brain and spinal cord comprises the central nervous system. Together with the peripheral nervous system, these integrate sensory information and control motor and cognitive functions. The spinal cord has a large role in reflexes and autonomic processes, but its primary function is to serve as a link between brain and body. Connected to the base of the brain, it extends caudally, about 40-50 cm, inside the vertebral column. Along the length of the cord, 31 pairs of nerves exit the cord laterally, conveying information to and from the different parts of the body. The spinal cord is organized into 31 segments, each corresponding to a nerve pair. These are in turn grouped into four regions: cervical, thoracic, lumbar and sacral (Fig. 2.1a).

Fig. 2.1b illustrates typical cross sections along the length of the spinal cord. The cord tissue consists of gray and white matter, differing mainly in the distribution of nerve cell bodies and fibers, and in the content of insulating myelin. In the figure, the butterfly-shape in the central area is gray matter, while the surrounding, lighter shade tissue is white matter. In the center of the cord is a narrow channel lined by a single layer of ependymal cells. This is referred to as the central canal. The central canal is fully intact at birth, but progressively occludes with age. To a varying extent, only parts remain in the spinal cords of adults (Milhorat et al., 1994; Yasui et al., 1999).

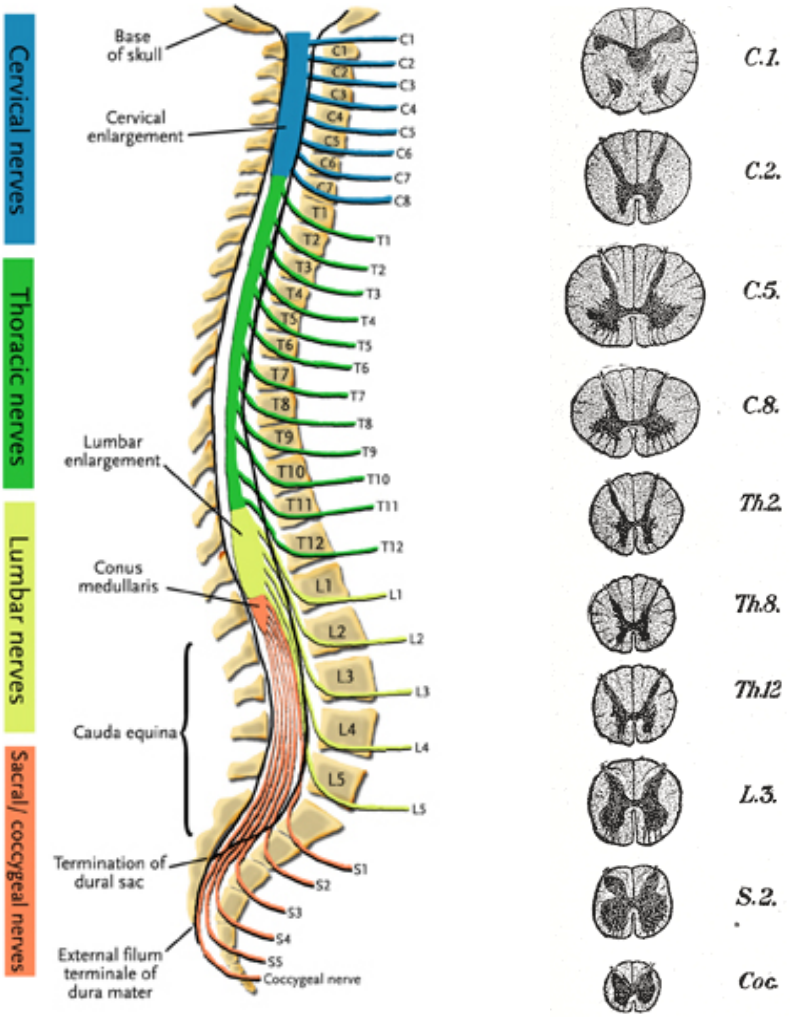

(a) Spinal cord longitudinal organization

(b) Spinal cord cross sections

Figure 2.1: Illustrations of the (a) longitudinal organization and (b) internal structure of the spinal cord. The spinal cord is divided into cervical, thoracic, lumbar and sacral regions. These are further organized into a total of 31 segments, corresponding to the 31 nerve pairs exiting the cord. In (b), illustrations of spinal cord cross sections are given at several longitudinal levels (Gray, 2000). Gray and white matter are depicted by darker and lighter gray, respectively.

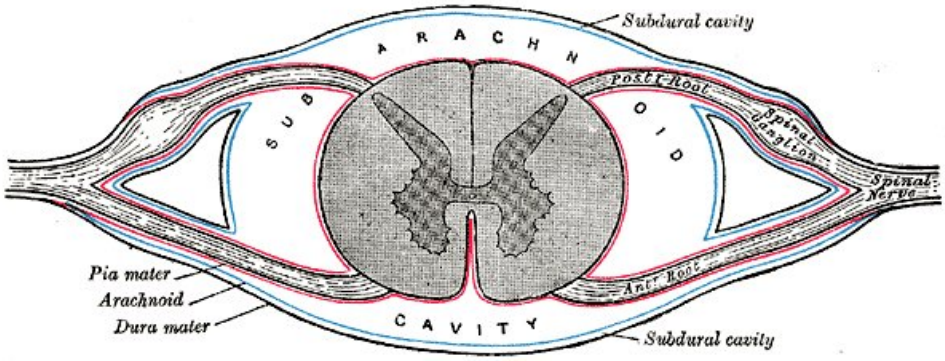

Figure 2.2: Cross section of the spinal canal (Gray, 2000). The illustration shows the spinal cord, nerves exiting the cord, the surrounding subarachnoid space and the protective tissue membranes: the dura mater, the arachnoid mater and the pia mater.

2.1.2 The Subarachnoid Space

The brain and spinal cord are contained within the skull and vertebral column, connected at an opening in the base of the skull known as the foramen magnum. Within this bony casing, the central nervous system is surrounded by fluid and several tissue membranes (Fig. 2.2). Adherent to the brain and spinal cord is a thin membrane called the pia mater. Outside the pia mater is a fluid-filled space traversed by connective tissue trabeculae; this has been named the subarachnoid space (SAS) after its enclosing membrane, the arachnoid mater. Lastly, between the arachnoid mater and the bone is a thick, protective membrane called the dura mater.

2.1.3 Cerebrospinal Fluid Flow

The fluid in the SAS, called cerebrospinal fluid (CSF), is composed of water and small amounts of protein, salts and sugars. It circulates in the SAS, being recycled several times a day due to secretion and absorption through blood vessel walls. This process occurs throughout the SAS, but the main production is in the choroid plexus of the brain.

Superimposed on the mean CSF flow is an oscillating component coupled to the cardiac cycles. With each heartbeat, the brain expands and contracts due to changes in contained blood volume. Since the skull is rigid, this is balanced by a corresponding flow of CSF between the cranial and spinal SAS. Thus, the effect is an oscillatory flow through the foramen magnum, as well as up and down the spinal canal. In the spinal canal, CSF dynamics is dominated by the oscillating component (Loth et al., 2001; Gupta et al., 2009).

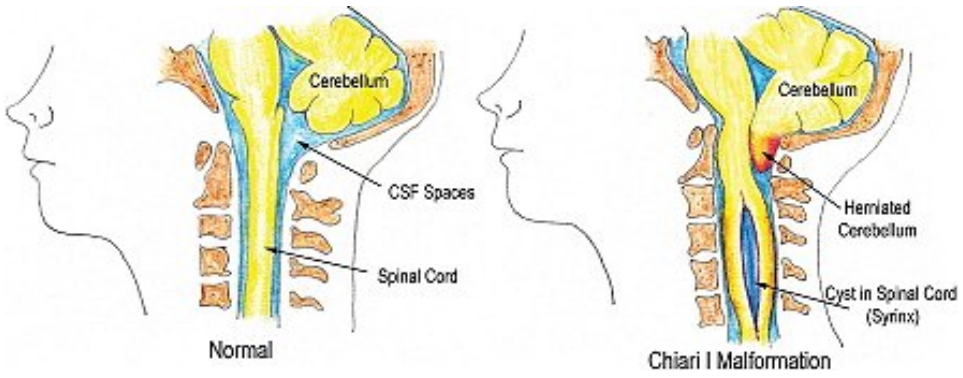

Figure 2.3: Illustration of the Chiari Malformation, depicting the brain, spinal cord and SAS of a healthy individual (left) and a Chiari subject (right) (http://www.chiariinstitute.com). The Chiari anatomy is characterized by the displacement of the cerebellar tonsils into the spinal canal. The illustration also includes a spinal cord cyst (syrinx), characteristic of syringomyelia (see Sec. 2.3).

2.2 The Chiari Malformation

The Chiari Malformation (CM) is a medical condition characterized by a herniation of the cerebellar tonsils into the spinal canal (Fig. 2.3). There are three primary types: CM1, CM2 and CM3—graded after severity of the malformation. CM1 is the simplest and most common form, traditionally defined to be a tonsilar herniation of at least 3 mm. CM2 and CM3 are associated with greater abnormalities.

Only about half of Chiari cases are symptomatic. However, when present, symptoms are many and varying. The most common is the 'Chiari headache', characterized by a pressure type pain in the back of the head which is usually triggered by straining activities, such as coughing, laughing, exercise and so on. Other common symptoms include neck pain, dizziness, numbness or weakness in arms and legs, and sleep apnea.

A Chiari Malformation obstructs the normal CSF flow through the foramen magnum. This is associated with several symptoms, and, as will be discussed in the following sections, is hypothetically the driving mechanism of cyst formation in syringomyelia. Abnormal CSF flow related to the Chiari Malformation has been confirmed by phase-contrast magnetic resonance imaging (PC-MRI) measuring flow velocities. Characteristic of Chiari are inhomogeneous flow, jets, regions with preferred flow direction, and synchronous bidirectional flow (e.g. Haughton et al., 2003; Quigley et al., 2004).

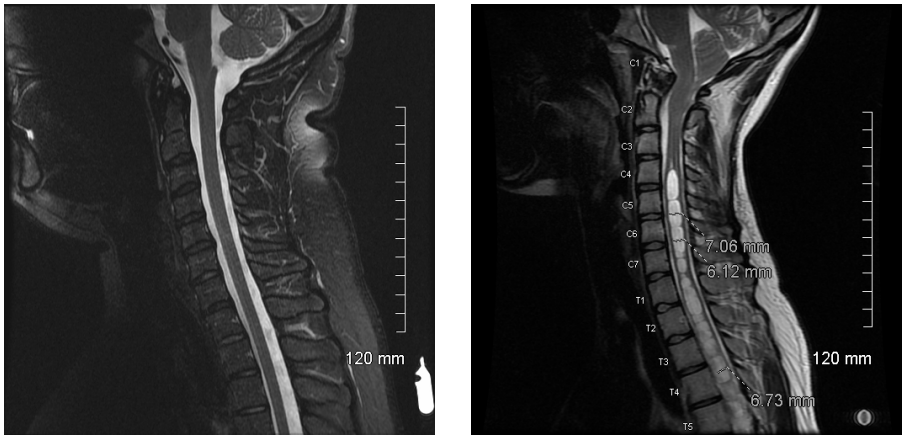

(a) Healthy MRI (b) MRI of syringomyelia

Figure 2.4: Magnetic resonance images (MRIs) showing sagittal cross sections of the neck area of (a) a healthy person and (b) a Chiari patient with syringomyelia. The tissue of the brain and spinal cord is seen in gray, while the fluid in the SAS and syrinx is seen in white.

2.3 Syringomyelia

The Chiari Malformation is frequently accompanied by syringomyelia: fluid-filled cysts (syrinxes) within the spinal cord (see Fig. 2.3 and 2.4). Syrinxes usually form in the central canal of the cervical cord, either isolated from or including the adjacent tissue. They typically expand—straining and damaging the surrounding nerve tissue. Symptoms specific to syringomyelia are weakness and sensory loss in arms and legs, pain in the neck and upper back, bladder and bowel problems, and inability to regulate body temperature. As with Chiari, symptoms vary, and there are even cases where a syrinx causes no symptoms.

2.4 Theories on the Pathogenesis of Syringomyelia

The pathogenesis of syringomyelia associated with the Chiari Malformation is unknown. Current theories relate cyst formation to abnormal CSF flow caused by the malformation. However, there is a wide range of hypotheses on the underlying mechanism. These can be divided into two main groups, differing by what is believed to be the source of the syrinx fluid. The first propose a net CSF flow into the spinal cord. The second suggest some source of stress on the cord, causing excess secretion from blood vessels within the cord. In the following, we summarize a few recently developed theories.

2.4.1 The Piston Theory

Oldfield et al. (1994) measured tonsilar movement in Chiari patients and observed a sharp downward movement with the CSF flow from cranial to spinal SAS. Based on this, it is theorized that the tonsils act like a piston, increasing CSF pressure waves and driving CSF into the spinal cord (Oldfield et al., 1994; Heiss et al., 1999).

Recent PC-MR investigations indicate that the observations done by Oldfield might be erroneous. The piston-like movement was observed during surgery, possibly affecting the results. The PC-MR studies indicate that tonsilar movement is small and, furthermore, not enhanced in Chiari subjects compared to normals (Cousins and Haughton, 2009).

2.4.2 The Venous Congestion Theory

Levine (2004) propose that, under certain conditions, the obstruction at the foramen magnum causes transient abrupt changes in CSF pressure across the obstruction; this could occur with the oscillatory flow coupled to the cardiac cycles, straining activities or assuming an erect position. The venous pressure inside the cord, however, is assumed unaltered by the malformation. Hypothetically, this causes an uneven expansion and contraction of blood vessels within the cord which, over time, inflicts damage on the cord tissue. The syrinx results from accumulation of excess fluid secreted through the blood vessel walls.

2.4.3 The Intramedullary Pulse Pressure Theory

Greitz (2006) suggests that increased velocities in the narrowed part of the SAS causes a venturi effect which distends the spinal cord. The resulting stress on the cord tissue causes an increased secretion from blood vessels within the cord, leading to the accumulation of excess fluid forming a syrinx. The distension leads to a further narrowing of the SAS and an increased venturi effect, causing progression of the syrinx.

Chapter 3

Mathematical Model

We model CSF dynamics in the spinal canal by a porous and viscous flow governed by the coupled Navier-Stokes/Darcy system. The spinal cord tissue is considered a rigid porous medium, saturated by the fluid of the surrounding SAS. Syrinxes or patent segments of the central canal are represented by cavities in the porous tissue.

In this chapter we first give an introduction to the Navier-Stokes equations and Darcy's law, as well as necessary coupling conditions at interfaces between porous and viscous domains. Then, a coupled porous and viscous model of spinal canal flow is presented.

3.1 Viscous Flow

Flow in the SAS and in spinal cord cavities is described by the incompressible Navier-Stokes equations for Newtonian fluids. A presentation of the equations, their scope, and a short derivation is given in the following.

3.1.1 The Navier-Stokes Equations

Incompressible, viscous fluid flow is described by the incompressible Navier-Stokes equations:

$$\rho\left(\frac{\partial \boldsymbol{u}}{\partial t} + \boldsymbol{u}\cdot\boldsymbol{\nabla}\boldsymbol{u}\right) = \boldsymbol{\nabla}\cdot\sigma(\boldsymbol{u},p) + \boldsymbol{f} \tag{3.1}$$

$$\boldsymbol{\nabla}\cdot\boldsymbol{u} = 0. \tag{3.2}$$

The quantities of interest are the velocity field, $\boldsymbol{u}$, and pressure field, p. The tensor, $\sigma(\boldsymbol{u},p)$, is the Cauchy stress tensor for a Newtonian fluid, given by

$$\sigma(\boldsymbol{u}) = 2\mu\epsilon(\boldsymbol{u}) - p\mathbb{I}, \tag{3.3}$$

where $\epsilon(\boldsymbol{u})$ is the symmetric strain rate tensor,

$$\epsilon(\boldsymbol{u}) = \frac{1}{2}\left(\boldsymbol{\nabla}\boldsymbol{u} + (\boldsymbol{\nabla}\boldsymbol{u})^T\right). \tag{3.4}$$

Fluid density and viscosity are given by ρ and μ, respectively, and $\boldsymbol{f}$ denotes volume forces. Eq. 3.1 originates from conservation of momentum and is, thus, referred to as the *equation of motion*. Eq. 3.2, accounting for conservation of mass, is referred to as the *equation of continuity*.

The Navier-Stokes equations govern Newtonian fluid flow. A Newtonian fluid is an isotropic, viscous fluid in which strain rates are proportional to viscous stress. This is an idealization, but common real fluids are approximated well by Newtonian fluids. In particular, this is valid for water, and thus also for CSF which has similar properties. The second approximation made is that of an incompressible fluid. In the context of single-phase flow, which is what we will consider, incompressibility means a constant fluid density. Again, this is a fairly good approximation for most real fluids.

3.1.2 Derivation of the Navier-Stokes Equations

The Navier-Stokes equations are derived in most fluid mechanics text books (e.g. White, 2008). However, a short derivation is given in the following as this provides a more thorough background on the mathematical model.

Fluid flow is governed by four basic conservation laws, stating the conservation of mass, linear and angular momentum, and energy. These are in turn supplemented by equations of state, relating thermodynamic properties. The nature of the problem to be solved determines which relations are needed. In this case, we are only interested in conservation of linear momentum and mass which, combined with the assumption of a Newtonian fluid, yields the Navier-Stokes equations.

The Reynolds Transport Theorem

The basic conservation laws describe changes in system quantities in interaction with the surroundings. The *Reynolds transport theorem* provides a means of converting these laws into ones governing spatial fields, relating changes in system quantities to integrals over a fixed *control volume*.

Let B be some fluid property and $\beta = \frac{\mathrm{d}B}{\mathrm{d}m}$ the amount of this quantity per unit mass. The Reynolds transport theorem states that (White, 2008, Eq. 3.12)

$$\frac{\mathrm{d}B_{\mathrm{syst}}}{\mathrm{d}t} = \int_{\mathrm{CV}} \frac{\partial}{\partial t}(\rho\beta)\,\mathrm{d}V + \int_{\mathrm{CS}} \rho\beta\boldsymbol{u}\cdot\hat{\boldsymbol{n}}\,\mathrm{d}S, \tag{3.5}$$

where CV and CS refer to the control volume and its surface, and $\hat{\boldsymbol{n}}$ is the outward unit normal vector. Expressed in words, the Reynolds transport theorem states that changes in the quantity, B, within the control volume, equals the change in the corresponding system quantity, B_{syst}, plus the flow through the control volume surface (Fig. 3.1).

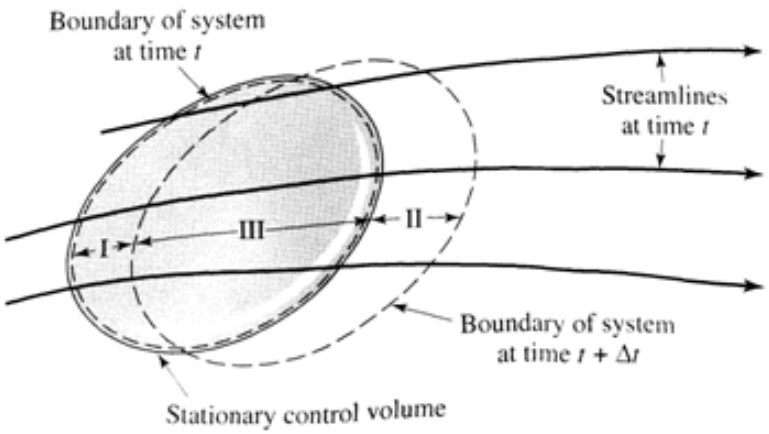

Figure 3.1: Illustration of the Reynolds transport theorem. (University of Pittsburgh, http://pillars.che.pitt.edu/). Changes in a quantity, B, within the control volume are caused by changes in the corresponding system quantity, B_{syst}, and flux through the control volume surface.

When deriving the governing equations, it is constructive to apply Gauss's divergence theorem and rewrite Eq. 3.5 as a pure volume integral:

$$\frac{\mathrm{d}B_{\text{syst}}}{\mathrm{d}t} = \int_{\text{CV}} \left(\frac{\partial}{\partial t}(\rho\beta) + \boldsymbol{\nabla} \cdot (\rho\beta \boldsymbol{u}) \right) \mathrm{d}V. \tag{3.6}$$

Conservation of Mass

By definition, the system mass is constant:

$$\frac{\mathrm{d}m_{\text{syst}}}{\mathrm{d}t} = 0. \tag{3.7}$$

Applying the Reynolds transport theorem (Eq. 3.6) with $B = m$ and $\beta = 1$, yields the mass balance law in integral form:

$$\int_{\text{CV}} \left(\frac{\partial \rho}{\partial t} + \boldsymbol{\nabla} \cdot (\rho \boldsymbol{u}) \right) \mathrm{d}V = 0. \tag{3.8}$$

For this to be valid for arbitrary control volumes the argument inside the integral must vanish, and we are left with

$$\frac{\partial \rho}{\partial t} + \boldsymbol{\nabla} \cdot (\rho \boldsymbol{u}) = 0, \tag{3.9}$$

which is the general equation of continuity. In the present study we are only interested in *incompressible* flow. A constant density, ρ, yields

$$\boldsymbol{\nabla} \cdot \boldsymbol{u} = 0, \tag{3.10}$$

which equals the equation of continuity for incompressible fluids as given in Eq. 3.2.

Conservation of Linear Momentum

Newton's second law states that the rate of change in system momentum, $\boldsymbol{p}_{\text{syst}}$, equals the net force, $\boldsymbol{F}$, exerted on the system,

$$\frac{\mathrm{d}\boldsymbol{p}_{\text{syst}}}{\mathrm{d}t} = \boldsymbol{F}. \tag{3.11}$$

Inserting $B = \boldsymbol{p} = m\boldsymbol{u}$ and $\beta = \boldsymbol{u}$ in the Reynolds transport theorem (Eq. 3.6) yields one equation for each component of $\boldsymbol{p}_{\text{syst}}$,

$$\frac{\mathrm{d}\boldsymbol{p}_{\text{syst}}}{\mathrm{d}t} = \int_{\text{CV}} \left(\frac{\partial}{\partial t}(\rho \boldsymbol{u}) + \boldsymbol{\nabla} \cdot (\rho \boldsymbol{u}\boldsymbol{u}) \right) \mathrm{d}V. \tag{3.12}$$

Forces on the system are of two types: stress, acting on the system surface, or volume forces (e.g. gravity or inertial forces). Denoting volume forces by $\boldsymbol{f}$ and introducing the Cauchy stress tensor, σ, these are expressed as

$$\begin{aligned} \boldsymbol{F} &= \int_{\text{CS}} \sigma \cdot \hat{\boldsymbol{n}} \, \mathrm{d}S + \int_{\text{CV}} \boldsymbol{f} \, \mathrm{d}V \\ &= \int_{\text{CV}} (\boldsymbol{\nabla} \cdot \sigma + \boldsymbol{f}) \, \mathrm{d}V, \end{aligned} \tag{3.13}$$

where the last step follows from Gauss's divergence theorem.

Inserting Eqs. 3.12 and 3.13 in Newton's second law and demanding the resulting integral statement to be valid for arbitrary control volumes, we get

$$\frac{\partial}{\partial t}(\rho \boldsymbol{u}) + \boldsymbol{\nabla} \cdot (\rho \boldsymbol{u}\boldsymbol{u}) = \boldsymbol{\nabla} \cdot \sigma + \boldsymbol{f}. \tag{3.14}$$

By use of the general equation of continuity (Eq. 3.9), this can be rewritten as

$$\rho \left(\frac{\partial \boldsymbol{u}}{\partial t} + \boldsymbol{u} \cdot \boldsymbol{\nabla} \boldsymbol{u} \right) = \boldsymbol{\nabla} \cdot \sigma(\boldsymbol{u}, p) + \boldsymbol{f}, \tag{3.15}$$

which is the equation of motion as given in Eq. 3.1.

Newtonian Fluids

For the complete equation of motion, it remains to derive the Cauchy stress tensor for a Newtonian fluid (Eq. 3.3). In the following, index notation and the Einstein summation convention is applied.

A Newtonian fluid is an isotropic, viscous fluid in which stress is linear with respect to strain rates. Quantitatively, this can be expressed as

$$\sigma_{ij} = -p\delta_{ij} + A_{ijkl} \nabla_k u_l, \tag{3.16}$$

where $\nabla_k u_l$ contains the strain rates and A_{ijkl} is an isotropic, rank 4 coefficient tensor. The term $-p\delta_{ij}$ represents pressure, which is a compression stress present in all fluids irrespective of relative velocities.

Isotropy means that the fluid properties are independent of direction, implying that the governing laws must be independent of the coordinate axes in which they are expressed. A general isotropic tensor of rank 4 can be expressed as

$$A_{ijkl} = \lambda\delta_{ij}\delta_{kl} + \mu(\delta_{ik}\delta_{jl} + \delta_{il}\delta_{jk}) + \nu(\delta_{ik}\delta_{jl} - \delta_{il}\delta_{jk}), \tag{3.17}$$

where δ_{ij} is the Kronecker delta and λ, μ and ν are arbitrary coefficients. Inserted into Eq. 3.16, this yields

$$\sigma_{ij} = -p\delta_{ij} + \lambda\delta_{ij}\nabla_k u_k + \mu(\nabla_i u_j + \nabla_j u_i) + \nu(\nabla_i u_j - \nabla_j u_i). \tag{3.18}$$

It can be shown that the antisymmetric part of the strain rate tensor corresponds to pure rotation. Causing no relative movement, this cannot contribute to viscous stress, and ν must be zero. Furthermore, $\nabla_k u_k = 0$, because of the incompressibility constraint. Thus,

$$\sigma_{ij} = -p\delta_{ij} + 2\mu\epsilon_{ij}, \tag{3.19}$$

where

$$\epsilon_{ij} = \frac{1}{2}\left(\nabla_i u_j + \nabla_j u_i\right), \tag{3.20}$$

is the symmetric strain rate tensor. The coefficient, μ, is defined as the viscosity, and we are left with the Cauchy stress tensor for a Newtonian fluid as given in Eq. 3.3.

3.2 Porous Media Flow

Flow through the spinal cord tissue is described by a non-stationary Darcy's law, combined with the porous media equation of continuity. In this section, the applied equations are presented. Then a short background is given on the principles of porous media flow modeling, describing how the governing equations are related to the more general Navier-Stokes equations. Finally, the validity of the non-stationary extension of Darcy's law is discussed.

3.2.1 Darcy's Law

Incompressible porous media flow is described by Darcy's law,

$$\boldsymbol{u} = -\frac{K}{\mu}\boldsymbol{\nabla} p, \tag{3.21}$$

combined with the porous media analogue of the incompressible equation of continuity,

$$\boldsymbol{\nabla}\cdot\boldsymbol{u} = 0. \tag{3.22}$$

Darcy's law is the equation of motion for porous media flow. It states that volumetric flux, $\boldsymbol{u}$ (commonly referred to as the *Darcy velocity*), is proportional to the pressure gradient, $\boldsymbol{\nabla} p$. K denotes permeability; this is a material property, quantifying how easily fluids are transmitted through a porous medium. As for viscous flow, μ denotes fluid viscosity. Darcy's law is valid for low Reynolds number porous media flow.

Non-stationary Extension

Darcy's law is valid for stationary and quasi-stationary flow, and most applications are of this kind. In this work we consider a non-stationary extension, including an inertial term (Nield and Bejan, 2006, eq. 1.9):

$$\frac{\rho}{\phi}\frac{\partial \boldsymbol{u}}{\partial t} = -\boldsymbol{\nabla} p - \frac{\mu}{K}\boldsymbol{u}, \tag{3.23}$$

where ρ is the fluid density and ϕ denotes porosity, defined as the fraction of void space in the porous medium. The literature on non-stationary porous media flow is sparse, and the validity of this extension is uncertain. This issue is discussed in Sec. 3.2.3.

3.2.2 Principles of Porous Media Flow Modeling

Porous media flow is described by space-averaged (macroscopic) quantities. A porous medium is a solid with an interconnected void, allowing fluid to pass through the material. A natural porous medium contains a large, irregular network of pores, and thus also a highly complex flow. Obtaining a detailed description of the full flow field is in practice impossible. Furthermore, gross features are usually of greater interest.

Fluid flow through a porous medium follows the same principles as free viscous flow, and the governing equations can be derived from the Navier-Stokes equations through space-averaging (see e.g. Whitaker, 1986). The complex porous structure is represented by a simple continuous medium, characterized by a few macroscopic properties. This is done by averaging over *representative elementary volumes* (REVs) throughout the flow domain, taking each average as the macroscopic value in the centroid of the corresponding REV (Fig. 3.2). The REV must be large compared to the pore scale and small compared to the overall flow domain. The first condition ensures a proper average, while the second justifies a continuum description.

3.2.3 Comment on the Inertial Term in the Non-Stationary Extension of Darcy's Law

The inertial term added to Darcy's law origins from the corresponding inertial term in the Navier-Stokes equations. Nield and Bejan (2006, Sec. 1.5)

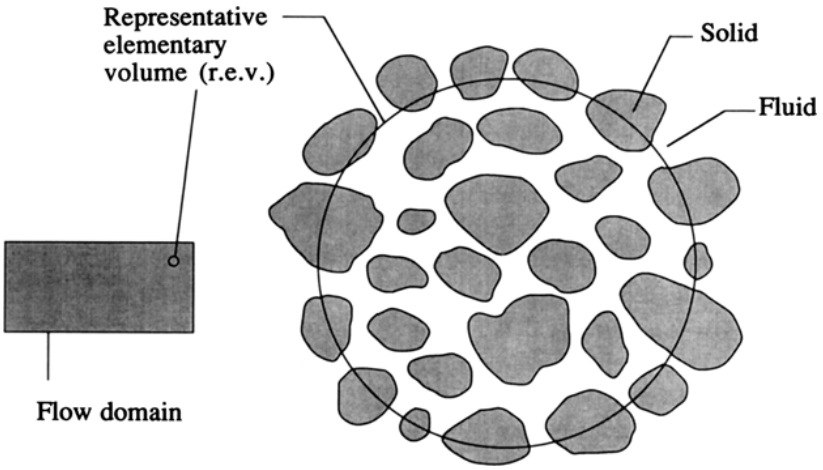

Figure 3.2: Illustration of the space-averaging procedure for creating a continuum description of a porous structure (Nield and Bejan, 2006). Averages are taken over representative elementary volumes (REVs) throughout the flow domain. Each average is taken as the macroscopic value in the centroid of the corresponding REV. The REV scale must be small compared to the overall flow domain, and large compared to the pore scale.

discuss the validity of this extension. Deriving this form, it is assumed that the partial derivative with respect to time permutes with the volume average, but in general this is not valid. Nield and Bejan propose replacing Eq. 3.23 by

$$\rho c_a \frac{\partial \boldsymbol{u}}{\partial t} = -\boldsymbol{\nabla} p - \frac{\mu}{K}\boldsymbol{u}, \tag{3.24}$$

where c_a, called the acceleration coefficient tensor, depends sensitively on the geometry of the porous medium. It is argued, however, that the inertial term usually is small and can be discarded.

Since we consider flow that is periodic in time, neglecting the inertial term could lead to significant errors (Philip, 1956). We therefore keep this term, working with the extended version of Darcy's law. As we have no measure of the acceleration coefficient tensor for spinal cord tissue, we use the form in Eq. 3.23. The importance of the inertial term and the acceleration coefficient tensor in spinal canal flow modeling is investigated (Sec. 6.3).

3.3 Coupling of Viscous and Porous flow

Viscous and porous domains are coupled at the interfaces by conservation of mass, continuity of normal stress and the Beavers-Joseph-Saffman (BJS)

condition (Beavers and Joseph, 1967; Saffman, 1973):

$$\boldsymbol{u}_{\mathrm{v}} \cdot \hat{\boldsymbol{n}} = \boldsymbol{u}_{\mathrm{p}} \cdot \hat{\boldsymbol{n}}, \tag{3.25}$$

$$2\mu \hat{\boldsymbol{n}} \cdot \epsilon(\boldsymbol{u}_{\mathrm{v}}) \cdot \hat{\boldsymbol{n}} - p_{\mathrm{v}} = -p_{\mathrm{p}}, \tag{3.26}$$

$$2\hat{\boldsymbol{n}} \cdot \varepsilon(\boldsymbol{u}_{\mathrm{v}}) \cdot \hat{\boldsymbol{\tau}} = \alpha K^{-1/2} \boldsymbol{u}_{\mathrm{v}} \cdot \hat{\boldsymbol{\tau}}. \tag{3.27}$$

Subscripts v and p denote viscous and porous quantities, respectively; $\hat{\boldsymbol{n}}$ is the unit normal vector and $\hat{\boldsymbol{\tau}}$ the unit tangent vector at the interface. The normal vector is defined to point out of the porous domain. The quantity α in the BJS condition is a dimensionless parameter determined by the structure near the interface of the porous medium.

3.4 Spinal Canal Flow Model

We present a coupled viscous and porous model of spinal canal CSF flow based on the coupled Navier-Stokes/Darcy system introduced in sections 3.1–3.3. The spinal cord is considered a rigid porous medium saturated by the fluid of the surrounding SAS. Fluid-filled cavities can be included in the porous tissue, representing a patent segment of the central canal or a syrinx. The SAS is treated as a free space. Thus, drag from the SAS trabeculae and the effects of traversing nerve fibers are neglected.

3.4.1 Cerebrospinal Fluid Properties

CSF has properties similar to water and is approximated well by a Newtonian fluid (Bloomfield et al., 1998). In the model equations we apply the density and viscosity of water at 37°C.

3.4.2 Porous Media Representation of Spinal Cord Tissue

The spinal cord can be considered a viscoelastic, porous medium (e.g. Nicholson, 2001; Cheng et al., 2008). In between the cells are narrow, fluid-filled spaces comprising what is referred to as the extracellular space (Fig. 3.3). This allows fluid flow through the spinal cord tissue, and, as the extracellular space is continuously connected to the SAS, flow between the SAS and spinal cord. Fluid inside the extracellular space, although mixing with CSF, is referred to as interstitial fluid (ISF).

We neglect viscoelasticity, treating the spinal cord tissue as a rigid, porous structure. The extracellular space takes up about 20% of the total volume of the spinal cord tissue, yielding a porosity of 0.2 (Nicholson, 2001). The permeability of spinal cord tissue is low. Several studies use a higher permeability of white matter compared to gray (e.g. Kaczmarek et al., 1997), but to our knowledge, this has not been measured. We use a uniform

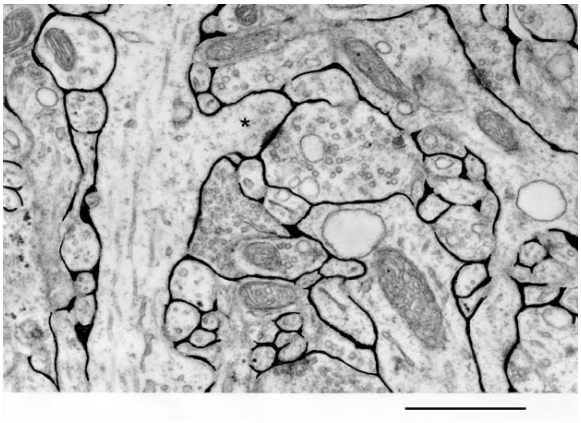

Figure 3.3: Electron micrograph of gray matter in a rat cerebral cortex (Nicholson, 2001). The black areas depict fluid filling the extracellular space. The scale bar under the figure represents a distance of about 1 μm.

CSF parameter values:	
Mass density, ρ [kg/m^3]	1.0×10^3
Dynamic viscosity, μ [kg/(m-s)]	7.0×10^{-4}

Spinal cord parameter values:	
Porosity, ϕ	0.2
Permeability, K [m^2]	1.4×10^{-15}
BJS interface parameter, α	1
Acceleration coefficient tensor, c_a	$1/\phi$

Table 3.1: Parameter values applied in the model equations.

permeability of 1.4×10^{-15} m^2, proposed by Smith and Humphrey (2007). The effect of the pia mater enveloping the cord is neglected.

To our knowledge, there are no measurements of the BJS structural parameter, α, or the acceleration coefficient tensor, c_a. We initially set $\alpha = 1$ and $\mathsf{c}_a = 1/\phi$ (Sec. 3.2.3). The importance of these parameters is investigated (Sec. 6.3).

Parameter values used in the model equations are collected in table 3.1.

3.4.3 Volume Forces

Volume forces include gravity and inertial forces caused by body movements. Assuming these to be balanced by the hydrostatic pressure, they can be eliminated by considering only the dynamic pressure. This assumption is not valid during sudden body movements.

3.4.4 Boundary Conditions

Spinal Canal Walls

We assume rigid, impermeable channel walls, applying the no-penetration and no-slip conditions:

$$\boldsymbol{u} = 0. \tag{3.28}$$

Pressure-Driven Flow

Channel inlets consist of both viscous and porous parts. To simulate pressure-driven flow, we apply a pseudo-traction condition on viscous parts and Dirichlet pressure conditions on porous parts.

Different forms of the Navier-Stokes equations, although equivalent in the continuum, are associated with different natural boundary conditions in the variational formulation (see e.g. Gresho and Sani, 1998). The stress-divergence form of the viscous term, used in Eq. 3.1, is associated with stress Neumann boundary conditions:

$$\hat{\boldsymbol{n}} \cdot \sigma = \mu \left(\frac{\partial \boldsymbol{u}}{\partial n} + \hat{\boldsymbol{n}} \cdot (\boldsymbol{\nabla u})^T \right) - p\hat{\boldsymbol{n}} = \bar{\boldsymbol{F}}, \tag{3.29}$$

where σ is the Cauchy stress tensor, $\hat{\boldsymbol{n}}$ is the boundary unit normal, and $\bar{\boldsymbol{F}}$ is an applied stress. This condition often leads to unwanted creeping around inlet corners. To avoid this we instead apply pseudo-traction conditions (Gresho and Sani, 1998, Sec. 3.8)[1]:

$$\mu \frac{\partial \boldsymbol{u}}{\partial n} - p\hat{\boldsymbol{n}} = -\bar{p}\hat{\boldsymbol{n}}, \tag{3.30}$$

where, $\bar{p}$ is a prescribed 'pressure'. To simulate flow in a channel that continues outside the computational domain, the solution should fulfill

$$\frac{\partial \boldsymbol{u}}{\partial n} = 0 \tag{3.31}$$

at inlet boundaries. Using the pseudo-traction condition, tangential components of Eq. 3.31 are fulfilled.

On porous inlets, we impose Dirichlet pressure boundary conditions, i.e.

$$p = p_0, \tag{3.32}$$

where p_0 is a prescribed pressure.

Temporal Variation

CSF flow in the spinal canal is dominated by the oscillating component coupled to the cardiac cycles (Loth et al., 2001; Gupta et al., 2009). The

[1] The pseudo-traction condition is actually the natural boundary condition associated with the Laplace form of the viscous term ($\mu \nabla^2 \boldsymbol{u}$). However, we keep the stress-divergence form in order to use stress interface conditions between viscous and porous domains (Eqs. 3.26 and 3.27).

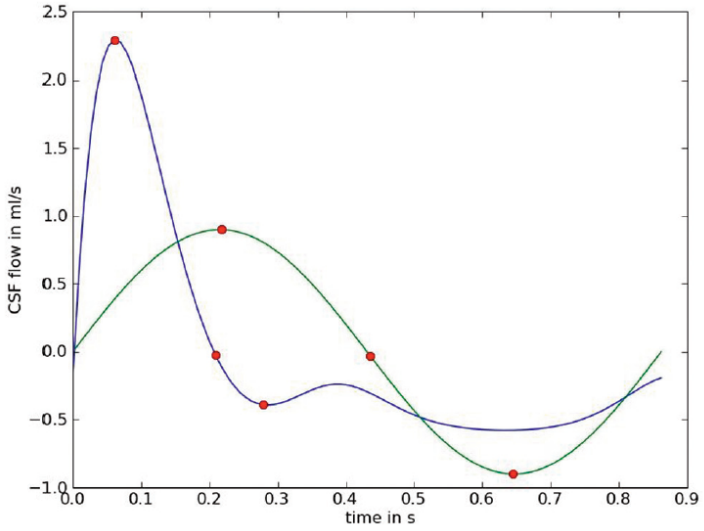

Figure 3.4: Examples of symmetric (green) and asymmetric (blue) temporal flow patterns (Hentschel et al., 2010). A symmetric sine function is used in the present study.

temporal flow pattern may be symmetric, varying approximately like a sine, or it could have a more irregular form (Fig. 3.4). In this study we apply a simple sinusoidal variation with period 1 s, approximately the timespan of one heartbeat.

3.4.5 Initial Conditions

Flow simulations are started from rest. This creates a transient phase before a cyclic solution is obtained. The applied pressure difference over the channel inlets is chosen to be maximal at $t = 0$. From experience we know that, for this type of problem, pressure peaks when velocities change direction. It is thus expected that this choice of initial boundary conditions causes a more rapid relaxation.

3.4.6 Two-Dimensional Model

Geometry

For initial investigations we use a simplified two-dimensional geometry. The spinal canal is represented as a rectangular channel with a porous medium cord in the center (Fig. 3.5). Simulations are performed both with and without a rectangular cavity located in the center of the cord.

Model dimensions are collected in table 3.2. Channel and cord diameters are taken from the idealized model of Linge et al. (2010).

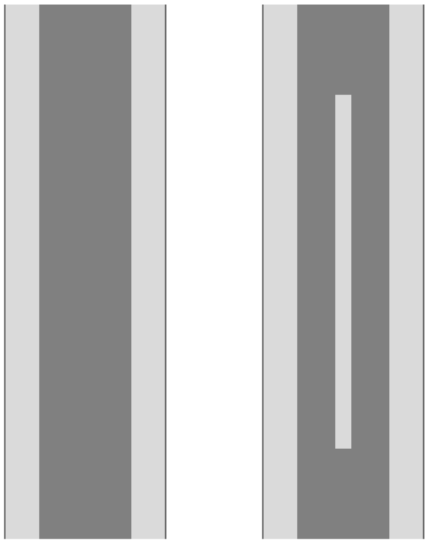

(a) Plain flow domain (b) Cavity flow domain

Figure 3.5: Computational domains used in 2D flow simulations. Darker gray depicts the porous media cord tissue. Lighter gray depicts the SAS and spinal cord cavity, governed by the viscous equations.

Model dimensions [cm]	
Spinal canal radius	0.90
Spinal cord radius	0.50
Length of channel segment	6.00
Cavity radius	0.10
Cavity length	4.00

Table 3.2: Dimensions of 2D rectangular flow domain.

Flow Conditions

A sinusoidal pressure difference with amplitude 20 Pa and period 1 s is applied, resulting in maximal SAS velocities of about 5–6 cm/s. For symmetry, the applied pressure on each inlet is equal in magnitude and of opposite sign.

Chapter 4

Numerical Methods

The model equations are solved by the finite element method (FEM). Implementation is done in FEniCS, a software package designed for automated solution of partial differential equations. Introductions to FEM and FEniCS are given in sections 4.1–4.2.

We investigate three different numerical schemes. These are presented in section 4.3. Applied finite elements and linear solvers are presented in sections 4.4 and 4.5, respectively.

4.1 The Finite Element Method

The finite element method (FEM) is a numerical approach for finding approximate solutions to partial differential equations (PDEs). FEM straightforwardly handles geometrically complex domains, and is thus appropriate for flow simulations in realistic models of the human spinal canal. The theoretical field of finite element methods is vast, and a full treatment is not possible within the scope of this thesis. Instead, we settle with a short introduction, giving an overview of basic principles.

The first step in FEM is to rewrite the PDE as a *variational problem*. Then, by restricting solutions to finite dimensional function spaces, an approximate solution is found by the solution of an algebraic system of equations. FEM is characterized by the choice of piecewise polynomial approximation spaces, defined through a set of *finite elements*. In this introduction, special emphasis will be on the concept of variational problems, as this is central in problem definition in FEniCS.

4.1.1 Variational Formulation

Rewriting a PDE as a *variational problem* is central in FEM and many other related methods. Variational formulations are alternative, weaker statements

of the original problem. Consider a general PDE, written as

$$\mathcal{L}(u(\boldsymbol{x})) = 0, \quad \boldsymbol{x} \in \Omega, \tag{4.1}$$

where $\mathcal{L}$ is some differential operator and $u(\boldsymbol{x})$ is the unknown function on a spatial domain, Ω. Conversion to variational form consists of multiplying by a *test function*, v, and integrating over the domain,

$$\int_\Omega \mathcal{L}(u(\boldsymbol{x}))v \,\mathrm{d}\Omega = 0. \tag{4.2}$$

Terms involving higher-order derivatives are integrated by parts. The resulting boundary terms are used to impose Neumann boundary conditions. Dirichlet boundary conditions are handled as additional restrictions on the solution, u. Usually, v is demanded to be zero at Dirichlet boundaries, and the corresponding boundary integrals vanish. The final integral statement can be written as

$$a(u, v) = L(v), \tag{4.3}$$

where terms dependent on the unknown, u, are collected in $a(u, v)$, and the remaining terms in $L(v)$.

A variational problem is formulated by demanding Eq. 4.3 to be fulfilled for *any* test function, v. Restrictions confine u and v to function spaces V and $\hat{V}$, respectively. In addition to the constraints on Dirichlet boundaries, u and v must be sufficiently differentiable for the integrals in Eq. 4.3 to exist. The complete variational problem is stated as:

Variational Form 4.1.1. *Find $u \in V$ such that*

$$a(u, v) = L(v) \qquad \forall v \in \hat{V}. \tag{4.4}$$

The variational problem is, in a sense, a weaker statement compared to the original PDE. Firstly, it is formulated through averages over the domain, as opposed to an equation to be fulfilled at each spatial point. Secondly, the solution space is enlarged. Solutions of the original PDE need to be sufficiently smooth such that all derivatives appearing in the equation exist. In the variational formation it suffices that the corresponding integrals exist. Furthermore, integrating by parts lowers the order of derivatives.

4.1.2 Discretization

The variational problem is discretized by seeking an approximation, $u_h \simeq u$, confined to a finite-dimensional subspace, $V_h \subset V$. This approximation has $N = \dim(V_h)$ degrees of freedom. For a unique representation, the test function, v, must be restricted to a subspace, $\hat{V}_h \subset \hat{V}$, of the same dimension as V_h. The resulting *discrete variational problem* is stated as:

Discrete Variational Form 4.1.1. *Find $u_h \in V_h$ such that*

$$a(u_h, v) = L(v) \qquad \forall v \in \hat{V}_h. \tag{4.5}$$

This is written on the form of an algebraic system of equations by introducing basis functions, $\{\phi_i\}_{i=1}^N$ and $\{\hat{\phi}_i\}_{i=1}^N$, such that

$$V_h = \text{span}\{\phi_1(\boldsymbol{x}), \phi_2(\boldsymbol{x}), \ldots, \phi_N(\boldsymbol{x})\},$$
$$\hat{V}_h = \text{span}\{\hat{\phi}_1(\boldsymbol{x}), \hat{\phi}_2(\boldsymbol{x}), \ldots, \hat{\phi}_N(\boldsymbol{x})\}.$$

Given a basis, the approximation, u_h, can be written as

$$u_h = \sum_{j=1}^{N} u_j \phi_j(\boldsymbol{x}), \tag{4.6}$$

where u_j are coefficients, defining the degrees of freedom. Furthermore, demanding Eq. 4.5 to apply for all $v \in \hat{V}_h$, is equivalent to demanding it to apply for all basis functions, $\hat{\phi}_i$, that is,

$$a(\sum_{j=1}^{N} u_j \phi_j, \hat{\phi}_i) = L(\hat{\phi}_i), \qquad i = 1, 2, \ldots, N, \tag{4.7}$$

where we have replaced u_h by the sum in Eq. 4.6. For simplicity, we assume a linear PDE such that $a(u, v)$ is linear in u. In this case, Eq. 4.7 can be written as

$$\sum_{j=1}^{N} a(\phi_j, \hat{\phi}_i) u_j = L(\hat{\phi}_i), \qquad i = 1, 2, \ldots, N, \tag{4.8}$$

which is recognized as a linear algebraic system of equations. These are solved efficiently by a large selection of numerical methods. In the case of non-linear PDEs, non-linear systems of algebraic equations appear. In the present work, we apply a linearizing strategy to avoid dealing with non-linear systems of equations. We note, however, that these are solved effectively by iterative methods.

Because of the restrictions on V_h and $\hat{V}_h$, constructing basis functions is nontrivial in the general case. In particular, this applies when imposing Dirichlet boundary conditions on geometrically complicated domains. In FEM, however, this is straightforward because of a separation of boundary degrees of freedom. Imposing Dirichlet boundary conditions reduces to a simple modification of the final algebraic system of equations.

4.1.3 Finite Elements

FEM approximates solutions by piecewise polynomials. Approximation spaces and their basis functions are defined through a set of *finite elements*. A general finite element is given by the following triplet (Larson and Bengzon, 2010):

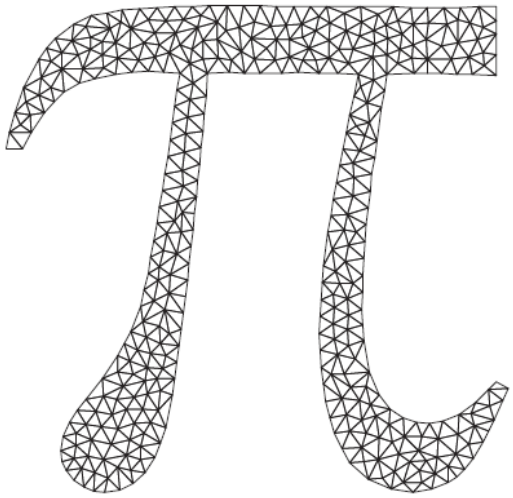

Figure 4.1: Example of a finite element mesh in 2D (Larson and Bengzon, 2010). The domain, in this case the Greek letter π, is divided into non-overlapping triangles.

1. A cell, $K \subseteq \Omega$
2. A polynomial function space, P on K
3. A set of functionals, L_i, $i = 1, 2, \ldots, n = \dim(P)$, defining the degrees of freedom.

The function space, P, is equipped with a basis, $\{\phi_i\}_{i=1}^n$, determined uniquely by the functionals, $\{L_i\}_{i=1}^n$, such that

$$L_i(\phi_j) = \delta_{ij}, \quad i, j = 1, 2, \ldots, n, \tag{4.9}$$

where δ_{ij} is the Kronecker delta. Finite elements determine the shape of polynomial approximations over each cell, and how these are connected at cell boundaries. In the following, we consider the example of a common family of elements, the *Lagrange elements*, yielding *continuous*, piecewise polynomial approximations.

The solution domain is divided into a mesh of non-overlapping cells (Fig. 4.1). In the case of Lagrange elements, these are simplexes, i.e. triangles in 2D, tetrahedrons in 3D and so on. The degrees of freedom are defined through a set of spatial points, called *nodes*. Each cell is associated with n nodes—n being the degree of the piecewise polynomial approximation space (Fig. 4.2). Basis functions are given by

$$\phi_i(x_j) = \delta_{ij}, \quad i, j = 1, 2, \ldots, N, \tag{4.10}$$

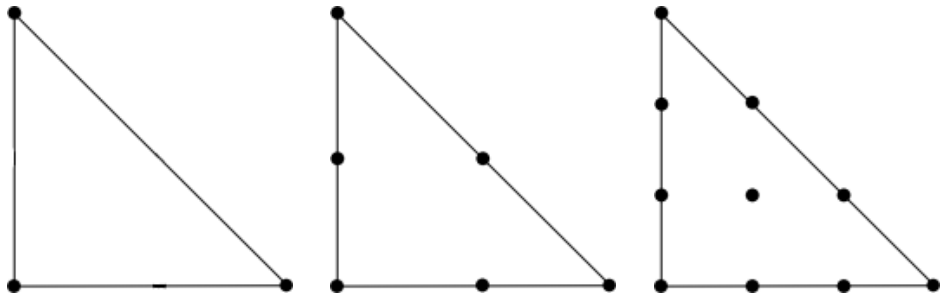

(a) Linear (b) Quadratic (c) Cubic

Figure 4.2: Illustration of nodes of the 2D Lagrange reference elements for linear (a), quadratic (b) and cubic (c) piecewise polynomial approximations (http://www.femwiki.org/).

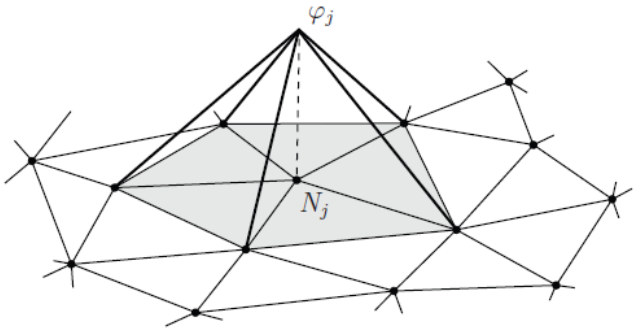

Figure 4.3: Example of a linear Lagrange basis function in 2D (Larson and Bengzon, 2010). Basis functions are non-zero only over cells associated with the corresponding node.

where x_j is node number j, and N is the total number of degrees of freedom. That is, there is one basis function associated with each node, its value being one in this node and zero in all other nodes. Each basis function is non-zero only over cells associated with the corresponding node (Fig. 4.3).

4.2 FEniCS: Automated Solution of Partial Differential Equations

The FEniCS project (http://fenicsproject.org) is a collection of free software aimed at automated solution of partial differential equations by the finite element method. This section provides an overview of basic FEniCS usage, as well as important functionality needed in the present work.

We use a development version following FEniCS 1.0.0. Source code may

need to be modified in order to work with other versions.

4.2.1 Basic Usage: Solving a Poisson Problem

A good introduction to FEniCS is given in the tutorial available on the project web page. In the following, we illustrate basic FEniCS usage through an example on a simple Poisson problem.

Problem Definition

Consider the Poisson problem in two dimensions,

$$-\nabla^2 u(x,y) = f(x,y) \qquad x,y \in \Omega, \tag{4.11}$$

with boundary conditions

$$u = u_0(x,y) \quad \text{on} \quad \partial\Omega_D, \qquad \frac{\partial u}{\partial n} = g(x,y) \quad \text{on} \quad \partial\Omega_N, \tag{4.12}$$

where $\partial\Omega_D$ and $\partial\Omega_N$ denote boundaries where Dirichlet and Neumann conditions apply, respectively. We use a simple unit square on $[0,1] \times [0,1]$ as problem domain, Ω, and define $\partial\Omega_N$ to be the boundary at $x = 1$. To reproduce the analytical solution, $u = 1 + x^2 + y^2$, we choose

$$f(x,y) = -4, \quad u_0(x,y) = 1 + x^2 + y^2, \quad g(x,y) = 2.$$

Variational Form

Multiplying the PDE by a test function, v, and integrating over the domain, we get

$$-\int_\Omega (\nabla^2 u) v \,\mathrm{d}x = \int_\Omega f v \,\mathrm{d}x. \tag{4.13}$$

The Laplace term is integrated by parts, and Neumann boundary conditions are imposed,

$$\begin{aligned} -\int_\Omega (\nabla^2 u) v \,\mathrm{d}x &= \int_\Omega \boldsymbol{\nabla} u \cdot \boldsymbol{\nabla} v \,\mathrm{d}x - \int_{\partial\Omega} \frac{\partial u}{\partial n} v \,\mathrm{d}s \\ &= \int_\Omega \boldsymbol{\nabla} u \cdot \boldsymbol{\nabla} v \,\mathrm{d}x - \int_{\partial\Omega_N} g v \,\mathrm{d}s. \end{aligned} \tag{4.14}$$

The resulting variational form is written as

$$a(u,v) = L(v), \tag{4.15}$$

where

$$a(u,v) = \int_\Omega \boldsymbol{\nabla} u \cdot \boldsymbol{\nabla} v \,\mathrm{d}x, \tag{4.16}$$

$$L(v) = \int_\Omega f v \,\mathrm{d}x + \int_{\partial\Omega_N} g v \,\mathrm{d}s. \tag{4.17}$$

The function, u, is commonly referred to as the *trial function*.

Implementation

FEniCS provides problem-solving environments in C++ and Python. The latter is used in this thesis. A FEniCS solver for the Poisson problem is included in listing 4.1. In the following, we go through this example line by line.

Listing 4.1: Implementation of the Poisson problem solver in FEniCS

```
# Import from dolfin library
from dolfin import *

# Define mesh and function space
mesh = UnitSquare(6, 4)
V = FunctionSpace(mesh, 'CG', 1)

# Define Dirichlet boundary conditions
u0 = Expression('1 + x[0]*x[0] + x[1]*x[1]')
class DirichletBoundary(SubDomain):
    def inside(self, x, on_boundary):
        return x[0] < DOLFIN_EPS or \
            x[1] < DOLFIN_EPS or \
            abs(x[1]-1.0) < DOLFIN_EPS

bc = DirichletBC(V, u0, DirichletBoundary())

# Define variational problem
u = TrialFunction(V)
v = TestFunction(V)
f = Constant(-4)
g = Constant(2)

a = inner(grad(u), grad(v))*dx
L = f*v*dx + g*v*ds

# Assemble matrices
A = assemble(a)
b = assemble(L)
bc.apply(A,b)

# Solve
u = Function(V)
solve(A, u.vector(), b)

# Plot
plot(u)
interactive()
```

First, the necessary tools are imported from the DOLFIN library, providing the FEniCS problem-solving environment:

```
from dolfin import *
```

A unit square mesh is defined through:

```
mesh = UnitSquare(6, 4)
```

FEniCS has built-in classes defining meshes over simple geometries. For this problem we use the 'UnitSquare' class, defining a uniform, unit square mesh on $[0,1] \times [0,1]$. Its arguments determine the coarseness of the mesh. In this case, the domain is divided into 6×4 rectangles which in turn are divided along the diagonal into triangles. More complex geometries are handled by separate preprocessor programs.

A function space, in this case given by linear Lagrange elements, is defined through:

```
V = FunctionSpace(mesh, 'CG', 1)
```

The arguments are the mesh, element type and polynomial degree. The element type specification, 'CG', is short for 'Continuous Galerkin', meaning Lagrange elements. The FEniCS book provides a list of available elements.

The variational problem is defined using FEniCS' unified form language (UFL):

```
u = TrialFunction(V)
v = TestFunction(V)
f = Constant(-4)
g = Constant(2)

a = inner(grad(u), grad(v))*dx
L = f*v*dx + g*v*ds
```

The UFL syntax should be evident, comparing with Eqs. 4.15–4.17. Note that the boundary integral is defined over the entire boundary, not just the Neumann part. This is done for simplicity. The test function, v, is zero on Dirichlet boundaries.

Next, we define Dirichlet boundary conditions:

```
u0 = Expression('1 + x[0]*x[0] + x[1]*x[1]')
class DirichletBoundary(SubDomain):
    def inside(self, x, on_boundary):
        return x[0] < DOLFIN_EPS or \
               x[1] < DOLFIN_EPS or \
               abs(x[1]-1.0) < DOLFIN_EPS

bc = DirichletBC(V, u0, DirichletBoundary())
```

Dirichlet boundary values are defined through an 'Expression' instance. Spatial coordinates are available through a vector x—x[0] and x[1] denoting x and y coordinates, respectively. There are various ways of defining Dirichlet boundaries in FEniCS. In this example, we create a subclass of 'SubDomain', and define the boundary by overriding its 'inside' method. The boundary expression and the Dirichlet boundary definition, are collected in a 'DirichletBC' instance.

Matrices of the algebraic system of equations are assembled by:

```
A = assemble(a)
b = assemble(L)
```

Dirichlet boundary conditions are imposed by:

```
bc.apply(A,b)
```

Finally, the algebraic system of equations is solved:

```
u = Function(V)
solve(A, u.vector(), b)
```

Optional arguments may be given to specify the type of linear solver, and a preconditioner. Given no arguments, the default solver is a direct LU decomposition method.

The solution is visualized through the commands:

```
plot(u)
interactive()
```

4.2.2 Advanced Usage

We introduce more advanced FEniCS functionality needed in the present work. This includes solving coupled PDEs, defining mixed finite elements and time dependent expressions.

Splitting the Domain

Solving coupled PDEs requires a means of splitting the domain—defining sub domains, boundary parts, interfaces and interface orientation. In FEniCS this is done through *mesh functions*. Mesh functions are discrete functions that can be evaluated at a set of mesh entities, used to mark cells and facets. In the following, we go through the implemented splitting into porous and viscous parts.

First, mesh functions for cell domains, interior and exterior facet domains and facet orientation are created:

```
# Initialize
D = mesh.topology().dim()
mesh.init(D-1, D)

# Create mesh functions
cell_domains = MeshFunction('uint', mesh, D)
interior_facet_domains = MeshFunction('uint', mesh, D - 1)
exterior_facet_domains = MeshFunction('uint', mesh, D - 1)
orientation = mesh.data().create_mesh_function(\
    'facet_orientation', D - 1)

# Set default values
cell_domains.set_all(default)
```

```
interior_facet_domains.set_all(default)
exterior_facet_domains.set_all(default)
orientation.set_all(default)
```

The last argument of 'MeshFunction' specifies the entity topological dimension, that is if the mesh function applies to cells, facets or vertices. Each sub domain or boundary part is given a marker. In the present case, these are unsigned integers, as specified by the 'uint' argument. The orientation mesh function is marked by cells, and is an attribute of the mesh. This requires mesh cells and facets to be initialized through 'mesh.init'. All mesh functions are given default values to check for errors when marked.

Given a function that defines the porous domain, cells are marked by the following statements:

```
cell_domains.set_all(fluid_domain)
for cell in cells(mesh):
    index = cell.index()
    midpoint = cell.midpoint()
    if self.inside_porous_domain(midpoint):
        cell_domains[index] = porous_domain
```

Initially, all cells are marked as belonging to the viscous domain. Then, the cells are traversed and re-marked if the midpoint is evaluated to be inside the porous domain.

Boundaries are initially marked as either inlets or walls:

```
Boundary(index=1, radius=0.5*self.length).mark(\
    exterior_facet_domains, inlet)
Boundary(index=0, radius=self.radius).mark(\
    exterior_facet_domains, wall)
```

This is done through a 'Boundary' sub-class of 'SubDomain':

```
class Boundary(SubDomain):
    def __init__(self, index, radius):
        self.index, self.radius = index, radius
        SubDomain.__init__(self)

    def inside(self, x, on_boundary):
        index, radius = self.index, self.radius
        return abs(abs(x[index]) - radius) < eps
```

Note that this function is only valid for rectangular domains with symmetry about the axes.

After walls and inlets are marked, all facets are traversed. Boundary facets are marked as either viscous walls, viscous inlets, porous walls or porous inlets. Interior facets are marked and given an orientation at interfaces between viscous and porous domains.

```
for facet in facets(mesh):
    # Get facet index and adjacent cells
```

```
    index = facet.index()
    adjacent_cells = facet.entities(D)

    # Exterior facets
    if len(adjacent_cells) == 1:
        cell = adjacent_cells[0]
        domain_type = cell_domains.array()[cell]
        boundary_type = exterior_facet_domains.array()[index]

        # Fluid boundaries
        if domain_type == fluid_domain:
            if boundary_type == inlet:
                exterior_facet_domains[index] = fluid_inlet
            elif boundary_type == wall:
                exterior_facet_domains[index] = fluid_wall
            else:
                print 'Error in marking boundaries.'
                exit(0)
        # Porous boundaries
        elif domain_type == porous_domain:
            if boundary_type == inlet:
                exterior_facet_domains[index] = porous_inlet
            elif boundary_type == wall:
                exterior_facet_domains[index] = porous_wall
            else:
                print 'Error in marking boundaries.'
                exit(0)
        else:
            print 'Error in marking boundaries.'
            exit(0)

    #Interior facets
    else:
        c0, c1 = adjacent_cells
        s0, s1 = cell_domains.array()[c0], \
            cell_domains.array()[c1]
        if s0 == fluid_domain and s1 == porous_domain:
            interior_facet_domains[index] = interface
            orientation[index] = c1  # ('+') denotes porous cell
        elif s0 == porous_domain and s1 == fluid_domain:
            interior_facet_domains[index] = interface
            orientation[index] = c0  # ('+') denotes porous cell
```

Facets are marked by evaluating adjacent cells; exterior and interior facets are handled separately. Walls and inlets are marked as either viscous or porous, depending on the marking of the adjacent cell. Interior facets are marked as interfaces if in between viscous and porous cells. The orientation mesh function is marked by the adjacent porous cell. When defining variational forms, this means that porous and viscous interface properties are denoted by '+' and '−', respectively.

Defining Variational Forms on a Split Domain

Isolated integrals over sub domains or boundary parts are done using mesh function markers. For instance,

```
dx(fluid_domain)
```

specifies integration over the viscous domain, and

```
ds(porous_inlet)
```

an integration over porous inlets. A typical integration over an interface is written as:

```
q('+')*inner(u('-'), n('+'))*dS(interface)
```

Integration over interior facets is specified by 'dS'. All interface quantities must be restricted to one of the adjacent domains. This is done through the '+' and '–' arguments, denoting porous and viscous quantities, respectively.

Cell and facet domain markers are just integers; they are of no use without the corresponding mesh functions. These are included in assembly:

```
A = assemble(a,
             cell_domains=cell_domains,
             exterior_facet_domains=exterior_facet_domains,
             interior_facet_domains=interior_facet_domains)
```

Mesh Function Specification of Dirichlet Boundaries

Mesh functions over exterior facets can be used in the specification of Dirichlet boundary conditions. For instance, in the fully coupled scheme, these are implemented as:

```
bcu = [DirichletBC(V, uwall, exterior_facet_domains, fluid_wall)]
bcp = [DirichletBC(Q, p0, exterior_facet_domains, porous_inlet)]
```

Like in the Poisson equation example, the first two arguments of 'DirichletBC' are a function space and the boundary expression. However, instead of using a function to specify the boundary, a mesh function and a marker are given as arguments.

Mixed Elements

In the fully coupled scheme for the Navier-Stokes/Darcy system, mixed finite elements are applied. That is, different function spaces are used for the different unknowns. A mixed function space for velocity and pressure is created by the following statements:

```
V = VectorFunctionSpace(mesh, 'CG', 2)
Q = FunctionSpace(mesh, 'CG', 1)
W = V*Q
```

The vector function space, 'V', applies to the velocity and the function space, 'Q', to the pressure. 'W' denotes the mixed space. Trial and test functions are defined by:

```
(u, p) = TrialFunctions(W)
(v, q) = TestFunctions(W)
```

Solutions are stored in a function instance, defined on the mixed space:

```
w = Function(V)
solve(A, w.vector(), b)
```

This can be split in order to access velocity and pressure separately:

```
(ufunc, pfunc) = w.split()
```

Time Dependent Expressions

FEniCS 'Expression' instances can hold time dependent expressions. Consider e.g.:

```
p0 = Expression('cos(2*pi*t)', t=0)
```

The keyword argument, 't', denotes time. This is stored in an attribute of 'p0', and can be changed at each time step:

```
p0.t = t
```

4.3 Numerical Schemes

We investigate three different numerical schemes. First, we develop a unified, mixed formulation, allowing for Taylor-Hood elements to be applied over the entire computational domain. Then we consider variants of incremental pressure correction schemes, decoupling the system of equations into separate equations for velocity and pressure. The first is developed based on the mixed formulation. The second is applied to a Brinkman model, allowing for the same system of equations to be solved over the entire computational domain by representing the porous parts by a discontinuous drag term.

4.3.1 Preliminaries

Generalized Navier-Stokes/Darcy System

We revisit the Navier-Stokes/Darcy system, and add generalizations used in numerical experiments. The flow domain, Ω, is divided into viscous and porous parts, Ω_v and Ω_p, respectively. Viscous flow in Ω_v is governed by the incompressible Navier-Stokes equations,

$$\rho\left(\frac{\partial \boldsymbol{u}}{\partial t} + \boldsymbol{u}\cdot\boldsymbol{\nabla}\boldsymbol{u}\right) = \boldsymbol{\nabla}\cdot\sigma(\boldsymbol{u},p) + \boldsymbol{f} \tag{4.18}$$

$$\boldsymbol{\nabla} \cdot \boldsymbol{u} = g, \tag{4.19}$$

where $\sigma(\boldsymbol{u}) = 2\mu\epsilon(\boldsymbol{u}) - p\mathbb{I}$ and $\epsilon(\boldsymbol{u}) = \frac{1}{2}\left(\boldsymbol{\nabla}\boldsymbol{u} + (\boldsymbol{\nabla}\boldsymbol{u})^T\right)$. Porous flow in Ω_p is governed by a non-stationary Darcy's law,

$$\frac{\rho}{\phi}\frac{\partial \boldsymbol{u}}{\partial t} = -\boldsymbol{\nabla} p - \frac{\mu}{K}\boldsymbol{u} + \boldsymbol{f}, \tag{4.20}$$

$$\boldsymbol{\nabla} \cdot \boldsymbol{u} = g. \tag{4.21}$$

Similarly, the boundary, $\partial\Omega$, is divided into viscous and porous parts, $\partial\Omega_\mathrm{v}$ and $\partial\Omega_\mathrm{p}$, respectively. The boundary conditions are

$$\boldsymbol{u} = \boldsymbol{u}_0 \qquad \text{or} \qquad \mu\frac{\partial \boldsymbol{u}}{\partial n} - p\hat{\boldsymbol{n}} = -\bar{p}\hat{\boldsymbol{n}}, \tag{4.22}$$

on the viscous boundary and

$$p = p_0 \qquad \text{or} \qquad \boldsymbol{u} \cdot \hat{\boldsymbol{n}} = \bar{\boldsymbol{u}} \cdot \hat{\boldsymbol{n}}, \tag{4.23}$$

on the porous boundary. The coupling conditions at interfaces, $\Gamma = \Omega_\mathrm{v} \cap \Omega_\mathrm{d}$, are

$$\boldsymbol{u}_\mathrm{v} \cdot \hat{\boldsymbol{n}} = \boldsymbol{u}_\mathrm{p} \cdot \hat{\boldsymbol{n}}, \tag{4.24}$$

$$2\mu\hat{\boldsymbol{n}} \cdot \epsilon(\boldsymbol{u}_\mathrm{v}) \cdot \hat{\boldsymbol{n}} - p_\mathrm{v} = -p_\mathrm{p} + h_1, \tag{4.25}$$

$$2\hat{\boldsymbol{n}} \cdot \varepsilon(\boldsymbol{u}_\mathrm{v}) \cdot \hat{\boldsymbol{\tau}} = \alpha K^{-1/2}\boldsymbol{u}_\mathrm{v} \cdot \hat{\boldsymbol{\tau}} + h_2, \tag{4.26}$$

where $\hat{\boldsymbol{n}}$ is the unit normal vector pointing out of the porous domain and $\hat{\boldsymbol{\tau}}$ is the tangent vector. Viscous interface quantities are denoted with a subscript 'v', porous interface quantities with a subscript 'p'.

This form of the Navier-Stokes/Darcy system is a slight modification of the original problem presented in chapter 3. Additional boundary conditions are applied, and generalizations, g, h_1 and h_2, have been added. This is done in order to simplify verification through the method of manufactured solutions (see chapter 5).

Inner Product Notation

We use $\langle \cdot, \cdot \rangle$ to denote inner products. Let $\boldsymbol{u}$ and $\boldsymbol{v}$ be either vector-valued or scalar functions. The L^2 inner product of $\boldsymbol{u}$ and $\boldsymbol{v}$ is defined as

$$\langle \boldsymbol{u}, \boldsymbol{v} \rangle_\Omega = \int_\Omega \boldsymbol{u} \cdot \boldsymbol{v} \, \mathrm{d}\Omega. \tag{4.27}$$

A subscript denotes the integration domain.

4.3.2 Coupled Scheme

In the coupled scheme velocity and pressure is solved for simultaneously. A semi-implicit discretization in time is combined with a unified, mixed finite element discretization in space.

Temporal Discretization

An implicit discretization in time is achieved with the finite difference method and the Backward Euler scheme:

1. Solutions are sought at discrete points in time, $t_0, t_1, \ldots, t_N$. For simplicity, we assume equal steps, Δt, such that $t_n = n\Delta t$. The solution at time step t_n is denoted with superscript n:

$$\boldsymbol{u}(t_n) = \boldsymbol{u}^n, \qquad p(t_n) = p^n. \tag{4.28}$$

2. Time derivatives are approximated by finite differences. In this case, these are given by the Backward Euler method:

$$\frac{\partial \boldsymbol{u}^n}{\partial t} \simeq \frac{\boldsymbol{u}^n - \boldsymbol{u}^{n-1}}{\Delta t}. \tag{4.29}$$

The convection term in Eq. 4.18 is non-linear. This term is linearized by using the velocity from the previous step as convective velocity,

$$\boldsymbol{u}^n \cdot \boldsymbol{\nabla} \boldsymbol{u}^n \simeq \boldsymbol{u}^{n-1} \cdot \boldsymbol{\nabla} \boldsymbol{u}^n. \tag{4.30}$$

The resulting semi-implicit temporal scheme is

$$\frac{\rho}{\Delta t}\boldsymbol{u}^n + \rho \boldsymbol{u}^{n-1} \cdot \boldsymbol{\nabla} \boldsymbol{u}^n - \boldsymbol{\nabla} \cdot \sigma(\boldsymbol{u}^n, p^n) = \frac{\rho}{\Delta t}\boldsymbol{u}^{n-1} + \boldsymbol{f}^n \tag{4.31}$$

$$-\boldsymbol{\nabla} \cdot \boldsymbol{u}^n = -g^n, \tag{4.32}$$

in the viscous domain, and

$$\left(\frac{\rho}{\phi \Delta t} + \frac{\mu}{K}\right)\boldsymbol{u}^n + \boldsymbol{\nabla} p^n = \frac{\rho}{\phi \Delta t}\boldsymbol{u}^{n-1} + \boldsymbol{f}^n \tag{4.33}$$

$$-\boldsymbol{\nabla} \cdot \boldsymbol{u}^n = -g^n, \tag{4.34}$$

in the porous domain. The equations of continuity have been multiplied by -1 for symmetry in the final scheme.

Discrete Variational Form

Due to the fact that most Stokes elements are unstable for Darcy flow and vice versa, numerical methods for Darcy-Stokes type equations have been studied to a large extent in recent years (cf. e.g. Karper et al. (2008); Xie et al. (2008); Juntunen and Stenberg (2009)). The common approach is to apply different finite element spaces for the viscous and porous regions. However, most available software packages, including FEniCS, do not support this feature. This motivates for the development of *unified* discretizations, that

is discretizations that apply the same finite element spaces over the entire computational domain.

In this work, we apply a unified, mixed finite element discretization based on the L^2 formulation proposed by Karper et al. (2008) for the stationary Darcy-Stokes system. Karper et al. show that, for the stationary problem, this discretization is stable combined with Taylor-Hood elements over the entire domain. We apply a similar discretization strategy on the Navier-Stokes/Darcy system.

Inner products of the equations of motion and the equations of continuity are taken with test functions $\boldsymbol{v}$ and q, respectively.

$$\begin{aligned}\frac{\rho}{\Delta t}\langle \boldsymbol{u}^n,\, \boldsymbol{v}\rangle_{\Omega_\mathrm{v}} + \rho\langle \boldsymbol{u}^{n-1}\cdot\boldsymbol{\nabla}\boldsymbol{u}^n,\, \boldsymbol{v}\rangle_{\Omega_\mathrm{v}} - \langle \boldsymbol{\nabla}\cdot\sigma(\boldsymbol{u}^n, p^n),\, \boldsymbol{v}\rangle_{\Omega_\mathrm{v}} \\ + \left(\frac{\rho}{\phi\Delta t} + \frac{\mu}{K}\right)\langle \boldsymbol{u}^n,\, \boldsymbol{v}\rangle_{\Omega_\mathrm{p}} + \langle \boldsymbol{\nabla} p^n,\, \boldsymbol{v}\rangle_{\Omega_\mathrm{p}} \\ = \frac{\rho}{\Delta t}\langle \boldsymbol{u}^{n-1},\, \boldsymbol{v}\rangle_{\Omega_\mathrm{v}} + \langle \boldsymbol{f}^n,\, \boldsymbol{v}\rangle_{\Omega_\mathrm{v}} \\ + \frac{\rho}{\phi\Delta t}\langle \boldsymbol{u}^{n-1},\, \boldsymbol{v}\rangle_{\Omega_\mathrm{p}} + \langle \boldsymbol{f}^n,\, \boldsymbol{v}\rangle_{\Omega_\mathrm{p}},\end{aligned} \tag{4.35}$$

$$-\langle \boldsymbol{\nabla}\cdot\boldsymbol{u},\, q\rangle_\Omega = -\langle g^n,\, q\rangle_\Omega. \tag{4.36}$$

Integration by parts is performed on the viscous stress term and on the porous equation of continuity. First, integrating the stress term by parts, we get

$$\begin{aligned}\langle \boldsymbol{\nabla}\cdot\sigma(\boldsymbol{u},p),\, \boldsymbol{v}\rangle_{\Omega_\mathrm{v}} &= -\langle \sigma(\boldsymbol{u},p),\, \boldsymbol{\nabla}\boldsymbol{v}\rangle_{\Omega_\mathrm{v}} + \langle \hat{\boldsymbol{n}}\cdot\sigma(\boldsymbol{u},p),\, \boldsymbol{v}\rangle_{\partial\Omega_\mathrm{v}} \\ &\quad + \langle \hat{\boldsymbol{n}}_\mathrm{v}\cdot\sigma(\boldsymbol{u}_\mathrm{v},p_\mathrm{v}),\, \boldsymbol{v}_\mathrm{v}\rangle_\Gamma \\ &= -2\mu\langle \epsilon(\boldsymbol{u}),\, \epsilon(\boldsymbol{v})\rangle_{\Omega_\mathrm{v}} + \langle p,\, \boldsymbol{\nabla}\cdot\boldsymbol{v}\rangle_{\Omega_\mathrm{v}} \\ &\quad + \langle \mu\hat{\boldsymbol{n}}\cdot(\boldsymbol{\nabla}\boldsymbol{u})^T + \mu\frac{\partial\boldsymbol{u}}{\partial n} - p\hat{\boldsymbol{n}},\, \boldsymbol{v}\rangle_{\partial\Omega_\mathrm{v}} \\ &\quad + \langle -2\mu(\hat{\boldsymbol{n}}\cdot\epsilon(\boldsymbol{u}_\mathrm{v})\cdot\hat{\boldsymbol{n}})\hat{\boldsymbol{n}} - 2\mu(\hat{\boldsymbol{n}}\cdot\epsilon(\boldsymbol{u}_\mathrm{v})\cdot\hat{\boldsymbol{\tau}})\hat{\boldsymbol{\tau}} + p_\mathrm{v}\hat{\boldsymbol{n}},\, \boldsymbol{v}\rangle_\Gamma \\ &= -2\mu\langle \epsilon(\boldsymbol{u}),\, \epsilon(\boldsymbol{v})\rangle_{\Omega_\mathrm{v}} + \langle p,\, \boldsymbol{\nabla}\cdot\boldsymbol{v}\rangle_{\Omega_\mathrm{v}} \\ &\quad + \mu\langle \hat{\boldsymbol{n}}\cdot(\boldsymbol{\nabla}\boldsymbol{u})^T,\, \boldsymbol{v}\rangle_{\partial\Omega_\mathrm{v}} - \langle \bar{p}\hat{\boldsymbol{n}},\, \boldsymbol{v}\rangle_{\partial\Omega_\mathrm{v}} \\ &\quad - \langle (p_v - p_p + h_1)\hat{\boldsymbol{n}},\, \boldsymbol{v}_\mathrm{v}\rangle_\Gamma - \mu\langle (\alpha K^{-\frac{1}{2}}\boldsymbol{u}_\mathrm{v}\cdot\hat{\boldsymbol{\tau}} + h_2)\hat{\boldsymbol{\tau}},\, \boldsymbol{v}_\mathrm{v}\rangle_\Gamma \\ &\quad + \langle p_\mathrm{v}\hat{\boldsymbol{n}},\, \boldsymbol{v}_\mathrm{v}\rangle_\Gamma \\ &= -2\mu\langle \epsilon(\boldsymbol{u}),\, \epsilon(\boldsymbol{v})\rangle_{\Omega_\mathrm{v}} + \langle p,\, \boldsymbol{\nabla}\cdot\boldsymbol{v}\rangle_{\Omega_\mathrm{v}} \\ &\quad + \mu\langle \hat{\boldsymbol{n}}\cdot(\boldsymbol{\nabla}\boldsymbol{u})^T,\, \boldsymbol{v}\rangle_{\partial\Omega_\mathrm{v}} - \langle \bar{p}\hat{\boldsymbol{n}},\, \boldsymbol{v}\rangle_{\partial\Omega_\mathrm{v}} \\ &\quad + \langle p_\mathrm{p}\hat{\boldsymbol{n}},\, \boldsymbol{v}_\mathrm{v}\rangle_\Gamma - \mu\alpha K^{-\frac{1}{2}}\langle \boldsymbol{u}_\mathrm{v}\cdot\hat{\boldsymbol{\tau}},\, \boldsymbol{v}_\mathrm{v}\cdot\hat{\boldsymbol{\tau}}\rangle_\Gamma \\ &\quad - \langle h_1\hat{\boldsymbol{n}} + \mu h_2\hat{\boldsymbol{\tau}},\, \boldsymbol{v}_\mathrm{v}\rangle_\Gamma.\end{aligned} \tag{4.37}$$

The integration by parts is performed in the first step. In the third step, the Neumann boundary condition in Eq. 4.22 and the interface conditions in Eqs. 4.25 and 4.26 are applied. Step two and four are just rewriting and

rearranging of terms. Integrating the divergence term in the porous media equation of continuity by parts, we get

$$\begin{aligned}\langle \boldsymbol{\nabla}\cdot\boldsymbol{u},\, q\rangle_{\Omega_\mathrm{p}} &= -\langle \boldsymbol{u},\, \boldsymbol{\nabla} q\rangle_{\Omega_\mathrm{p}} + \langle \boldsymbol{u}\cdot\hat{\boldsymbol{n}},\, q\rangle_{\partial\Omega_\mathrm{p}} + \langle \boldsymbol{u}_\mathrm{p}\cdot\hat{\boldsymbol{n}},\, q_\mathrm{p}\rangle_\Gamma \\ &= -\langle \boldsymbol{u},\, \boldsymbol{\nabla} q\rangle_{\Omega_\mathrm{p}} + \langle \bar{\boldsymbol{u}}\cdot\hat{\boldsymbol{n}},\, q\rangle_{\partial\Omega_\mathrm{p}} + \langle \boldsymbol{u}_\mathrm{v}\cdot\hat{\boldsymbol{n}},\, q_\mathrm{p}\rangle_\Gamma. \quad (4.38)\end{aligned}$$

The first step is the integration by parts, and the second imposes the Neumann boundary condition in Eq. 4.23 and the interface condition in Eq. 4.24.

The final variational problem results from inserting the terms integrated by parts in Eqs. 4.35 and 4.36. We include both the generalized form used in verification, and the simpler form used on flow problems.

Discrete Variational Form 4.3.1 (coupled scheme, generalized). *Find functions* $(\boldsymbol{u}^n, p^n) \in \boldsymbol{V}_h \times Q_h$ *such that for all* $(\boldsymbol{v}, q) \in \hat{\boldsymbol{V}}_h \times \hat{Q}_h$

$$a(\boldsymbol{u}^n, \boldsymbol{v}) + b(p^n, \boldsymbol{v}) = L_1(\boldsymbol{v}) \quad (4.39)$$

$$b(q, \boldsymbol{u}^n) = L_2(q), \quad (4.40)$$

where

$$\begin{aligned}a(\boldsymbol{u},\boldsymbol{v}) = {}& \frac{\rho}{\Delta t}\langle \boldsymbol{u},\, \boldsymbol{v}\rangle_{\Omega_v} + \rho\langle \boldsymbol{u}^{n-1}\cdot\boldsymbol{\nabla}\boldsymbol{u},\, \boldsymbol{v}\rangle_{\Omega_v} + 2\mu\langle \epsilon(\boldsymbol{u}),\, \epsilon(\boldsymbol{v})\rangle_{\Omega_v} \\ & - \mu\langle \hat{\boldsymbol{n}}\cdot(\boldsymbol{\nabla}\boldsymbol{u})^T,\, \boldsymbol{v}\rangle_{\partial\Omega_v} + \left(\frac{\rho}{\phi\Delta t} + \frac{\mu}{K}\right)\langle \boldsymbol{u},\, \boldsymbol{v}\rangle_{\Omega_p} \\ & + \mu\alpha K^{-\frac{1}{2}}\langle \boldsymbol{u}_v\cdot\hat{\boldsymbol{\tau}},\, \boldsymbol{v}_v\cdot\hat{\boldsymbol{\tau}}\rangle_\Gamma, \quad (4.41)\end{aligned}$$

$$b(q,\boldsymbol{v}) = -\langle q,\, \boldsymbol{\nabla}\cdot\boldsymbol{v}\rangle_{\Omega_v} + \langle \boldsymbol{\nabla} q,\, \boldsymbol{v}\rangle_{\Omega_p} - \langle q_p,\, \boldsymbol{v}_v\cdot\hat{\boldsymbol{n}}\rangle_\Gamma, \quad (4.42)$$

$$\begin{aligned}L_1(\boldsymbol{v}) = {}& \frac{\rho}{\Delta t}\langle \boldsymbol{u}^{n-1},\, \boldsymbol{v}\rangle_{\Omega_v} + \frac{\rho}{\phi\Delta t}\langle \boldsymbol{u}^{n-1},\, \boldsymbol{v}\rangle_{\Omega_p} + \langle \boldsymbol{f}^n,\, \boldsymbol{v}\rangle_\Omega \\ & - \langle \bar{p}\hat{\boldsymbol{n}},\, \boldsymbol{v}\rangle_{\partial\Omega_v} - \langle h_1\hat{\boldsymbol{n}} + \mu h_2\hat{\boldsymbol{\tau}},\, \boldsymbol{v}_v\rangle_\Gamma, \quad (4.43)\end{aligned}$$

$$L_2(q) = -\langle g^n,\, q\rangle_\Omega + \langle \bar{\boldsymbol{u}}\cdot\hat{\boldsymbol{n}},\, q\rangle_{\partial\Omega_p}. \quad (4.44)$$

Discrete Variational Form 4.3.2 (coupled scheme, flow problems). *Find functions* $(\boldsymbol{u}^n, p^n) \in \boldsymbol{V}_h \times Q_h$ *such that for all* $(\boldsymbol{v}, q) \in \hat{\boldsymbol{V}}_h \times \hat{Q}_h$

$$a(\boldsymbol{u}^n, \boldsymbol{v}) + b(p^n, \boldsymbol{v}) = L_1(\boldsymbol{v}) \quad (4.45)$$

$$b(q, \boldsymbol{u}^n) = L_2(q), \quad (4.46)$$

where

$$\begin{aligned}a(\boldsymbol{u},\boldsymbol{v}) = {}& \frac{\rho}{\Delta t}\langle \boldsymbol{u},\, \boldsymbol{v}\rangle_{\Omega_v} + \rho\langle \boldsymbol{u}^{n-1}\cdot\boldsymbol{\nabla}\boldsymbol{u},\, \boldsymbol{v}\rangle_{\Omega_v} + 2\mu\langle \epsilon(\boldsymbol{u}),\, \epsilon(\boldsymbol{v})\rangle_{\Omega_v} \\ & - \mu\langle \hat{\boldsymbol{n}}\cdot(\boldsymbol{\nabla}\boldsymbol{u})^T,\, \boldsymbol{v}\rangle_{\partial\Omega_v} + \left(\frac{\rho}{\phi\Delta t} + \frac{\mu}{K}\right)\langle \boldsymbol{u},\, \boldsymbol{v}\rangle_{\Omega_p} \\ & + \mu\alpha K^{-\frac{1}{2}}\langle \boldsymbol{u}_v\cdot\hat{\boldsymbol{\tau}},\, \boldsymbol{v}_v\cdot\hat{\boldsymbol{\tau}}\rangle_\Gamma, \quad (4.47)\end{aligned}$$

$$b(q,\boldsymbol{v}) = -\langle q,\, \boldsymbol{\nabla}\cdot\boldsymbol{v}\rangle_{\Omega_v} + \langle \boldsymbol{\nabla} q,\, \boldsymbol{v}\rangle_{\Omega_p} - \langle q_p,\, \boldsymbol{v}_v\cdot\hat{\boldsymbol{n}}\rangle_\Gamma, \quad (4.48)$$

$$L_1(\boldsymbol{v}) = \frac{\rho}{\Delta t}\langle \boldsymbol{u}^{n-1},\, \boldsymbol{v}\rangle_{\Omega_v} + \frac{\rho}{\phi\Delta t}\langle \boldsymbol{u}^{n-1},\, \boldsymbol{v}\rangle_{\Omega_p} - \langle \bar{p}\hat{\boldsymbol{n}},\, \boldsymbol{v}\rangle_{\partial\Omega_v}, \quad (4.49)$$

$$L_2(q) = \langle \bar{\boldsymbol{u}}\cdot\hat{\boldsymbol{n}},\, q\rangle_{\partial\Omega_p}. \quad (4.50)$$

Implementation in FEniCS

The FEniCS implementation of the coupled scheme variational form is included in listing 4.2. This is primarily written for flow problems. Additions needed in verification tests are added through an if-test. Note the following points:

- Interfaces are divided into parts parallel with the x-axis and parts parallel with the y-axis. This simplifies implementation of interface tangential components in the simple two-dimensional model. See the source code for implementation of the modified mesh function. Note that verification domains only have interfaces that are parallel with the y-axis.
- The discrete weak form for a is split into $a = c + d$, where c is constant and d depends on the velocity from the previous step. This is done in order to avoid reassembly of constant terms in every time step.
- In FEniCS, gradients of vectors are transposed compared to the notation used in this thesis, i.e.

$$\text{grad(u)} = (\boldsymbol{\nabla u})^T.$$

- On interfaces, porous domain quantities are marked with a '+'-sign and viscous domain quantities by '−'-signs.
- The generalizations 'ff' and 'gf' apply to the viscous (fluid) domain, while 'fp' and 'gp' apply to the porous domain.

Listing 4.2: Implementation of variational form in fully coupled solver.

```
# Define variational problem
(u, p) = TrialFunctions(W)
(v, q) = TestFunctions(W)
u1 = Function(V) # velocity from previous step
n = FacetNormal(mesh)

# momentum eq
c1 = rho/dt*inner(u, v)*dx(fluid_domain) \
    + 2*mu*inner(epsilon(u), epsilon(v))*dx(fluid_domain) \
    - mu*inner(grad(u).T*n, v)*ds(fluid_inlet) \
    + (rho/(dt*phi) + mu/K)*inner(u, v)*dx(porous_domain) \
    + mu*alpha/sqrt(K)*u('-')[0]*v('-')[0]*dS(interface_x) \
    + mu*alpha/sqrt(K)*u('-')[1]*v('-')[1]*dS(interface_y)

d1 = rho*inner(grad(u)*u1, v)*dx(fluid_domain) #not constant

b1 = -p*div(v)*dx(fluid_domain) \
    + inner(grad(p), v)*dx(porous_domain) \
    - p('+')*inner(v('-'), n('+'))*dS(interface_x) \
```

```
    - p('+')*inner(v('-'), n('+'))*dS(interface_y)

L1 = rho/dt*inner(u1, v)*dx(fluid_domain) \
    + rho/(dt*phi)*inner(u1, v)*dx(porous_domain) \
    - inner(v, pbar*n)*ds(fluid_inlet)

# continuity eq
b2 = -q*div(u)*dx(fluid_domain) \
    + inner(grad(q), u)*dx(porous_domain) \
    - q('+')*inner(u('-'), n('+'))*dS(interface_x) \
    - q('+')*inner(u('-'), n('+'))*dS(interface_y)

L2 = q*inner(ubar, n)*ds(porous_inlet)

# additions for test cases
if isinstance(problem, TestCase):
    L1 += inner(ff, v)*dx(fluid_domain) \
        + inner(fp, v)*dx(porous_domain) \
        - h1('-')*inner(v('-'), n('+'))*dS(interface_y) \
        - mu*h2('-')*v('-')[1]*dS(interface_y)

    L2 += -gf*q*dx(fluid_domain) \
        - gp*q*dx(porous_domain) \
        + q*inner(ubar, n)*ds(porous_wall)

# put together
c = c1 + b1 + b2
d = d1
L = L1 + L2
```

4.3.3 Incremental Pressure Correction Scheme

In the fully coupled scheme, both velocity and pressure degrees of freedom are solved for simultaneously. A simpler, more efficient method could be obtained by splitting the problem into separate equations for velocity and pressure. Such schemes are called *operator-splitting schemes*. In this work, we apply an operator-splitting scheme called the *incremental pressure correction scheme* (IPCS) to the coupled Navier-Stokes/Darcy system. The IPCS is a common scheme applied to the Navier-Stokes equations. On this simpler problem, it has been shown to be an overall accurate and efficient scheme (Valen-Senstad et al., 2011).

Temporal Discretization

The PDE is solved in a stepwise manner. A tentative velocity is computed from the equation of motion using the pressure field from the previous time step; this is then projected onto the space of divergence free vectors using

the equation of continuity. Consider the temporal scheme from Sec. 4.3.2:

$$\frac{\rho}{\Delta t}\boldsymbol{u}^n + \rho\boldsymbol{u}^{n-1}\cdot\boldsymbol{\nabla}\boldsymbol{u}^n - \boldsymbol{\nabla}\cdot\sigma(\boldsymbol{u}^n, p^n) = \frac{\rho}{\Delta t}\boldsymbol{u}^{n-1} + \boldsymbol{f}^n \quad \text{on} \quad \Omega_v, \tag{4.51}$$

$$\left(\frac{\rho}{\phi\Delta t} + \frac{\mu}{K}\right)\boldsymbol{u}^n + \boldsymbol{\nabla}p^n = \frac{\rho}{\phi\Delta t}\boldsymbol{u}^{n-1} + \boldsymbol{f}^n \quad \text{on} \quad \Omega_p, \tag{4.52}$$

$$-\boldsymbol{\nabla}\cdot\boldsymbol{u}^n = -g^n \quad \text{on} \quad \Omega. \tag{4.53}$$

Instead of solving this fully coupled scheme, the equations are split into separate equations for velocity and pressure. First, a tentative velocity, $\boldsymbol{u}^*$, is computed using the pressure field from the previous step:

$$\frac{\rho}{\Delta t}\boldsymbol{u}^* + \rho\boldsymbol{u}^{n-1}\cdot\boldsymbol{\nabla}\boldsymbol{u}^* - \boldsymbol{\nabla}\cdot\sigma(\boldsymbol{u}^*, p^{n-1}) = \frac{\rho}{\Delta t}\boldsymbol{u}^{n-1} + \boldsymbol{f}^n \quad \text{on} \quad \Omega_v, \tag{4.54}$$

$$\left(\frac{\rho}{\phi\Delta t} + \frac{\mu}{K}\right)\boldsymbol{u}^* + \boldsymbol{\nabla}p^{n-1} = \frac{\rho}{\phi\Delta t}\boldsymbol{u}^{n-1} + \boldsymbol{f}^n \quad \text{on} \quad \Omega_p. \tag{4.55}$$

This requires an initial pressure value, p_0, not needed in the original problem. It is common to either set $p_0 = 0$, or to make a 'guess' based on the nature of the problem. In flow simulations we choose p_0 to vary linearly along the length of the channel, such that it is equal to the initial pressure imposed at channel inlets. The velocity, $\boldsymbol{u}^n$, in Eqs. 4.51 and 4.52 can be expressed through the tentative velocity as

$$\boldsymbol{u}^n = \boldsymbol{u}^* - \frac{\Delta t}{\rho}\boldsymbol{\nabla}(p^n - p^{n-1}) + s_v(\boldsymbol{u}^c) \quad \text{on} \quad \Omega_v, \tag{4.56}$$

$$\boldsymbol{u}^n = \boldsymbol{u}^* - \frac{\phi\Delta t}{\rho}\boldsymbol{\nabla}(p^n - p^{n-1}) + s_p(\boldsymbol{u}^c) \quad \text{on} \quad \Omega_p, \tag{4.57}$$

where $\boldsymbol{u}^c = \boldsymbol{u}^n - \boldsymbol{u}^*$ and

$$s_v(\boldsymbol{u}^c) = \frac{\Delta t}{\rho}\left(-\rho\boldsymbol{u}^{n-1}\cdot\boldsymbol{\nabla}\boldsymbol{u}^c + 2\mu\epsilon(\boldsymbol{u}^c)\right), \tag{4.58}$$

$$s_p(\boldsymbol{u}^c) = -\frac{\phi\Delta t}{\rho}\frac{\mu}{K}\boldsymbol{u}^c. \tag{4.59}$$

The terms $s_v(\boldsymbol{u}^c)$ and $s_p(\boldsymbol{u}^c)$ originate from the implicit terms in Eqs. 4.51 and 4.52. It is common to discard these as this yields a simple Poisson problem for the corrected pressure. Since the error in the temporal discretization is already of order Δt, this should not affect the scheme accuracy. However, in our flow simulations K is small ($\sim 10^{-15}\,\mathrm{m}^2$), and discarding s_p could lead to large errors. Since this term is on the same form as the time derivative term, including it does not increase complexity of the pressure correction equation. However, initial tests show that this could lead to instabilities at interfaces between viscous and porous regions. We introduce a switch, β,

such that $\beta = 1$ includes s_p, and $\beta = 0$ does not. Eqs. 4.56 and 4.57 then read

$$\boldsymbol{u}^n = \boldsymbol{u}^* - \frac{\Delta t}{\rho}\boldsymbol{\nabla}(p^n - p^{n-1}) \quad \text{on} \quad \Omega_v, \tag{4.60}$$

$$\boldsymbol{u}^n = \boldsymbol{u}^* - \left(\frac{\rho}{\phi\Delta t} + \beta\frac{\mu}{K}\right)^{-1}\boldsymbol{\nabla}(p^n - p^{n-1}) \quad \text{on} \quad \Omega_p. \tag{4.61}$$

The next step is to use the equation of continuity (Eq. 4.53) to get an expression for the corrected pressure, p^n. Taking the divergence of Eqs. 4.60 and 4.61, and applying Eq. 4.53, we get

$$\boldsymbol{\nabla}^2 p^n = \boldsymbol{\nabla}^2 p^{n-1} + \frac{\rho}{\Delta t}(\boldsymbol{\nabla}\cdot\boldsymbol{u}^* - g) \quad \text{on} \quad \Omega_v, \tag{4.62}$$

$$\boldsymbol{\nabla}^2 p^n = \boldsymbol{\nabla}^2 p^{n-1} + \left(\frac{\rho}{\phi\Delta t} + \beta\frac{\mu}{K}\right)(\boldsymbol{\nabla}\cdot\boldsymbol{u}^* - g) \quad \text{on} \quad \Omega_p. \tag{4.63}$$

The corrected pressure is used in Eqs. 4.60 and 4.61 to compute the corrected velocity. The algorithm can be summarized in three steps. For each time step:

1. compute a tentative velocity, $\boldsymbol{u}^*$:

$$\frac{\rho}{\Delta t}\boldsymbol{u}^* + \rho\boldsymbol{u}^{n-1}\cdot\boldsymbol{\nabla}\boldsymbol{u}^* - \boldsymbol{\nabla}\cdot\sigma(\boldsymbol{u}^*, p^{n-1}) = \frac{\rho}{\Delta t}\boldsymbol{u}^{n-1} + \boldsymbol{f}^n \quad \text{on} \quad \Omega_\mathrm{v}, \tag{4.64}$$

$$\left(\frac{\rho}{\phi\Delta t} + \frac{\mu}{K}\right)\boldsymbol{u}^* + \boldsymbol{\nabla}p^{n-1} = \frac{\rho}{\phi\Delta t}\boldsymbol{u}^{n-1} + \boldsymbol{f}^n \quad \text{on} \quad \Omega_\mathrm{p}. \tag{4.65}$$

2. compute the corrected pressure, p^n:

$$\boldsymbol{\nabla}^2 p^n = \boldsymbol{\nabla}^2 p^{n-1} + \frac{\rho}{\Delta t}(\boldsymbol{\nabla}\cdot\boldsymbol{u}^* - g) \quad \text{on} \quad \Omega_\mathrm{v}, \tag{4.66}$$

$$\boldsymbol{\nabla}^2 p^n = \boldsymbol{\nabla}^2 p^{n-1} + \left(\frac{\rho}{\phi\Delta t} + \beta\frac{\mu}{K}\right)(\boldsymbol{\nabla}\cdot\boldsymbol{u}^* - g) \quad \text{on} \quad \Omega_\mathrm{p}. \tag{4.67}$$

3. compute the corrected velocity, $\boldsymbol{u}^n$:

$$\boldsymbol{u}^n = \boldsymbol{u}^* - \frac{\Delta t}{\rho}\boldsymbol{\nabla}(p^n - p^{n-1}) \quad \text{on} \quad \Omega_\mathrm{v}, \tag{4.68}$$

$$\boldsymbol{u}^n = \boldsymbol{u}^* - \left(\frac{\rho}{\phi\Delta t} + \beta\frac{\mu}{K}\right)^{-1}\boldsymbol{\nabla}(p^n - p^{n-1}) \quad \text{on} \quad \Omega_\mathrm{p}. \tag{4.69}$$

Modified Boundary Conditions

The decoupled equations require a new set of boundary conditions. On the porous boundary, these can be made equivalent to the original set. In the viscous case, however, tricks are done to imitate the actual conditions, leading to errors in thin layers near the boundary.

The original porous boundary conditions are of two kinds; either a pressure Dirichlet condition or a Neumann condition for the normal Darcy velocity are imposed, i.e.

$$p^n = p_0 \qquad \text{or} \qquad \boldsymbol{u}^n \cdot \hat{\boldsymbol{n}} = \bar{\boldsymbol{u}} \cdot \hat{\boldsymbol{n}} \qquad \text{on} \quad \partial\Omega_\text{p}. \tag{4.70}$$

In the IPCS, both the tentative velocity step and the velocity correction are pure projection steps over the porous domain. Thus, the only conditions imposed on the porous boundary are in the pressure correction. In this step, either p^n or $\frac{\partial p^n}{\partial n}$ needs to be prescribed. The first condition is identical to the Dirichlet condition in the original system. The latter can be expressed as a condition for $\boldsymbol{u}^n \cdot \hat{\boldsymbol{n}}$ by considering the normal component of Eq. 4.69,

$$\begin{aligned}\frac{\partial}{\partial n}(p^n - p^{n-1})|_{\partial\Omega_\text{p}} &= \left(\frac{\rho}{\phi\Delta t} + \beta\frac{\mu}{K}\right)(\boldsymbol{u}^* \cdot \hat{\boldsymbol{n}} - \boldsymbol{u}^n \cdot \hat{\boldsymbol{n}})|_{\partial\Omega_\text{p}} \\ &= \left(\frac{\rho}{\phi\Delta t} + \beta\frac{\mu}{K}\right)(\boldsymbol{u}^* \cdot \hat{\boldsymbol{n}} - \bar{\boldsymbol{u}} \cdot \hat{\boldsymbol{n}})|_{\partial\Omega_\text{p}},\end{aligned} \tag{4.71}$$

where $\boldsymbol{u}^n \cdot \hat{\boldsymbol{n}} = \bar{\boldsymbol{u}} \cdot \hat{\boldsymbol{n}}$ is inserted from the original Neumann condition.

On the viscous boundary, the original conditions are either of Dirichlet type for the velocity or what we referred to as the pseudo-traction condition,

$$\boldsymbol{u}^n = \boldsymbol{u}_0 \qquad \text{or} \qquad \mu\frac{\partial \boldsymbol{u}^n}{\partial n} - p^n\hat{\boldsymbol{n}} = -\bar{p}\hat{\boldsymbol{n}} \qquad \text{on} \quad \partial\Omega_\text{v}. \tag{4.72}$$

In the IPCS, viscous boundary conditions must be prescribed for $\boldsymbol{u}^*$ or $\frac{\partial \boldsymbol{u}^*}{\partial n}$ in the tentative velocity step and p^n or $\frac{\partial p^n}{\partial n}$ in the pressure correction step. The velocity correction is a pure projection step.

To imitate the Dirichlet condition, we set

$$\boldsymbol{u}^* = \boldsymbol{u}_0 \quad \text{on} \quad \partial\Omega_\text{v} \tag{4.73}$$

in the tentative velocity step, and choose the pressure correction boundary condition to best preserve this property in the corrected velocity. Taking the normal component of Eq. 4.68, we get the appropriate condition for $\frac{\partial p^n}{\partial n}$:

$$\frac{\partial}{\partial n}(p^n - p^{n-1})|_{\partial\Omega_\text{v}} = \frac{\rho}{\Delta t}(\boldsymbol{u}^* \cdot \hat{\boldsymbol{n}} - \boldsymbol{u}^n \cdot \hat{\boldsymbol{n}})|_{\partial\Omega_\text{v}} = 0. \tag{4.74}$$

Note that this only works for the normal component of $\boldsymbol{u}^n$. From Eq. 4.68, the actual conditions imposed on $\boldsymbol{u}^n$ are

$$\boldsymbol{u}^n = \boldsymbol{u}_0 - \frac{\Delta t}{\rho}\frac{\partial}{\partial \tau}(p^n - p^{n-1})\hat{\boldsymbol{\tau}} \qquad \text{on} \quad \partial\Omega_\text{v}, \tag{4.75}$$

where $\hat{\boldsymbol{\tau}}$ is the tangential unit vector at the boundary. Thus, we get an error in the tangential velocity component of first order in Δt. Moreover, additional restrictions are put on $\frac{\partial p^n}{\partial n}$. In particular, $\frac{\partial p^n}{\partial n} = \frac{\partial p^0}{\partial n}$.

The pseudo-traction condition in Eq. 4.72 is imitated by prescribing its separate parts:

$$\frac{\partial \boldsymbol{u}^*}{\partial n} = \frac{\partial \bar{\boldsymbol{u}}}{\partial n} \qquad \text{and} \qquad p^n = p_0 \qquad \text{on} \quad \partial\Omega_{\mathrm{v}} \tag{4.76}$$

in the tentative velocity step and pressure correction, respectively. In flow problems, we assume $\frac{\partial \boldsymbol{u}}{\partial n}$ to be small[1], and choose

$$\frac{\partial \bar{\boldsymbol{u}}}{\partial n} = 0 \qquad \text{and} \qquad p_0 = \bar{p}, \tag{4.77}$$

where $\bar{p}$ is the 'pressure' in the original pseudo-traction condition. We keep the generalized form to facilitate scheme verification through the method of manufactured solutions.

Modified Interface Conditions

Interface conditions are also changed by the operator splitting. In the tentative velocity step, we apply continuity of stress and the BJS condition (Eqs. 4.25 and 4.26), with the pressure replaced by its value in the previous step:

$$2\mu\hat{\boldsymbol{n}} \cdot \epsilon(\boldsymbol{u^*}_{\mathrm{v}}) \cdot \hat{\boldsymbol{n}} - p_{\mathrm{v}}^{n-1} = -p_{\mathrm{p}}^{n-1} + h_1, \tag{4.78}$$

$$2\hat{\boldsymbol{n}} \cdot \varepsilon(\boldsymbol{u^*}_{\mathrm{v}}) \cdot \hat{\boldsymbol{\tau}} = \alpha K^{-1/2} \boldsymbol{u^*}_{\mathrm{v}} \cdot \hat{\boldsymbol{\tau}} + h_2. \tag{4.79}$$

Only involving viscous unknowns, these act as boundary conditions for the viscous domain. Note that these conditions are imposed on the tentative velocity; they are not necessarily met by the corrected velocity.

We investigate three different sets of interface conditions applied in the pressure correction step. Normal derivatives of the pressure can be expressed through normal velocities using Eqs. 4.71 and 4.74. In the first approach, we simply omit the interface terms. This is equivalent to setting the normal velocity equal to the normal tentative velocity,

$$\boldsymbol{u}_v^n \cdot \hat{\boldsymbol{n}} = \boldsymbol{u}_v^* \cdot \hat{\boldsymbol{n}} \quad \text{and} \quad \boldsymbol{u}_p^n \cdot \hat{\boldsymbol{n}} = \boldsymbol{u}_p^* \cdot \hat{\boldsymbol{n}}. \tag{4.80}$$

The resulting scheme does not impose the mass conservation interface condition (Eq. 4.24). This can be included by replacing one of the conditions by

$$\boldsymbol{u}_v^n \cdot \hat{\boldsymbol{n}} = \boldsymbol{u}_p^n \cdot \hat{\boldsymbol{n}}. \tag{4.81}$$

[1] This was the motivation for choosing the pseudo-traction condition in the first place (Sec. 3.4.4).

The appropriate interface conditions are derived from Eqs. 4.71 and 4.74. Replacing the condition on the porous velocity we get

$$\frac{\partial}{\partial n}(p_p^n - p_p^{n-1}) = \left(\frac{1}{\phi} + \beta\frac{\mu\Delta t}{K\rho}\right)\frac{\partial}{\partial n}(p_v^n - p_v^{n-1}) + \left(\frac{\rho}{\phi\Delta t} + \beta\frac{\mu}{K}\right)(\boldsymbol{u}_p^* - \boldsymbol{u}_v^*)\cdot\hat{\boldsymbol{n}}. \tag{4.82}$$

Similarly, replacing the viscous velocity we get

$$\frac{\partial}{\partial n}(p_v^n - p_v^{n-1}) = \left(\frac{1}{\phi} + \beta\frac{\mu\Delta t}{K\rho}\right)^{-1}\frac{\partial}{\partial n}(p_p^n - p_p^{n-1}) + \frac{\rho}{\Delta t}(\boldsymbol{u}_v^* - \boldsymbol{u}_p^*)\cdot\hat{\boldsymbol{n}}. \tag{4.83}$$

We include a switch, γ such that $\gamma = 0$ omits the interface terms, $\gamma = 1$ applies Eq. 4.82 and $\gamma = 2$ applies Eq. 4.83.

Discrete Variational Forms

The tentative velocity step is equivalent to the coupled scheme equation of motion with the pressure, p^n, replaced by the previous pressure, p^{n-1}. We take the inner product with a test function, $\boldsymbol{v}$, and integrate the viscous stress term by parts in order to imitate the coupled scheme. The resulting variational form is equal to the coupled, with the replacements:

$$p^n \to p^{n-1} \qquad \text{and} \qquad \bar{p}\hat{\boldsymbol{n}} \to p^{n-1}\hat{\boldsymbol{n}} - \frac{\partial\bar{\boldsymbol{u}}}{\partial n}. \tag{4.84}$$

The pressure correction is a simple Poisson equation. We take the inner product with a test function, q,

$$\langle\nabla^2 p^n,\, q\rangle_\Omega = \langle\nabla^2 p^{n-1},\, q\rangle_\Omega + \frac{\rho}{\Delta t}\langle\boldsymbol{\nabla}\cdot\boldsymbol{u}^* - g,\, q\rangle_{\Omega_\mathrm{v}} + \left(\frac{\rho}{\phi\Delta t} + \beta\frac{\mu}{K}\right)\langle\boldsymbol{\nabla}\cdot\boldsymbol{u}^* - g,\, q\rangle_{\Omega_\mathrm{p}}, \tag{4.85}$$

and integrate the second order terms by parts,

$$\langle\nabla^2 p,\, q\rangle_\Omega = -\langle\boldsymbol{\nabla}p,\, \boldsymbol{\nabla}q\rangle_\Omega + \langle\frac{\partial p}{\partial n},\, q\rangle_{\partial\Omega} + \langle\frac{\partial p_p}{\partial n},\, q_p\rangle_\Gamma - \langle\frac{\partial p_v}{\partial n},\, q_v\rangle_\Gamma. \tag{4.86}$$

Imposing the Neumann boundary conditions in Eqs. 4.71 and 4.74, and including the interface conditions discussed in the preceding paragraph, we

get

$$\begin{aligned}\langle \nabla p^n,\, \nabla q\rangle_\Omega + I(p^n)_\gamma = \langle \nabla p^{n-1},\, \nabla q\rangle_\Omega &- \frac{\rho}{\Delta t}\langle \nabla\cdot \boldsymbol{u}^* - g,\, q\rangle_{\Omega_\mathrm{v}} \\ &- \left(\frac{\rho}{\phi\Delta t} + \beta\frac{\mu}{K}\right)\langle \nabla\cdot \boldsymbol{u}^* - g,\, q\rangle_{\Omega_\mathrm{p}} \\ &+ \left(\frac{\rho}{\phi\Delta t} + \beta\frac{\mu}{K}\right)\langle \boldsymbol{u}^*\cdot\hat{\boldsymbol{n}} - \bar{\boldsymbol{u}}\cdot\hat{\boldsymbol{n}},\, q\rangle_{\partial\Omega_\mathrm{p}} \\ &+ I(p^{n-1})_\gamma, \end{aligned} \tag{4.87}$$

where

$$I_\gamma(p) = \begin{cases} 0 & \text{if } \gamma = 0, \\ -\left(\frac{1}{\phi} + \beta\frac{\mu\Delta t}{K\rho}\right)\langle \frac{\partial p_v}{\partial n},\, q_p\rangle_\Gamma & \text{if } \gamma = 1, \\ \left(\frac{1}{\phi} + \beta\frac{\mu\Delta t}{K\rho}\right)^{-1}\langle \frac{\partial p_p}{\partial n},\, q_v\rangle_\Gamma & \text{if } \gamma = 2. \end{cases} \tag{4.88}$$

Note that we have omitted interface terms involving $\boldsymbol{u}_v^* - \boldsymbol{u}_p^*$; these are zero when applying continuous elements. The variational form for the velocity correction is trivial as this is a pure projection step.

The final IPCS scheme is given by the following three steps. As before, we include both generalized versions and the forms used in flow simulations.

1. Tentative velocity step:

   Discrete Variational Form 4.3.3 (tentative velocity, generalized). *Find a function $\boldsymbol{u}^* \in \boldsymbol{V}_h$ such that for all $\boldsymbol{v} \in \hat{\boldsymbol{V}}_h$*

   $$a(\boldsymbol{u}^*, \boldsymbol{v}) = L(\boldsymbol{v}) - b(p^{n-1}, \boldsymbol{v}), \tag{4.89}$$

   where a and b are given by the corresponding expressions in the coupled scheme (Eqs. 4.41 and 4.42):

   $$\begin{aligned} a(\boldsymbol{u}^*, \boldsymbol{v}) = \frac{\rho}{\Delta t}\langle \boldsymbol{u}^*,\, \boldsymbol{v}\rangle_{\Omega_v} &+ \rho\langle \boldsymbol{u}^{n-1}\cdot\nabla\boldsymbol{u}^*,\, \boldsymbol{v}\rangle_{\Omega_v} + 2\mu\langle \epsilon(\boldsymbol{u}^*),\, \epsilon(\boldsymbol{v})\rangle_{\Omega_v} \\ &- \mu\langle \hat{\boldsymbol{n}}\cdot(\nabla\boldsymbol{u}^*)^T,\, \boldsymbol{v}\rangle_{\partial\Omega_v} + \left(\frac{\rho}{\phi\Delta t} + \frac{\mu}{K}\right)\langle \boldsymbol{u}^*,\, \boldsymbol{v}\rangle_{\Omega_p} \\ &+ \mu\alpha K^{-\frac{1}{2}}\langle \boldsymbol{u}_v^*\cdot\hat{\boldsymbol{\tau}},\, \boldsymbol{v}_v\cdot\hat{\boldsymbol{\tau}}\rangle_\Gamma, \end{aligned} \tag{4.90}$$

   $$\begin{aligned} b(p^{n-1}, \boldsymbol{v}) = &-\langle p^{n-1},\, \nabla\cdot\boldsymbol{v}\rangle_{\Omega_v} + \langle \nabla p^{n-1},\, \boldsymbol{v}\rangle_{\Omega_p} \\ &- \langle p_p^{n-1},\, \boldsymbol{v}_v\cdot\hat{\boldsymbol{n}}\rangle_\Gamma, \end{aligned} \tag{4.91}$$

   and $L(\boldsymbol{v})$ is given by

   $$\begin{aligned} L(\boldsymbol{v}) = \frac{\rho}{\Delta t}\langle \boldsymbol{u}^{n-1},\, \boldsymbol{v}\rangle_{\Omega_v} &+ \frac{\rho}{\phi\Delta t}\langle \boldsymbol{u}^{n-1},\, \boldsymbol{v}\rangle_{\Omega_p} + \langle \boldsymbol{f}^n,\, \boldsymbol{v}\rangle_\Omega \\ &- \langle p^{n-1}\hat{\boldsymbol{n}},\, \boldsymbol{v}\rangle_{\partial\Omega_v} - \langle h_1\hat{\boldsymbol{n}} + \mu h_2\hat{\boldsymbol{\tau}},\, \boldsymbol{v}_v\rangle_\Gamma \\ &+ \mu\langle \frac{\partial\bar{\boldsymbol{u}}}{\partial n},\, \boldsymbol{v}\rangle_{\partial\Omega_v}. \end{aligned} \tag{4.92}$$

Discrete Variational Form 4.3.4 (tentative velocity, flow problems). *Find a function* $\boldsymbol{u}^* \in \boldsymbol{V}_h$ *such that for all* $\boldsymbol{v} \in \hat{\boldsymbol{V}}_h$

$$a(\boldsymbol{u}^*, \boldsymbol{v}) = L(\boldsymbol{v}) - b(p^{n-1}, \boldsymbol{v}), \tag{4.93}$$

where a *and* b *are given by the corresponding expressions in the coupled scheme (Eqs. 4.47 and 4.48):*

$$\begin{aligned} a(\boldsymbol{u}^*, \boldsymbol{v}) = &\frac{\rho}{\Delta t}\langle \boldsymbol{u}^*,\ \boldsymbol{v}\rangle_{\Omega_v} + \rho\langle \boldsymbol{u}^{n-1}\cdot\boldsymbol{\nabla}\boldsymbol{u}^*,\ \boldsymbol{v}\rangle_{\Omega_v} + 2\mu\langle \epsilon(\boldsymbol{u}^*),\ \epsilon(\boldsymbol{v})\rangle_{\Omega_v} \\ &- \mu\langle \hat{\boldsymbol{n}}\cdot(\boldsymbol{\nabla}\boldsymbol{u}^*)^T,\ \boldsymbol{v}\rangle_{\partial\Omega_v} + \left(\frac{\rho}{\phi\Delta t} + \frac{\mu}{K}\right)\langle \boldsymbol{u}^*,\ \boldsymbol{v}\rangle_{\Omega_p} \\ &+ \mu\alpha K^{-\frac{1}{2}}\langle \boldsymbol{u}_v^*\cdot\hat{\boldsymbol{\tau}},\ \boldsymbol{v}_v\cdot\hat{\boldsymbol{\tau}}\rangle_\Gamma, \end{aligned} \tag{4.94}$$

$$\begin{aligned} b(p^{n-1}, \boldsymbol{v}) = &-\langle p^{n-1},\ \boldsymbol{\nabla}\cdot\boldsymbol{v}\rangle_{\Omega_v} + \langle \boldsymbol{\nabla}p^{n-1},\ \boldsymbol{v}\rangle_{\Omega_p} \\ &- \langle p_p^{n-1},\ \boldsymbol{v}_v\cdot\hat{\boldsymbol{n}}\rangle_\Gamma, \end{aligned} \tag{4.95}$$

and $L(\boldsymbol{v})$ *is given by*

$$L(\boldsymbol{v}) = \frac{\rho}{\Delta t}\langle \boldsymbol{u}^{n-1},\ \boldsymbol{v}\rangle_{\Omega_v} + \frac{\rho}{\phi\Delta t}\langle \boldsymbol{u}^{n-1},\ \boldsymbol{v}\rangle_{\Omega_p} - \langle p^{n-1}\hat{\boldsymbol{n}},\ \boldsymbol{v}\rangle_{\partial\Omega_v} \tag{4.96}$$

2. Pressure correction:

Discrete Variational Form 4.3.5 (pressure correction, generalized). *Find a function* $p \in Q_h$ *such that for all* $q \in \hat{Q}_h$

$$\begin{aligned} \langle \boldsymbol{\nabla}p^n,\ \boldsymbol{\nabla}q\rangle_\Omega + I_\gamma(p^n) = &\langle \boldsymbol{\nabla}p^{n-1},\ \boldsymbol{\nabla}q\rangle_\Omega - \frac{\rho}{\Delta t}\langle \boldsymbol{\nabla}\cdot\boldsymbol{u}^* - g,\ q\rangle_{\Omega_v} \\ &- \left(\frac{\rho}{\phi\Delta t} + \beta\frac{\mu}{K}\right)\langle \boldsymbol{\nabla}\cdot\boldsymbol{u}^* - g,\ q\rangle_{\Omega_p} \\ &+ \left(\frac{\rho}{\phi\Delta t} + \beta\frac{\mu}{K}\right)\langle \boldsymbol{u}^*\cdot\hat{\boldsymbol{n}} - \bar{\boldsymbol{u}}\cdot\hat{\boldsymbol{n}},\ q\rangle_{\partial\Omega_p} \\ &+ I_\gamma(p^{n-1}), \end{aligned} \tag{4.97}$$

where

$$I_\gamma(p) = \begin{cases} 0 & \text{if } \gamma = 0, \\ -\left(\frac{1}{\phi} + \beta\frac{\mu\Delta t}{K\rho}\right)\langle \frac{\partial p_v}{\partial n},\ q_p\rangle_\Gamma & \text{if } \gamma = 1, \\ \left(\frac{1}{\phi} + \beta\frac{\mu\Delta t}{K\rho}\right)^{-1}\langle \frac{\partial p_p}{\partial n},\ q_v\rangle_\Gamma & \text{if } \gamma = 2. \end{cases} \tag{4.98}$$

Discrete Variational Form 4.3.6 (pressure correction, flow problems). *Find a function* $p \in Q_h$ *such that for all* $q \in \hat{Q}_h$

$$\begin{aligned} \langle \boldsymbol{\nabla}p^n,\ \boldsymbol{\nabla}q\rangle_\Omega + I_\gamma(p^n) = &\langle \boldsymbol{\nabla}p^{n-1},\ \boldsymbol{\nabla}q\rangle_\Omega - \frac{\rho}{\Delta t}\langle \boldsymbol{\nabla}\cdot\boldsymbol{u}^*,\ q\rangle_{\Omega_v} \\ &- \left(\frac{\rho}{\phi\Delta t} + \beta\frac{\mu}{K}\right)\langle \boldsymbol{\nabla}\cdot\boldsymbol{u}^*,\ q\rangle_{\Omega_p} \\ &+ \left(\frac{\rho}{\phi\Delta t} + \beta\frac{\mu}{K}\right)\langle \boldsymbol{u}^*\cdot\hat{\boldsymbol{n}} - \bar{\boldsymbol{u}}\cdot\hat{\boldsymbol{n}},\ q\rangle_{\partial\Omega_p} \\ &+ I_\gamma(p^{n-1}), \end{aligned} \tag{4.99}$$

where

$$I_\gamma(p) = \begin{cases} 0 & \text{if } \gamma = 0, \\ -\left(\frac{1}{\phi} + \beta\frac{\mu\Delta t}{K\rho}\right)\langle\frac{\partial p_v}{\partial n},\, q_p\rangle_\Gamma & \text{if } \gamma = 1, \\ \left(\frac{1}{\phi} + \beta\frac{\mu\Delta t}{K\rho}\right)^{-1}\langle\frac{\partial p_p}{\partial n},\, q_v\rangle_\Gamma & \text{if } \gamma = 2. \end{cases} \tag{4.100}$$

3. Velocity correction:

   Discrete Variational Form 4.3.7 (velocity correction)**.** *Find a function* $\boldsymbol{u}^n \in \boldsymbol{V}_h$ *such that for all* $\boldsymbol{v} \in \hat{\boldsymbol{V}}_h$

$$\langle \boldsymbol{u}^n,\, \boldsymbol{v}\rangle_\Omega = \langle \boldsymbol{u}^*,\, \boldsymbol{v}\rangle_\Omega - \frac{\Delta t}{\rho}\langle \boldsymbol{\nabla}(p^n - p^{n-1}),\, \boldsymbol{v}\rangle_{\Omega_v} - \left(\frac{\rho}{\phi\Delta t} + \beta\frac{\mu}{K}\right)^{-1}\langle \boldsymbol{\nabla}(p^n - p^{n-1}),\, \boldsymbol{v}\rangle_{\Omega_p}. \tag{4.101}$$

   This form is the same whether we consider flow problems or the generalized case.

Implementation in FEniCS

The FEniCS implementation of the IPCS variational forms are given in listing 4.3. As for the coupled scheme, the variational forms are primarily defined for flow problems; an if-test is used to add generalizations used in verification tests. In addition to the remarks on the coupled scheme implementation, note the following:

- The forms a2 and a3 are defined as integrations over the entire domain. For this to work properly, they need to be assembled without specifying cell domains.

Listing 4.3: Implementation of variational form for the IPCS.

```
# Define variational problem
# - trial and test functions
u = TrialFunction(V)
v = TestFunction(V)
p = TrialFunction(Q)
q = TestFunction(Q)
# - help functions
u1 = Function(V) # previous velocity
p1 = Function(Q) # previous pressure
u0 = Function(V) # tentative velocity
p0 = Function(Q) # corrected pressure
n = FacetNormal(mesh)

# 1) Tentative velocity step
c1 = rho/dt*inner(u, v)*dx(fluid_domain) \
```

```
    + 2*mu*inner(epsilon(u), epsilon(v))*dx(fluid_domain) \
    - mu*inner(grad(u).T*n, v)*ds(fluid_inlet) \
    + (rho/(dt*phi) + mu/K)*inner(u, v)*dx(porous_domain) \
    + mu*alpha/sqrt(K)*u('-')[1]*v('-')[1]*dS(interface_y) \
    + mu*alpha/sqrt(K)*u('-')[0]*v('-')[0]*dS(interface_x)

d1 = rho*inner(grad(u)*u1, v)*dx(fluid_domain) # not constant

b0 = -p1*div(v)*dx(fluid_domain) \
    + inner(grad(p1), v)*dx(porous_domain) \
    - p1('+')*inner(v('-'), n('+'))*dS(interface)

L0 = rho/dt*inner(u1, v)*dx(fluid_domain) \
    + rho/(dt*phi)*inner(u1, v)*dx(porous_domain) \
    - inner(v, p1*n)*ds(fluid_inlet)

L1 = L0 - b0 # collect RHS

# 2) Pressure correction step
a2 = inner(grad(q), grad(p))*dx
L2 = inner(grad(q), grad(p1))*dx(fluid_domain) \
    - rho/dt*q*div(u0)*dx(fluid_domain) \
    + inner(grad(q), grad(p1))*dx(porous_domain) \
    - (rho/(phi*dt)+beta*mu/K)*q*div(u0)*dx(porous_domain) \
    + (rho/(phi*dt)+beta*mu/K)*inner(u0, n)*q*ds(porous_wall) \
    + (rho/(phi*dt)+beta*mu/K) \
    *inner(u0 - ubar, n)*q*ds(porous_inlet)

# Interface conditions on pressure eq. (gamma-switch)
C = 1.0/phi + beta*mu/(rho*K)*dt
if gamma == 1:
    a2 += -C*inner(grad(p('-')),q('+')*n('+'))*dS(interface)
    L2 += -C*inner(grad(p1('-')),q('+')*n('+'))*dS(interface)
elif gamma == 2:
    a2 += 1.0/C*inner(grad(p('+')),q('-')*n('+'))*dS(interface)
    L2 += 1.0/C*inner(grad(p1('+')),q('-')*n('+'))*dS(interface)

# 3) Velocity correction step
a3 = inner(v, u)*dx
L3 = inner(v, u0)*dx(fluid_domain) \
    - dt/rho*inner(v, grad(p0 - p1))*dx(fluid_domain) \
    + inner(v, u0)*dx(porous_domain) \
    - 1.0/(rho/(phi*dt)+beta*mu/K)*inner(v, grad(p0 - p1))\
    *dx(porous_domain)

# Additions in test case
if isinstance(problem, TestCase):
    L1 += inner(ff, v)*dx(fluid_domain) \
        + inner(fp, v)*dx(porous_domain) \
        - h1('-')*inner(v('-'), n('+'))*dS(interface) \
        - mu*h2('-')*v('-')[1]*dS(interface)

    # generalization of du/dn
    L1 += mu*inner(gradu*n, v)*ds(fluid_inlet)
```

```
L2 += + rho/dt*gf*q*dx(fluid_domain) \
     + (rho/(phi*dt)+beta*mu/K)*gp*q*dx(porous_domain)

# generalized slip boundary condition
L2 += -(rho/(phi*dt) + beta*mu/K)*inner(ubar, n)*q\
*ds(porous_wall)
```

4.3.4 Brinkman Scheme

A simpler solution strategy is based on the Brinkman porous media equation (Nield and Bejan, 2006, Sec. 1.5.3):

$$\rho\left(\frac{1}{\phi}\frac{\partial \boldsymbol{u}}{\partial t} + \boldsymbol{u}\cdot\boldsymbol{\nabla}\boldsymbol{u}\right) = \boldsymbol{\nabla}\cdot\sigma(\boldsymbol{u},p) - \frac{\mu}{K}\boldsymbol{u} + \boldsymbol{f}. \tag{4.102}$$

If $\phi = 1$ and $K \to \infty$, the Brinkman equation limits to the Navier-Stokes equation. If $K \to 0$, Darcy's law is returned. Since the spinal cord permeability is estimated to be of the order $10^{-15}\,\mathrm{m}^2$, it seems reasonable to apply the Brinkman equation on the entire flow domain, using discontinuous parameters to separate viscous and porous parts. To account for an infinite permeability in the viscous domain, we introduce a parameter C, such that

$$C = \begin{cases} 0 & \text{on } \Omega_\mathrm{v}, \\ \mu/K & \text{on } \Omega_\mathrm{p}. \end{cases}$$

Temporal Discretization

We apply the incremental pressure correction scheme on the Brinkman equation. First, a tentative velocity is computed using a semi-implicit temporal discretization and the pressure from the previous time step,

$$\rho\left(\frac{\boldsymbol{u}^* - \boldsymbol{u}^{n-1}}{\phi\Delta t} + \boldsymbol{u}^{n-1}\cdot\boldsymbol{\nabla}\boldsymbol{u}^*\right) = \boldsymbol{\nabla}\cdot\sigma(\boldsymbol{u}^*, p^{n-1}) - C\boldsymbol{u}^* + \boldsymbol{f}^n. \tag{4.103}$$

Using a β-switch, as explained in Sec. 4.3.3, the corrected velocity can be expressed as

$$\boldsymbol{u}^n = \boldsymbol{u}^* - \left(\frac{\rho}{\phi\Delta t} + \beta C\right)^{-1}\boldsymbol{\nabla}(p^n - p^{n-1}), \tag{4.104}$$

where implicit terms of the order Δt have been discarded. Applying the equation of continuity, the corrected pressure is given by

$$\boldsymbol{\nabla}^2 p^n = \boldsymbol{\nabla}^2 p^{n-1} + \left(\frac{\rho}{\phi\Delta t} + \beta C\right)(\boldsymbol{\nabla}\cdot\boldsymbol{u}^* - g). \tag{4.105}$$

Note on Boundary and Interface Conditions

The Brinkman model introduces additional conditions on the porous boundary. In particular, we apply no-slip or pseudo-traction conditions on the entire boundary. As this is an incremental pressure correction scheme, we use the modified conditions introduced in Sec. 4.3.3.

Since the Brinkman model is used on the entire domain, no interface conditions are imposed explicitly.

Discrete Variational Forms

The variational forms of the Brinkman scheme are similar to the forms introduced over the viscous domain in Sec. 4.3.3. The only difference is that a Darcy drag term is added, and the interface terms omitted. We include only forms used in flow problems.

1. Tentative velocity step:

   Discrete Variational Form 4.3.8 (tentative velocity, flow problems)**.** *Find a function* $\boldsymbol{u}^* \in \boldsymbol{V}_h$ *such that for all* $\boldsymbol{v} \in \hat{\boldsymbol{V}}_h$

   $$a(\boldsymbol{u}^*, \boldsymbol{v}) = L(\boldsymbol{v}), \tag{4.106}$$

   where a *and* L *are given by*

   $$\begin{aligned} a(\boldsymbol{u}^*, \boldsymbol{v}) = \left(\frac{\rho}{\phi \Delta t} + C\right) \langle \boldsymbol{u}^*,\, \boldsymbol{v} \rangle_\Omega + \rho \langle \boldsymbol{u}^{n-1} \cdot \boldsymbol{\nabla} \boldsymbol{u}^*,\, \boldsymbol{v} \rangle_\Omega \\ + 2\mu \langle \epsilon(\boldsymbol{u}^*),\, \epsilon(\boldsymbol{v}) \rangle_\Omega - \mu \langle \hat{\boldsymbol{n}} \cdot (\boldsymbol{\nabla} \boldsymbol{u}^*)^T,\, \boldsymbol{v} \rangle_{\partial\Omega}, \end{aligned} \tag{4.107}$$

   $$L(\boldsymbol{v}) = \frac{\rho}{\phi \Delta t} \langle \boldsymbol{u}^{n-1},\, \boldsymbol{v} \rangle_\Omega + \langle p^{n-1} \hat{\boldsymbol{n}},\, \boldsymbol{v} \rangle_\Omega - \langle p^{n-1} \hat{\boldsymbol{n}},\, \boldsymbol{v} \rangle_{\partial\Omega}. \tag{4.108}$$

2. Pressure correction:

   Discrete Variational Form 4.3.9 (pressure correction, flow problems)**.** *Find a function* $p \in Q_h$ *such that for all* $q \in \hat{Q}_h$

   $$\langle \boldsymbol{\nabla} p^n,\, \boldsymbol{\nabla} q \rangle_\Omega = \langle \boldsymbol{\nabla} p^{n-1},\, \boldsymbol{\nabla} q \rangle_\Omega - \left(\frac{\rho}{\phi \Delta t} + \beta C\right) \langle \boldsymbol{\nabla} \cdot \boldsymbol{u}^*,\, q \rangle_\Omega. \tag{4.109}$$

3. Velocity correction:

   Discrete Variational Form 4.3.10 (velocity correction)**.** *Find a function* $\boldsymbol{u}^n \in \boldsymbol{V}_h$ *such that for all* $\boldsymbol{v} \in \hat{\boldsymbol{V}}_h$

   $$\langle \boldsymbol{u}^n,\, \boldsymbol{v} \rangle_\Omega = \langle \boldsymbol{u}^*,\, \boldsymbol{v} \rangle_\Omega - \left(\frac{\rho}{\phi \Delta t} + \beta C\right)^{-1} \langle \boldsymbol{\nabla}(p^n - p^{n-1}),\, \boldsymbol{v} \rangle_\Omega. \tag{4.110}$$

Implementation in FEniCS

The implemented Brinkman scheme is included in listing 4.4. This uses discontinuous functions, ϕ and C, created by the following statements:

```
DG = FunctionSpace(mesh, 'DG', 0)
u = TrialFunction(DG)
v = TestFunction(DG)

a = u*v*dx
L_C = Constant(mu/K)*v*dx(porous_domain)
L_phi = phi*v*dx(porous_domain) + 1.0*v*dx(fluid_domain)

A = assemble(a)
b_C = assemble(L_C, cell_domains=cell_domains)
b_phi = assemble(L_phi, cell_domains=cell_domains)

C = Function(DG)
phi = Function(DG)
solve(A, C.vector(), b_C)
solve(A, phi.vector(), b_phi)
```

The 'DG' function space defines piecewise constants over the domain. Separate projections on porous and viscous domains creates discontinuous functions for parameters ϕ and C.

Listing 4.4: Implementation of variational form in Brinkman scheme.

```
# Define variational problem
# - trial and test functions
u = TrialFunction(V)
v = TestFunction(V)
p = TrialFunction(Q)
q = TestFunction(Q)
# - help functions
u1 = Function(V) # previous velocity
p1 = Function(Q) # previous pressure
u0 = Function(V) # tentative velocity
p0 = Function(Q) # corrected pressure
n = FacetNormal(mesh)

# 1) Tentative velocity step
c1 = (rho/(dt*phi) + C)*inner(u, v)*dx \
    + 2*mu*inner(epsilon(u), epsilon(v))*dx \
    - mu*inner(grad(u).T*n, v)*ds

d1 = rho*inner(grad(u)*u1, v)*dx # not constant

L1 = rho/(dt*phi)*inner(u1, v)*dx \
    + p1*div(v)*dx
    - inner(v, p1*n)*ds

# 2) Pressure correction step
a2 = inner(grad(q), grad(p))*dx
```

```
L2 = inner(grad(q), grad(p1))*dx \
    - (rho/(phi*dt)+beta*C)*q*div(u0)*dx

# 3) Velocity correction step
a3 = inner(v, u)*dx
L3 = inner(v, u0)*dx \
    - 1.0/(rho/(phi*dt)+beta*C)*inner(v, grad(p0 - p1))*dx
```

4.4 Finite Elements

In initial investigations we apply Taylor-Hood finite elements. Quadratic Lagrange elements are used for the velocity field and linear Lagrange elements for the pressure field. Taylor-Hood elements fulfill the Babuska-Brezzi condition, ensuring a non-singular matrix in the linear system resulting from the mixed formulation (e.g. Langtangen et al., 2002). The operator-splitting schemes do not need to fulfill this condition. This is a great advantage as it could be possible to apply linear elements for both velocity and pressure, significantly increasing efficiency.

4.5 Linear Solvers

Due to stability problems, direct linear solvers are applied. This is, however, not feasible for applications on full three-dimensional domains. In this case, appropriate iterative solvers are needed. These are simpler do develop for the operator-splitting schemes than for the fully coupled discretization.

Chapter 5

Numerical Experiments on Accuracy and Convergence Properties of the Numerical Schemes

Accuracy and convergence properties of the coupled scheme and the IPCS are investigated by numerical experiments using the method of manufactured solutions. In particular, we

1. Verify that numerical solutions converge to known analytical solutions, and that convergence rates are in accordance with theoretical estimates.

2. Investigate how coupling affects accuracy, evaluated separately for viscous and porous regions.

3. Investigate how accuracy is affected by a change in problem parameters. In particular, we compare the choice of all parameters equal to one to realistic parameters for spinal canal flow problems.

4. Evaluate accuracy of the IPCS compared to the coupled scheme.

Evaluations on stability are also made. However, this is handled more thoroughly in flow experiments (Sec. 6.2). The Brinkman scheme is not considered until the next chapter.

The outline of this chapter is as follows. We first present theoretical convergence estimates in Sec. 5.1. Then, numerical experiments and error measurements are described in Sec. 5.2–5.3. Finally, the results are presented in Sec. 5.4.

5.1 Convergence Estimates

5.1.1 Estimates for Stationary Solutions

We present known convergence estimates for Taylor-Hood elements applied to mixed formulations of the stationary Navier-Stokes and Darcy problems.

Viscous Equations

Given a sufficiently smooth solution and a convex computational domain, Taylor-Hood elements applied to the stationary, linear Stokes problem should yield third order convergence in velocity and second order convergence in pressure (Mardal and Langtangen, 2003, Eqs. 4.69–4.71). The stationary Navier-Stokes system includes an additional non-linear convection term, expected to reduce convergence in velocity to second order (Elman et al., 2005, Eq. 7.56).

Porous Equations

Applied to the stationary Darcy problem, Taylor-Hood elements are estimated to have equal convergence properties as the Mini element (Karper, 2006). The latter has been shown to yield linear convergence in velocity and quadratic convergence in pressure (Mardal et al., 2002; Mardal and Langtangen, 2003).

5.1.2 Error in the Temporal Discretization

From the backward Euler temporal scheme and the omitted terms in the IPCS we expect linear convergence in the time discretization parameter.

5.2 Numerical Experiments

A measure of the order of accuracy is obtained by comparing numerical solutions to known analytical solutions. In this respect, we apply the method of manufactured solutions. That is, instead of comparing with a physical solution of the Navier-Stokes/Darcy system, the equations are generalized in order to yield an arbitrary, 'manufactured' solution.

5.2.1 Numerical Experiments

We apply the generalized equations introduced in Sec. 4.3.1. Tests are performed separately for the viscous and porous equations in addition to a coupled problem. Both stationary and non-stationary manufactured solutions

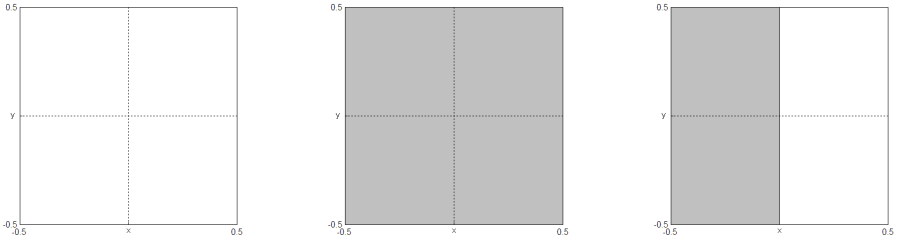

(a) Pure viscous domain (b) Pure porous domain (c) Split domain

Figure 5.1: Illustration of tests domains. Numerical experiments are performed on two-dimensional unit squares for pure viscous (a) and porous (b) domains, and for a split domain (c) comprised of a porous part in $x < 0$ and a viscous part in $x > 0$.

are considered. We investigate the simple case with all problem parameters set equal to one,

$$\mu = \rho = \phi = K = \alpha = 1,$$

and with realistic problem parameters for spinal canal flow (Tbl. 3.1).

Test are performed for the coupled scheme and the IPCS. In the latter case, we use $\beta = 1$ in porous domains, and $\gamma = 1$ in the pressure correction interface condition. Discretization parameters

$$h, \Delta t = 0.2, 0.1, 0.05, 0.025, 0.0125,$$

are applied, each differing by a factor 2. Smaller discretization parameters are used when this is necessary to obtain stable solutions.

5.2.2 Test Domains

Numerical experiments are performed on a two-dimensional unit square with ranges $[-0.5\,\text{cm}, 0.5\,\text{cm}] \times [-0.5\,\text{cm}, 0.5\,\text{cm}]$. In the coupled problem, the unit square is split in half, governed by the porous equations in $x < 0$ and the viscous equations in $x > 0$ (Fig. 5.1).

5.2.3 Manufactured Solutions

Stationary Solution

The choice of stationary, analytical solution is

$$\boldsymbol{u}_e = \cos(xy)\hat{\boldsymbol{\imath}} + \exp(x+y)\hat{\boldsymbol{\jmath}}, \tag{5.1}$$

$$p_e = \exp(x)\sin(x+y) - C, \tag{5.2}$$

where $\hat{\boldsymbol{\imath}}$ and $\hat{\boldsymbol{\jmath}}$ are the unit vectors in the x- and y-directions, respectively. C is a constant added for a normalized pressure, i.e. that the integrated pressure over the domain is zero. Using the unit square domain,

$$C = \int_{-0.5}^{0.5}\int_{-0.5}^{0.5} \exp(x)\sin(x+y)\,\mathrm{d}x\,\mathrm{d}y = 0.07988047615599. \tag{5.3}$$

Inserting the manufactured solution into the generalized equations, we get volume forces

$$\begin{aligned}
\boldsymbol{f}_v &= \rho\left(\frac{\partial \boldsymbol{u}_e}{\partial t} + \boldsymbol{u}_e\cdot\boldsymbol{\nabla}\boldsymbol{u}_e\right) - \boldsymbol{\nabla}\cdot\sigma(\boldsymbol{u}_e, p_e) \\
&= \rho\boldsymbol{u}_e\cdot\boldsymbol{\nabla}\boldsymbol{u}_e + \boldsymbol{\nabla}p_e - \mu\left(\nabla^2\boldsymbol{u}_e + \boldsymbol{\nabla}(\boldsymbol{\nabla}\cdot\boldsymbol{u}_e)\right) \\
&= \rho\begin{pmatrix} -y\sin(xy) & -xsin(xy) \\ \exp(x+y) & \exp(x+y)\end{pmatrix}\begin{pmatrix}\cos(xy)\\ \exp(x+y)\end{pmatrix} \\
&\quad + \begin{pmatrix}\exp(x)\sin(x+y) + cos(x+y)\\ \exp(x)\cos(x+y)\end{pmatrix} \\
&\quad - \mu\left[\begin{pmatrix}-(x^2+y^2)\cos(xy)\\ 2\exp(x+y)\end{pmatrix}\right. \\
&\qquad \left. + \begin{pmatrix}-y^2 cos(xy) + \exp(x+y)\\ -\sin(xy) - xy\cos(xy) + \exp(x+y)\end{pmatrix}\right],
\end{aligned} \tag{5.4}$$

$$\begin{aligned}
\boldsymbol{f}_p &= \frac{\rho}{\phi}\frac{\partial \boldsymbol{u}_e}{\partial t} + \boldsymbol{\nabla}p_e + \frac{\mu}{K}\boldsymbol{u}_e \\
&= \begin{pmatrix}\exp(x)\sin(x+y) + cos(x+y)\\ \exp(x)\cos(x+y)\end{pmatrix} + \frac{\mu}{K}\begin{pmatrix}\cos(xy)\\ \exp(x+y)\end{pmatrix},
\end{aligned} \tag{5.5}$$

in the viscous and porous domain, respectively, and generalizations

$$\begin{aligned}
g &= \boldsymbol{\nabla}\cdot\boldsymbol{u}_e \\
&= -y\sin(xy) + \exp(x+y), && (5.6)\\
h_1 &= 2\mu\hat{\boldsymbol{n}}\cdot\epsilon(\boldsymbol{u}_{e,\mathrm{v}})\cdot\hat{\boldsymbol{n}} - p_{e,\mathrm{v}} + p_{e,\mathrm{p}} \\
&= -2\mu y\sin(xy), && (5.7)\\
h_2 &= 2\hat{\boldsymbol{n}}\cdot\varepsilon(\boldsymbol{u}_{e,\mathrm{v}})\cdot\hat{\boldsymbol{\tau}} - \alpha K^{-1/2}\boldsymbol{u}_{e,\mathrm{v}}\cdot\hat{\boldsymbol{\tau}} \\
&= \exp(x+y) - x\sin(xy) - \frac{\alpha}{\sqrt{K}}\exp(x+y), && (5.8)
\end{aligned}$$

where we have defined $\hat{\boldsymbol{\tau}}$ to be the tangential in the positive y-direction. The Neumann boundary conditions are given by

$$\begin{aligned}
\bar{p}\hat{\boldsymbol{n}} &= p_e\hat{\boldsymbol{n}} - \mu\frac{\partial \boldsymbol{u}_e}{\partial n} \\
&= \left[p_e\mathbb{I} - \mu(\boldsymbol{\nabla}\boldsymbol{u})^T\right]\cdot\hat{\boldsymbol{n}} \\
&= \left[p_e\begin{pmatrix}1 & 0\\ 0 & 1\end{pmatrix} - \mu\begin{pmatrix}-y\sin(xy) & -xsin(xy)\\ \exp(x+y) & \exp(x+y)\end{pmatrix}\right]\cdot\hat{\boldsymbol{n}}, \qquad (5.9)\\
\frac{\partial\bar{\boldsymbol{u}}}{\partial n} &= \frac{\partial \boldsymbol{u}_e}{\partial n} \\
&= (\boldsymbol{\nabla}\boldsymbol{u})^T\cdot\hat{\boldsymbol{n}} \\
&= \begin{pmatrix}-y\sin(xy) & -xsin(xy)\\ \exp(x+y) & \exp(x+y)\end{pmatrix}\cdot\hat{\boldsymbol{n}} \qquad (5.10)
\end{aligned}$$

These are written as matrices multiplied by the boundary normal vector to simplify implementation.

Non-Stationary Solution

As non-stationary manufactured solution we apply the stationary manufactured solution multiplied by $\sin(2\pi t)$:

$$\boldsymbol{u}_e = (\cos(xy)\hat{\boldsymbol{\imath}} + \exp(x+y)\hat{\boldsymbol{\jmath}})\sin(2\pi t), \qquad (5.11)$$
$$p_e = (\exp(x)\sin(x+y) - C)\sin(2\pi t). \qquad (5.12)$$

Except for the convection term in the viscous volume force, all generalizations and all Neumann boundary conditions are linear in either $\boldsymbol{u}_e$ or p_e. Converting these from the stationary problem to the non-stationary, reduces to multiplication by a factor $\sin(2\pi t)$. The convection term is quadratic in $\boldsymbol{u}$ and is thus multiplied by $\sin^2(2\pi t)$. In addition, time derivative terms need to be added to the volume forces. These are given by

$$\frac{\partial \boldsymbol{u}_e}{\partial t} = 2\pi\,(\cos(xy)\hat{\boldsymbol{\imath}} + \exp(x+y)\hat{\boldsymbol{\jmath}})\cos(2\pi t). \qquad (5.13)$$

5.2.4 Boundary Conditions

Pressure type boundary conditions, meaning pseudo-traction conditions on viscous parts and Dirichlet pressure conditions on porous parts, are set at $y = \pm 0.5\,\text{cm}$. Similarly, velocity type boundary conditions refer to Dirichlet velocity conditions at viscous boundaries and Neumann conditions for the normal Darcy velocity at porous boundaries; these are set at $x = \pm 0.5\,\text{cm}$.

5.3 Error Norm Measurement

5.3.1 Error Norms

Accuracy is measured by the L^2-norm of the error. Given a numerical approximation, $\boldsymbol{u}$, and the exact solution, $\boldsymbol{u}_\mathrm{e}$, the error norm over a domain, Ω, is defined as

$$E = \sqrt{\langle \boldsymbol{u} - \boldsymbol{u}_\mathrm{e},\, \boldsymbol{u} - \boldsymbol{u}_\mathrm{e} \rangle_\Omega}. \tag{5.14}$$

In the coupled problem, error norms are computed separately over viscous and porous domains.

Implementation

The implemented error norm function is included in listing 5.1. It takes the exact solution, 'ue', the numerical approximation, 'u', a higher-order function space, 'Ve', and a domain specification as arguments. The L^2-norm over the given domain is returned. Note the following:

- The exact solution, 'ue', is contained in an Expression instance. If not stated explicitly, this will be projected onto the same space as 'u' in the numerical integration. A more accurate error norm is obtained by first projecting 'ue' and 'u' onto a higher-order function space. In our verification tests, this is of order 5.
- To minimize round-off errors, an error function is computed by subtracting the degrees of freedom before integrating.

Listing 5.1: Implemented error norm function.

```
def _domain_errornorms(self, ue, u, Ve, domain):
    """Compute errornorm over given domain."""
    ue = project(ue, Ve)
    u = project(u, Ve)
    error = Function(Ve)
    error.vector()[:] = ue.vector().array() - u.vector().array()
    L2_norm = inner(error, error)*dx(self.numbering[domain])

    return sqrt(assemble(L2_norm, mesh=Ve.mesh(),
                         cell_domains=self.cell_domains))
```

5.3.2 Stationary Solutions

For stationary test problems we use the initial condition,

$$\boldsymbol{u}(t_0) = 0.$$

Error norms are sampled when a steady state is reached. We use the convergence criterion

$$\frac{E(t_n) - E(t_{n-1})}{\Delta t E(t_n)} < \varepsilon, \tag{5.15}$$

where $\varepsilon = 1.0 \times 10^{-7}$.

5.3.3 Non-Stationary Solutions

For non-stationary test problems we set the initial velocity equal to the exact solution,

$$\boldsymbol{u}(t_0) = \boldsymbol{u}_e(t_0).$$

Error norms are computed for each time step, and then integrated over each period using the trapezoidal rule. When the integrated error converges, this is taken as measure of the error. We use the convergence criterion

$$\frac{E(T_n) - E(T_{n-1})}{E(T_n)} < \varepsilon, \tag{5.16}$$

where $E(T_n)$ is the integrated error over period number n, and we apply $\varepsilon = 1.0 \times 10^{-2}$. Note that we present the error given after a predefined number of periods. Thus, ε is only an upper limit.

5.3.4 Convergence Rates

In the respective asymptotic convergence regions for h and Δt, the error should vary approximately as

$$E = Ch^r \qquad \text{and} \qquad E = D(\Delta t)^s, \tag{5.17}$$

where C and D are constants and r and s denote convergence rates in h and Δt, respectively. In the verification tests, errors are computed from a series of experiments, varying h and Δt. In the respective asymptotic regions, convergence rates are then given by

$$r = \frac{\log(E_1/E_2)}{\log(h_1/h_2)}, \qquad s = \frac{\log(E_1/E_2)}{\log(\Delta t_1/\Delta t_2)}, \tag{5.18}$$

where E_1 and E_2 are errors given by the corresponding discretization parameters.

5.4 Results

We present results of the numerical experiments. Results for the viscous equations, porous equations and coupled problem are handled separately in sections 5.4.1–5.4.3. Finally, a summary is given in section 5.4.4. This section contains many tables of computed error norms and convergence rates. These are collected at the end of the section. An overview is given in table 5.1.

Problem	Parameters	Solution	Tables	
			Norms	Rates
viscous	unity	stationary	5.2	5.17
		non-stationary	5.3	5.18
	realistic	stationary	5.4	5.19
		non-stationary	5.5	5.20
porous	unity	stationary	5.6	5.21
		non-stationary	5.7	5.22
	realistic	stationary	5.8	5.23
		non-stationary	5.9	5.24

(a) Separate viscous and porous problems

Parameters	Solution	Region	Tables	
			Norms	Rates
unity	stationary	viscous	5.10	5.25
		porous	5.11	
	non-stationary	viscous	5.12	5.26
		porous	5.13	
realistic	stationary	viscous	5.14	5.27
		porous	5.15	
	non-stationary	both	5.16*	5.28*

(b) Coupled problem

Table 5.1: List of error norm and convergence rate tables. Unless stated otherwise, each table includes results for both the coupled scheme and the IPCS.

**Results only given for the coupled scheme.*

5.4.1 Viscous Equations

Problem Parameters = 1, Stationary Solution

Computed error norms and convergence rates for the stationary problem with parameters equal to one are given in tables 5.2 and 5.17, respectively. Performance of the IPCS is close to that of the coupled scheme, yielding errors of equal order of magnitude. Both schemes show second order convergence in both velocity and pressure, in accordance with the given convergence estimates. We observe no dependence on Δt in the final, stationary solution. However, this parameter may affect relaxation time.

Problem Parameters = 1, Non-Stationary Solution

Computed error norms and convergence rates for the non-stationary problem with parameters equal to one are given in tables 5.3 and 5.18, respectively. The error in the temporal discretization dominates, yielding the expected linear convergence. The IPCS and the coupled scheme show similar performance, with errors of equal order of magnitude. Differences decrease with shorter time steps.

Realistic Problem Parameters, Stationary Solution

Computed error norms and convergence rates for the stationary problem with realistic parameters are given in tables 5.4 and 5.19, respectively. Solutions are unstable, oscillating or blowing up, for $h>0.05$. Depending on the time step, some instabilities occur also for higher mesh resolutions. Final, stationary solutions are independent of the time step.

Velocity errors are up to two orders of magnitude larger for the IPCS compared to the coupled scheme, and the latter has a higher convergence rate. Differences in pressure are small. The coupled scheme yields third order convergence in velocity; however, this rate is rapidly decreasing with higher mesh resolutions. Otherwise, second order convergence is observed for velocity and pressure, in accordance with the given estimates.

Compared to the case with all parameters equal to one, errors in velocity are 2–3 orders of magnitude greater. However, with the coupled scheme we also observe an increased convergence rate. Errors in pressure are slightly smaller with realistic parameters, by less than one order of magnitude.

Realistic Problem Parameters, Non-Stationary Solution

Computed error norms and convergence rates for the non-stationary problem with realistic parameters are given in tables 5.5 and 5.20, respectively. Solutions are unstable for $h>0.025$ with the coupled scheme and for $h, \Delta t>0.0125$ with the IPCS.

The error in the temporal discretization dominates. The coupled scheme yields a clear first order convergence in Δt. Corresponding rates for the IPCS are between 1.6 and 3.9, rapidly decreasing with smaller time steps. Errors are up to one order of magnitude larger for the IPCS compared to the coupled scheme. However, differences decrease with smaller time steps.

Compared to the case where all parameters are set equal to one, the coupled scheme yields up to one order of magnitude larger errors in velocity and about three orders of magnitude smaller errors in pressure. Since the IPCS is mostly unstable for discretization parameters used with all parameters equal to one, a similar comparison for the IPCS is difficult. However, solutions indicate a lower accuracy in velocity and a higher accuracy in pressure, as with the coupled scheme.

5.4.2 Porous Equations

Problem Parameters = 1, Stationary Solution

Computed error norms and convergence rates for the stationary problem with parameters equal to one are given in tables 5.6 and 5.21, respectively. The IPCS and the coupled scheme yield equal errors. Convergence rates are 1.5 and 2.0 for velocity and pressure, respectively. Thus, observed velocity convergence is more rapid than the expected first order behavior given by Mini elements. Taylor-Hood elements apply higher order polynomials in the velocity approximation, possibly explaining this difference. There is no apparent dependence on Δt in the final stationary solution.

Problem Parameters = 1, Non-Stationary Solution

Computed error norms and convergence rates for the non-stationary problem with parameters equal to one are given in tables 5.7 and 5.22, respectively. The IPCS and the coupled scheme yield equal errors. The error in the temporal discretization dominates, and we get the expected first order convergence.

Realistic Problem Parameters, Stationary Solution

Computed error norms and convergence rates for the stationary problem with realistic parameters are given in tables 5.8 and 5.23, respectively. The IPCS and the coupled scheme yield equal results. We observe a third order convergence in velocity, increased compared to the case with parameters equal to one. Higher order convergence is also observed for the pressure. However, the latter decreases rapidly with increased mesh resolution, approaching the expected second order behavior. There is no apparent dependence of Δt in the final solution.

Compared to the case with all parameters set equal to one, the velocity converges faster and observed velocity errors are lower by 3–5 orders of magnitude. Errors in pressure are greater by about one order of magnitude for coarser meshes, but this difference evens out with higher mesh resolutions.

Realistic Problem Parameters, Non-Stationary Solution

Computed error norms and convergence rates for the non-stationary problem with realistic parameters are given in tables 5.9 and 5.24, respectively. The IPCS and the coupled scheme yield equal results. Errors in velocity are dominated by the error in the spatial discretization, which yields a third order convergence like in the stationary tests. Errors in pressure are dominated by the error in the spatial discretization for lower mesh resolutions, and by the error in the temporal discretization for higher mesh resolutions; for the highest resolution, $h = 0.0125$, there is a clear first order convergence in Δt.

Computed velocity error norms are 2–7 orders of magnitude smaller than with the parameters set equal to one, in which the error in the temporal discretization dominated. Errors in pressure is up to one order of magnitude larger for low mesh resolution, and up to about two orders of magnitude smaller for higher mesh resolutions.

5.4.3 Coupled Equations

Results for the coupled problem are given in the following. Note that errors are integrated only over half the domain. Thus, comparing solutions with separate viscous and porous domains, errors norms should be multiplied by two. However, since errors depend on the analytical solution errors norms cannot be compared to a high degree of accuracy.

Problem Parameters = 1

Computed error norms for the stationary coupled problem with parameters equal to one are given in tables 5.10 and 5.11 for viscous and porous regions, respectively. Errors for the corresponding non-stationary problem are given in tables 5.12 and 5.13 for viscous and porous regions, respectively. Convergence rates are collected in tables 5.25 and 5.26.

The coupling does not change the size of errors or convergence rates significantly compared to the separate viscous and porous problems. However, some instabilities occur with the coupled scheme for the highest mesh resolutions. We also observe a slight difference between the IPCS and the coupled scheme in the porous region, not present with uncoupled porous equations. In the stationary case this difference is only seen in the pressure.

Realistic Problem Parameters, Stationary Solution

Computed error norms for the stationary coupled problem with realistic parameters are given in tables 5.14 and 5.15 for viscous and porous regions, respectively. Corresponding convergence rates are collected in table 5.27. Like for the pure viscous domain, introducing realistic problem parameters yields instabilities for $h>0.05$. Errors are similar to that of the uncoupled problems. However, we observe a more rapid convergence rate for the viscous velocity, of about fourth order.

The large difference between the IPCS and the coupled scheme in accuracy of the viscous velocity does not seem to affect the porous region to a great extent. However, as for the case with parameters equal to one, we observe a small difference in the porous pressure that is not present in the decoupled problem.

Realistic Problem Parameters, Non-Stationary Solution

In the coupled, non-stationary problem with realistic parameters, the IPCS is unstable for $h\geq 0.00625$ and $\Delta t\geq 0.003124$. Smaller discretization times yield very long computation time. We thus only include solutions for the coupled scheme. Computed error norms and convergence rates are collected in tables 5.16 and 5.28, respectively.

Like in the separate viscous problem, solutions are unstable for $h>0.025$. The coupling does not change the size of errors or convergence rates to a great extent compared to the separate viscous and porous problems.

5.4.4 Summary

Coupling

On the non-stationary problem with realistic parameters, coupling leads to serious instabilities for the IPCS.

Except for instabilities, coupling does not affect solutions to a great extent. Comparing the schemes, we observe small differences in porous solutions that are not present in the uncoupled problem. With the coupled scheme applied to the stationary problem with realistic parameters we also observed a higher convergence rate in viscous velocities.

Convergence

All tests show convergence in either h or Δt. For non-stationary problems the error in the temporal discretization usually dominates, yielding the expected first order convergence. The exception is for the porous pressure given realistic problem parameters; in this case the error in the spatial discretization dominates, yielding the same rate as observed in the stationary tests.

With all problem parameters set equal to one the stationary tests yield the expected second order convergence for viscous velocity and pressure, and for the porous pressure. The observed convergence rate of 1.5 for the porous velocity is increased compared to the expected linear behavior given by the Mini element. This could be explained by the higher order approximation space of Taylor-Hood elements compared to Mini elements.

With realistic problem parameters the stationary tests yield a third order convergence in porous velocities. Furthermore, the coupled scheme yields a third to fourth order convergence in viscous velocities. Other rates are unchanged by the change in parameters.

Transition to Realistic Parameters

In the stationary problem introducing realistic problem parameters increases errors in viscous velocities by 2–3 orders of magnitude and decreases errors in porous velocities by 3–5 orders of magnitude. Other changes are by less than one order of magnitude. Convergence rates for the porous velocity double, increasing from 1.5 to 3.0. For the coupled scheme, we also observe an increased convergence in viscous velocities, from second to third or fourth order.

In the non-stationary problem errors in viscous velocities increase by about one order of magnitude, and errors in viscous pressure decrease by about three orders of magnitude. For the porous velocity the error in the temporal discretization seem to vanish, resulting in 2–7 order of magnitude smaller errors than with all problem parameters set equal to one. For sufficiently high mesh resolutions, errors in porous pressure are not significantly altered by the change in parameters.

With the transition to realistic parameters instabilities occur in the viscous domain. In the stationary problem stable solutions are given for $h \leq 0.05$. In the non-stationary problem we need $h \leq 0.025$ with the coupled scheme and $h, \Delta t \leq 0.0125$ with the IPCS. On the coupled, non-stationary problem the IPCS yields serious instabilities with the transition to realistic parameters.

IPCS Performance

Introducing realistic parameters in the coupled, non-stationary problem serious instabilities occur with the IPCS. We have not been able to find stable solutions for $h \geq 0.00625$ and $\Delta t \geq 0.003124$.

The IPCS and the coupled scheme yield equal results for the decoupled, porous equations. This is not surprising. Porous boundary conditions are made equivalent to that of the coupled scheme, and using $\beta = 1$ no terms are removed in the operator-splitting. With coupling, small differences are observed.

With all parameters set equal to one, IPCS performance on the viscous

domain is close to that of the coupled scheme. With realistic parameters on the stationary problem we observe a large difference in viscous velocity, the IPCS yielding a slower convergence and 2–3 orders of magnitude larger errors compared to the coupled scheme. In the non-stationary case, we observe increased differences in both velocity and pressure of up to one order of magnitude; however, these become smaller with shorter time steps.

$\Delta t \backslash h$	0.200000	0.100000	0.050000	0.025000	0.012500
0.200000	5.32e-04	1.57e-04	4.37e-05	1.15e-05	2.96e-06
0.100000	5.32e-04	1.57e-04	4.37e-05	1.15e-05	2.96e-06
0.050000	5.32e-04	1.57e-04	4.37e-05	1.15e-05	2.96e-06
0.025000	5.32e-04	1.57e-04	4.37e-05	1.15e-05	2.96e-06
0.012500	5.32e-04	1.57e-04	4.37e-05	1.15e-05	2.96e-06

(a) Error in velocity, coupled scheme

$\Delta t \backslash h$	0.200000	0.100000	0.050000	0.025000	0.012500
0.200000	1.11e-03	3.88e-04	1.13e-04	3.02e-05	7.79e-06*
0.100000	1.11e-03	3.88e-04	1.13e-04	3.02e-05	7.80e-06*
0.050000	1.11e-03	3.88e-04	1.13e-04	3.02e-05	7.80e-06*
0.025000	1.11e-03	3.88e-04	1.13e-04	3.02e-05	7.80e-06
0.012500	1.11e-03	3.88e-04	1.13e-04	3.02e-05	7.80e-06

(b) Error in velocity, IPCS

$\Delta t \backslash h$	0.200000	0.100000	0.050000	0.025000	0.012500
0.200000	1.04e-02	2.77e-03	7.12e-04	1.80e-04	4.54e-05
0.100000	1.04e-02	2.77e-03	7.12e-04	1.80e-04	4.54e-05
0.050000	1.04e-02	2.77e-03	7.12e-04	1.80e-04	4.54e-05
0.025000	1.04e-02	2.77e-03	7.12e-04	1.80e-04	4.54e-05
0.012500	1.04e-02	2.77e-03	7.12e-04	1.80e-04	4.54e-05

(c) Error in pressure, coupled scheme

$\Delta t \backslash h$	0.200000	0.100000	0.050000	0.025000	0.012500
0.200000	1.99e-02	5.63e-03	1.50e-03	3.88e-04*	9.85e-05*
0.100000	1.99e-02	5.63e-03	1.50e-03	3.88e-04	9.85e-05*
0.050000	1.99e-02	5.63e-03	1.50e-03	3.88e-04	9.86e-05*
0.025000	1.99e-02	5.63e-03	1.50e-03	3.88e-04	9.86e-05
0.012500	1.99e-02	5.63e-03	1.50e-03	3.88e-04	9.86e-05

(d) Error in pressure, IPCS

Table 5.2: Error norms for stationary test problem on the pure viscous domain with all problem parameters set equal to one.
**Do not meet the strict convergence criterion (fulfill $\varepsilon < 10^{-5}$).*

$\Delta t \backslash h$	0.200000	0.100000	0.050000	0.025000	0.012500
0.200000	1.77e-01	1.77e-01	1.77e-01	1.77e-01	1.77e-01
0.100000	1.00e-01	1.00e-01	1.00e-01	1.00e-01	1.00e-01
0.050000	5.24e-02	5.23e-02	5.23e-02	5.23e-02	5.23e-02
0.025000	2.70e-02	2.68e-02	2.68e-02	2.67e-02	2.67e-02
0.012500	1.38e-02	1.36e-02	1.36e-02	1.35e-02	1.35e-02

(a) Error in velocity, coupled scheme

$\Delta t \backslash h$	0.200000	0.100000	0.050000	0.025000	0.012500
0.200000	2.86e-01	2.83e-01	2.82e-01	2.81e-01	2.81e-01
0.100000	1.21e-01	1.20e-01	1.20e-01	1.20e-01	1.20e-01
0.050000	5.56e-02	5.54e-02	5.52e-02	5.52e-02	5.52e-02
0.025000	2.72e-02	2.69e-02	2.68e-02	2.68e-02	2.68e-02
0.012500	1.40e-02	1.36e-02	1.35e-02	1.34e-02	1.34e-02

(b) Error in velocity, IPCS

$\Delta t \backslash h$	0.200000	0.100000	0.050000	0.025000	0.012500
0.200000	6.64e-01	6.64e-01	6.64e-01	6.65e-01	6.65e-01
0.100000	3.43e-01	3.42e-01	3.42e-01	3.42e-01	3.42e-01
0.050000	1.73e-01	1.72e-01	1.72e-01	1.72e-01	1.72e-01
0.025000	8.77e-02	8.65e-02	8.62e-02	8.61e-02	8.61e-02
0.012500	4.52e-02	4.36e-02	4.32e-02	4.32e-02	4.31e-02

(c) Error in pressure, coupled scheme

$\Delta t \backslash h$	0.200000	0.100000	0.050000	0.025000	0.012500
0.200000	1.82e-01	1.84e-01	1.85e-01	1.85e-01	1.85e-01
0.100000	1.53e-01	1.59e-01	1.60e-01	1.61e-01	1.61e-01
0.050000	1.55e-01	1.55e-01	1.55e-01	1.55e-01	1.55e-01
0.025000	9.62e-02	9.29e-02	9.21e-02	9.19e-02	9.19e-02
0.012500	5.16e-02	4.73e-02	4.63e-02	4.60e-02	4.60e-02

(d) Error in pressure, IPCS

Table 5.3: Error norms for non-stationary test problem on the pure viscous domain with all problem parameters set equal to one.

$\Delta t \backslash h$	0.050000	0.025000	0.012500	0.006250
0.200000	6.93e-02	5.66e-03	4.46e-04	5.92e-05
0.100000	6.93e-02	5.66e-03	4.46e-04	5.92e-05
0.050000	6.93e-02	5.66e-03	4.46e-04	5.92e-05
0.025000	6.93e-02	5.66e-03	4.46e-04	5.92e-05
0.012500	unstable	5.66e-03	4.46e-04	5.92e-05

(a) Error in velocity, coupled scheme

$\Delta t \backslash h$	0.050000	0.025000	0.012500	0.006250
0.200000	unstable	6.13e-02	1.29e-02	3.00e-03
0.100000	unstable	6.13e-02	1.29e-02	3.00e-03
0.050000	1.75e-01	unstable	1.29e-02	3.00e-03
0.025000	1.75e-01	unstable	1.29e-02	3.00e-03
0.012500	unstable	6.13e-02	1.29e-02	3.00e-03

(b) Error in velocity, IPCS

$\Delta t \backslash h$	0.050000	0.025000	0.012500	0.006250
0.200000	3.06e-04	7.51e-05	1.87e-05	4.68e-06
0.100000	3.06e-04	7.51e-05	1.87e-05	4.68e-06
0.050000	3.06e-04	7.51e-05	1.87e-05	4.68e-06
0.025000	3.06e-04	7.51e-05	1.87e-05	4.68e-06
0.012500	unstable	7.51e-05	1.87e-05	4.68e-06

(c) Error in pressure, coupled scheme

$\Delta t \backslash h$	0.050000	0.025000	0.012500	0.006250
0.200000	unstable	8.81e-05	2.14e-05	5.37e-06
0.100000	unstable	8.81e-05	2.14e-05	5.37e-06
0.050000	3.59e-04	unstable	2.14e-05	5.37e-06
0.025000	3.59e-04	unstable	2.14e-05	5.37e-06
0.012500	unstable	8.81e-05	2.14e-05	5.37e-06

(d) Error in pressure, IPCS

Table 5.4: Error norms for stationary test problem with realistic problem parameters on pure viscous domain.

$\Delta t \backslash h$	0.025000	0.012500	0.006250
0.200000	1.50e+00	1.01e+00	1.01e+00
0.100000	5.77e-01	6.25e-01	6.35e-01
0.050000	4.22e-01*	4.02e-01	4.05e-01
0.025000	1.51e-01*	1.73e-01	1.74e-01
0.012500	5.95e-02	6.86e-02	6.92e-02
0.006250	3.96e-02	2.62e-02	2.57e-02
0.003125	2.95e-02	1.36e-02	1.30e-02

(a) Error in velocity, coupled scheme

$\Delta t \backslash h$	0.012500	0.006250
0.0125000	4.29e-01	2.07e+00
0.0062500	1.29e-01	1.38e-01
0.0031250	4.97e-02	4.38e-02
0.0015625	3.19e-02	1.43e-02

(b) Error in velocity, IPCS

$\Delta t \backslash h$	0.025000	0.012500	0.006250
0.200000	4.87e-04	5.14e-04	5.14e-04
0.100000	2.75e-04	2.70e-04	2.70e-04
0.050000	1.39e-04	1.32e-04	1.31e-04
0.025000	7.79e-05	6.25e-05	6.15e-05
0.012500	5.67e-05	3.11e-05	2.89e-05
0.006250	5.09e-05	1.80e-05	1.37e-05
0.003125	4.93e-05	1.37e-05	7.26e-06

(c) Error in pressure, coupled scheme

$\Delta t \backslash h$	0.012500	0.006250
0.0125000	3.94e-04	6.68e-04
0.0062500	9.75e-05	1.14e-04
0.0031250	3.58e-05	3.28e-05
0.0015625	2.36e-05	1.09e-05

(d) Error in pressure, IPCS

Table 5.5: Error norms for non-stationary test problem with realistic parameters on pure viscous domain.
**Not converged after 30 s. A less strict convergence criterion is fulfilled, ($\varepsilon < 2 \times 10^{-2}$).*

$\Delta t \backslash h$	0.200000	0.100000	0.050000	0.025000	0.012500
0.200000	1.07e-01	3.81e-02	1.35e-02	4.76e-03	1.68e-03
0.100000	1.07e-01	3.81e-02	1.35e-02	4.76e-03	1.68e-03
0.050000	1.07e-01	3.81e-02	1.35e-02	4.76e-03	1.68e-03
0.025000	1.07e-01	3.81e-02	1.35e-02	4.76e-03	unstable*
0.012500	1.07e-01	3.81e-02	1.35e-02	4.76e-03	1.68e-03

(a) Error in velocity, coupled scheme

$\Delta t \backslash h$	0.200000	0.100000	0.050000	0.025000	0.012500
0.200000	1.07e-01	3.81e-02	1.35e-02	4.76e-03	1.68e-03
0.100000	1.07e-01	3.81e-02	1.35e-02	4.76e-03	1.68e-03
0.050000	1.07e-01	3.81e-02	1.35e-02	4.76e-03	1.68e-03
0.025000	1.07e-01	3.81e-02	1.35e-02	4.76e-03	1.68e-03
0.012500	1.07e-01	3.81e-02	1.35e-02	4.77e-03	1.68e-03

(b) Error in velocity, IPCS

$\Delta t \backslash h$	0.200000	0.100000	0.050000	0.025000	0.012500
0.200000	8.52e-03	2.04e-03	4.97e-04	1.22e-04	3.02e-05
0.100000	8.52e-03	2.04e-03	4.97e-04	1.22e-04	3.02e-05
0.050000	8.52e-03	2.04e-03	4.97e-04	1.22e-04	3.02e-05
0.025000	8.52e-03	2.04e-03	4.97e-04	1.22e-04	unstable*
0.012500	8.52e-03	2.04e-03	4.97e-04	1.22e-04	3.02e-05

(c) Error in pressure, coupled scheme

$\Delta t \backslash h$	0.200000	0.100000	0.050000	0.025000	0.012500
0.200000	8.52e-03	2.04e-03	4.97e-04	1.22e-04	3.02e-05
0.100000	8.52e-03	2.04e-03	4.96e-04	1.22e-04	3.01e-05
0.050000	8.52e-03	2.04e-03	4.96e-04	1.22e-04	3.01e-05
0.025000	8.52e-03	2.04e-03	4.96e-04	1.22e-04	3.00e-05
0.012500	8.53e-03	2.04e-03	4.96e-04	1.21e-04	2.98e-05

(d) Error in pressure, IPCS

Table 5.6: Error norms for stationary test problem on pure porous domain with all problem parameters set equal to one.
**Small oscillations of equal order of magnitude as the computed error.*

$\Delta t \backslash h$	0.200000	0.100000	0.050000	0.025000	0.012500
0.200000	4.94e-01	4.90e-01	4.89e-01	4.89e-01	4.89e-01
0.100000	2.56e-01	2.55e-01	2.54e-01	2.54e-01	2.54e-01
0.050000	1.33e-01	1.32e-01	1.32e-01	1.32e-01	1.32e-01
0.025000	6.75e-02	6.66e-02	6.64e-02	6.64e-02	6.64e-02
0.012500	3.50e-02	3.36e-02	3.34e-02	3.34e-02	3.34e-02

(a) Error in velocity, coupled scheme

$\Delta t \backslash h$	0.200000	0.100000	0.050000	0.025000	0.012500
0.200000	4.97e-01	4.91e-01	4.90e-01	4.89e-01	4.89e-01
0.100000	2.56e-01	2.55e-01	2.54e-01	2.54e-01	2.54e-01
0.050000	1.33e-01	1.32e-01	1.32e-01	1.32e-01	1.32e-01
0.025000	6.75e-02	6.66e-02	6.64e-02	6.64e-02	6.64e-02
0.012500	3.50e-02	3.36e-02	3.34e-02	3.34e-02	3.34e-02

(b) Error in velocity, IPCS

$\Delta t \backslash h$	0.200000	0.100000	0.050000	0.025000	0.012500
0.200000	3.72e-01	3.74e-01	3.74e-01	3.74e-01	3.74e-01
0.100000	1.94e-01	1.94e-01	1.93e-01	1.93e-01	1.93e-01
0.050000	9.80e-02	9.71e-02	9.68e-02	9.67e-02	9.67e-02
0.025000	5.03e-02	4.88e-02	4.84e-02	4.84e-02	4.83e-02
0.012500	2.66e-02	2.47e-02	2.43e-02	2.42e-02	2.42e-02

(c) Error in pressure, coupled scheme

$\Delta t \backslash h$	0.200000	0.100000	0.050000	0.025000	0.012500
0.200000	3.72e-01	3.74e-01	3.74e-01	3.74e-01	3.74e-01
0.100000	1.95e-01	1.94e-01	1.94e-01	1.93e-01	1.93e-01
0.050000	9.82e-02	9.71e-02	9.68e-02	9.67e-02	9.67e-02
0.025000	5.03e-02	4.88e-02	4.85e-02	4.84e-02	4.83e-02
0.012500	2.66e-02	2.47e-02	2.43e-02	2.42e-02	2.42e-02

(d) Error in pressure, IPCS

Table 5.7: Error norms for non-stationary test problem on pure porous domain with all problem parameters set equal to one.

$\Delta t \backslash h$	0.200000	0.100000	0.050000	0.025000	0.012500
0.200000	2.43e-04	3.05e-05	3.82e-06	4.77e-07	5.97e-08
0.100000	2.43e-04	3.05e-05	3.82e-06	4.77e-07	5.97e-08
0.050000	2.43e-04	3.05e-05	3.82e-06	4.77e-07	5.97e-08
0.025000	2.43e-04	3.05e-05	3.82e-06	4.77e-07	5.97e-08
0.012500	2.43e-04	3.05e-05	3.82e-06	4.77e-07	5.97e-08

(a) Error in velocity, coupled scheme

$\Delta t \backslash h$	0.200000	0.100000	0.050000	0.025000	0.012500
0.200000	2.43e-04	3.05e-05	3.82e-06	4.77e-07	5.97e-08
0.100000	2.43e-04	3.05e-05	3.82e-06	4.77e-07	5.97e-08
0.050000	2.43e-04	3.05e-05	3.82e-06	4.77e-07	5.97e-08
0.025000	2.43e-04	3.05e-05	3.82e-06	4.77e-07	5.97e-08
0.012500	2.43e-04	3.05e-05	3.82e-06	4.77e-07	5.97e-08

(b) Error in velocity, IPCS

$\Delta t \backslash h$	0.200000	0.100000	0.050000	0.025000	0.012500
0.200000	3.84e-01	2.35e-02	1.35e-03	1.09e-04	2.75e-05
0.100000	3.84e-01	2.35e-02	1.35e-03	1.09e-04	2.75e-05
0.050000	3.84e-01	2.35e-02	1.35e-03	1.09e-04	2.75e-05
0.025000	3.84e-01	2.35e-02	1.35e-03	1.09e-04	2.75e-05
0.012500	3.84e-01	2.35e-02	1.35e-03	1.09e-04	2.75e-05

(c) Error in pressure, coupled scheme

$\Delta t \backslash h$	0.200000	0.100000	0.050000	0.025000	0.012500
0.200000	3.84e-01	2.35e-02	1.35e-03	1.09e-04	2.75e-05
0.100000	3.84e-01	2.35e-02	1.35e-03	1.09e-04	2.75e-05
0.050000	3.84e-01	2.35e-02	1.35e-03	1.09e-04	2.75e-05
0.025000	3.84e-01	2.35e-02	1.35e-03	1.09e-04	2.75e-05
0.012500	3.84e-01	2.35e-02	1.35e-03	1.09e-04	2.75e-05

(d) Error in pressure, IPCS

Table 5.8: Error norms for stationary test problem with realistic problem parameters on pure porous domain.

$\Delta t \backslash h$	0.200000	0.100000	0.050000	0.025000	0.012500
0.200000	1.50e-04	1.88e-05	2.35e-06	2.99e-07	5.18e-08
0.100000	1.50e-04	1.88e-05	2.35e-06	2.95e-07	4.13e-08
0.050000	1.54e-04	1.93e-05	2.41e-06	3.01e-07	3.88e-08
0.025000	1.55e-04	1.94e-05	2.42e-06	3.03e-07	3.82e-08
0.012500	1.55e-04	1.94e-05	2.43e-06	3.04e-07	3.81e-08

(a) Velocity error, coupled scheme

$\Delta t \backslash h$	0.200000	0.100000	0.050000	0.025000	0.012500
0.200000	1.50e-04	1.88e-05	2.35e-06	2.99e-07	5.18e-08
0.100000	1.50e-04	1.88e-05	2.35e-06	2.95e-07	4.13e-08
0.050000	1.54e-04	1.93e-05	2.41e-06	3.02e-07	3.88e-08
0.025000	1.55e-04	1.94e-05	2.42e-06	3.03e-07	3.82e-08
0.012500	1.55e-04	1.94e-05	2.43e-06	3.04e-07	3.81e-08

(b) Velocity error, IPCS

$\Delta t \backslash h$	0.200000	0.100000	0.050000	0.025000	0.012500
0.200000	2.35e-01	1.33e-02	1.29e-03	1.85e-03	1.87e-03
0.100000	2.36e-01	1.37e-02	5.16e-04	9.44e-04	9.70e-04
0.050000	2.42e-01	1.44e-02	4.97e-04	4.62e-04	4.87e-04
0.025000	2.44e-01	1.47e-02	6.56e-04	2.25e-04	2.46e-04
0.012500	2.44e-01	1.49e-02	7.55e-04	1.14e-04	1.26e-04

(c) Pressure error, coupled scheme

$\Delta t \backslash h$	0.200000	0.100000	0.050000	0.025000	0.012500
0.200000	2.31e-01	1.28e-02	1.28e-03	1.86e-03	1.88e-03
0.100000	2.36e-01	1.37e-02	4.86e-04	9.44e-04	9.70e-04
0.050000	2.42e-01	1.44e-02	4.91e-04	4.62e-04	4.87e-04
0.025000	2.44e-01	1.47e-02	6.56e-04	2.25e-04	2.46e-04
0.012500	2.44e-01	1.49e-02	7.55e-04	1.15e-04	1.26e-04

(d) Pressure error, IPCS

Table 5.9: Error norms for non-stationary test problem with realistic parameters on porous domain.

$\Delta t \backslash h$	0.100000	0.050000	0.025000	0.012500
0.200000	1.32e-04	3.82e-05	1.04e-05	2.72e-06
0.100000	1.32e-04	3.82e-05	1.04e-05	unstable
0.050000	1.32e-04	3.82e-05	1.04e-05	unstable
0.025000	1.32e-04	3.82e-05	1.04e-05	unstable
0.012500	1.32e-04	3.82e-05	1.04e-05	2.72e-06

(a) Error in velocity, coupled scheme

$\Delta t \backslash h$	0.100000	0.050000	0.025000	0.012500
0.200000	3.10e-04	9.02e-05*	2.44e-05*	6.30e-06*
0.100000	3.10e-04	9.02e-05	2.44e-05*	6.33e-06*
0.050000	3.10e-04	9.02e-05	2.44e-05	6.34e-06*
0.025000	3.10e-04	9.02e-05	2.44e-05	6.30e-06*
0.012500	3.10e-04	9.02e-05	2.44e-05	6.34e-06

(b) Error in velocity, IPCS

$\Delta t \backslash h$	0.100000	0.050000	0.025000	0.012500
0.200000	1.57e-03	4.17e-04	1.08e-04	2.74e-05
0.100000	1.57e-03	4.17e-04	1.08e-04	unstable
0.050000	1.57e-03	4.17e-04	1.08e-04	unstable
0.025000	1.57e-03	4.17e-04	1.08e-04	unstable
0.012500	1.57e-03	4.17e-04	1.08e-04	2.74e-05

(c) Error in pressure, coupled scheme

$\Delta t \backslash h$	0.100000	0.050000	0.025000	0.012500
0.200000	2.31e-03	6.32e-04*	1.65e-04*	4.22e-05*
0.100000	2.31e-03	6.32e-04	1.66e-04*	4.25e-05*
0.050000	2.31e-03	6.32e-04	1.66e-04	4.27e-05*
0.025000	2.31e-03	6.32e-04	1.66e-04	4.55e-05*
0.012500	2.31e-03	6.32e-04	1.66e-04	4.27e-05

(d) Error in pressure, IPCS

Table 5.10: Error norms in viscous domain of stationary, coupled test problem with all problem parameters set equal to one.
**Do not meet the strict convergence criterion (fulfill $\varepsilon < 10^{-5}$).*

$\Delta t \backslash h$	0.100000	0.050000	0.025000	0.012500
0.200000	2.02e-02	7.12e-03	2.51e-03	8.86e-04
0.100000	2.02e-02	7.12e-03	2.51e-03	unstable
0.050000	2.02e-02	7.12e-03	2.51e-03	unstable
0.025000	2.02e-02	7.12e-03	2.51e-03	unstable
0.012500	2.02e-02	7.12e-03	2.51e-03	8.86e-04

(a) Error in velocity, coupled solver

$\Delta t \backslash h$	0.100000	0.050000	0.025000	0.012500
0.200000	2.02e-02	7.12e-03	2.51e-03	8.86e-04
0.100000	2.02e-02	7.12e-03	2.51e-03	8.86e-04
0.050000	2.02e-02	7.12e-03	2.51e-03	8.86e-04
0.025000	2.02e-02	7.12e-03	2.51e-03	8.86e-04
0.012500	2.02e-02	7.12e-03	2.51e-03	8.86e-04

(b) Error in velocity, IPCS

$\Delta t \backslash h$	0.100000	0.050000	0.025000	0.012500
0.200000	1.19e-03	2.86e-04	7.00e-05	1.73e-05
0.100000	1.19e-03	2.86e-04	7.00e-05	unstable
0.050000	1.19e-03	2.86e-04	7.00e-05	unstable
0.025000	1.19e-03	2.86e-04	7.00e-05	unstable
0.012500	1.19e-03	2.86e-04	7.00e-05	1.73e-05

(c) Error in pressure, coupled solver

$\Delta t \backslash h$	0.100000	0.050000	0.025000	0.012500
0.200000	1.21e-03	2.92e-04	7.17e-05*	1.77e-05*
0.100000	1.21e-03	2.92e-04	7.17e-05	1.77e-05*
0.050000	1.21e-03	2.92e-04	7.17e-05	1.77e-05
0.025000	1.21e-03	2.92e-04	7.17e-05	1.77e-05*
0.012500	1.21e-03	2.92e-04	7.17e-05	1.77e-05

(d) Error in pressure, IPCS

Table 5.11: Error norms in porous domain of stationary, coupled test problem with all problem parameters set equal to one.
**Do not meet the strict convergence criterion (fulfill $\varepsilon < 10^{-5}$).*

$\Delta t \backslash h$	0.100000	0.050000	0.025000	0.012500
0.200000	1.29e-01	1.29e-01	1.29e-01	1.29e-01
0.100000	7.22e-02	7.19e-02	7.18e-02	7.17e-02
0.050000	3.72e-02	3.70e-02	3.69e-02	unstable
0.025000	1.90e-02	1.89e-02	1.88e-02	1.88e-02
0.012500	9.64e-03	9.54e-03	9.49e-03	9.47e-03

(a) Error in velocity, coupled scheme

$\Delta t \backslash h$	0.100000	0.050000	0.025000	0.012500
0.200000	2.34e-01	2.35e-01	2.36e-01	2.37e-01
0.100000	9.45e-02	9.40e-02	9.37e-02	9.40e-02
0.050000	3.99e-02	3.95e-02	3.93e-02	3.94e-02
0.025000	1.91e-02	1.88e-02	1.87e-02	1.84e-02
0.012500	9.55e-03	9.36e-03	9.28e-03	9.01e-03

(b) Error in velocity, IPCS

$\Delta t \backslash h$	0.100000	0.050000	0.025000	0.012500
0.200000	3.61e-01	3.65e-01	3.66e-01	3.67e-01
0.100000	1.92e-01	1.95e-01	1.96e-01	1.96e-01
0.050000	9.82e-02	9.95e-02	9.99e-02	unstable
0.025000	4.96e-02	5.04e-02	5.07e-02	5.08e-02
0.012500	2.48e-02	2.53e-02	2.55e-02	2.56e-02

(c) Error in pressure, coupled scheme

$\Delta t \backslash h$	0.100000	0.050000	0.025000	0.012500
0.200000	1.28e-01	1.30e-01	1.30e-01	1.31e-01
0.100000	1.46e-01	1.45e-01	1.45e-01	1.45e-01
0.050000	1.00e-01	1.01e-01	1.02e-01	1.04e-01
0.025000	5.59e-02	5.72e-02	5.79e-02	5.99e-02
0.012500	2.85e-02	2.93e-02	2.95e-02	3.23e-02

(d) Error in pressure, IPCS

Table 5.12: Error norms in viscous domain of non-stationary, coupled test problem with all problem parameters set equal to one.

$\Delta t \backslash h$	0.100000	0.050000	0.025000	0.012500
0.200000	2.59e-01	2.59e-01	2.59e-01	2.59e-01
0.100000	1.36e-01	1.36e-01	1.36e-01	unstable*
0.050000	7.06e-02	7.03e-02	7.03e-02	unstable
0.025000	3.59e-02	3.57e-02	3.56e-02	3.56e-02
0.012500	1.82e-02	1.80e-02	1.79e-02	1.80e-02

(a) Error in velocity, coupled scheme

$\Delta t \backslash h$	0.100000	0.050000	0.025000	0.012500
0.200000	2.83e-01	2.83e-01	2.83e-01	2.83e-01
0.100000	1.49e-01	1.48e-01	1.47e-01	1.47e-01
0.050000	7.18e-02	7.14e-02	7.14e-02	7.15e-02
0.025000	3.58e-02	3.56e-02	3.55e-02	3.56e-02
0.012500	1.81e-02	1.79e-02	1.78e-02	1.79e-02

(b) Error in velocity, IPCS

$\Delta t \backslash h$	0.100000	0.050000	0.025000	0.012500
0.200000	2.55e-01	2.56e-01	2.56e-01	2.56e-01
0.100000	1.32e-01	1.32e-01	1.32e-01	1.31e-01
0.050000	6.74e-02	6.70e-02	6.69e-02	unstable
0.025000	3.41e-02	3.37e-02	3.36e-02	3.35e-02
0.012500	1.73e-02	1.69e-02	1.68e-02	1.68e-02

(c) Error in pressure, coupled scheme

$\Delta t \backslash h$	0.100000	0.050000	0.025000	0.012500
0.200000	3.07e-01	3.07e-01	3.07e-01	3.07e-01
0.100000	1.53e-01	1.51e-01	1.50e-01	1.50e-01
0.050000	6.85e-02	6.77e-02	6.75e-02	6.76e-02
0.025000	3.34e-02	3.29e-02	3.28e-02	3.30e-02
0.012500	1.69e-02	1.64e-02	1.64e-02	1.65e-02

(d) Error in pressure, IPCS

Table 5.13: Error norms in porous domain of non-stationary, coupled test problem with all problem parameters set equal to one.
**Small oscillations at least in first ten periods.*

$\Delta t \backslash h$	0.050000	0.025000	0.012500	0.006250
0.200000	1.35e-01	1.02e-02	4.77e-04	2.16e-05
0.100000	1.35e-01	1.02e-02	4.77e-04	2.16e-05
0.050000	1.35e-01	1.02e-02	4.77e-04	2.16e-05
0.025000	1.35e-01	1.02e-02	4.77e-04	2.16e-05
0.012500	1.35e-01	1.02e-02	4.77e-04	—

(a) Error in velocity, coupled scheme

$\Delta t \backslash h$	0.050000	0.025000	0.012500	0.006250
0.200000	unstable	2.62e-02	5.10e-03	1.26e-03
0.100000	8.77e-02	2.62e-02	5.10e-03	1.26e-03
0.050000	8.77e-02	2.62e-02	5.10e-03	1.26e-03
0.025000	unstable	2.62e-02	—	1.26e-03
0.012500	8.78e-02	2.62e-02	5.10e-03	—

(b) Error in velocity, IPCS

$\Delta t \backslash h$	0.050000	0.025000	0.012500	0.006250
0.200000	2.67e-04	5.97e-05	1.48e-05	3.70e-06
0.100000	2.67e-04	5.97e-05	1.48e-05	3.70e-06
0.050000	2.67e-04	5.97e-05	1.48e-05	3.70e-06
0.025000	2.67e-04	5.97e-05	1.48e-05	3.70e-06
0.012500	2.67e-04	5.97e-05	1.48e-05	—

(c) Error in pressure, coupled scheme

$\Delta t \backslash h$	0.050000	0.025000	0.012500	0.006250
0.200000	unstable	6.78e-05	1.70e-05	4.53e-06
0.100000	2.68e-04	6.78e-05	1.70e-05	4.53e-06
0.050000	2.68e-04	6.78e-05	1.70e-05	4.53e-06
0.025000	unstable	6.78e-05	—	4.53e-06
0.012500	2.68e-04	6.78e-05	1.70e-05	—

(d) Error in pressure, IPCS

Table 5.14: Error norms in viscous domain of stationary, coupled test problem with realistic problem parameters. The IPCS results fulfill less strict convergence criteria. Some results are missing.
emph

$\Delta t \backslash h$	0.050000	0.025000	0.012500	0.006250
0.200000	2.04e-06	2.55e-07	3.19e-08	4.04e-09
0.100000	2.04e-06	2.55e-07	3.19e-08	4.04e-09
0.050000	2.04e-06	2.55e-07	3.19e-08	4.04e-09
0.025000	2.04e-06	2.55e-07	3.19e-08	4.04e-09
0.012500	2.04e-06	2.55e-07	3.19e-08	—

(a) Error in velocity, coupled scheme

$\Delta t \backslash h$	0.050000	0.025000	0.012500	0.006250
0.200000	unstable	2.55e-07	3.19e-08	unstable*
0.100000	2.04e-06	2.55e-07	3.19e-08	unstable*
0.050000	2.04e-06	2.55e-07	3.19e-08	unstable*
0.025000	unstable	2.55e-07	—	unstable*
0.012500	2.04e-06	2.55e-07	3.19e-08	—

(b) Error in velocity, IPCS

$\Delta t \backslash h$	0.050000	0.025000	0.012500	0.006250
0.200000	6.42e-04	5.62e-05	1.27e-05	3.27e-06
0.100000	6.42e-04	5.62e-05	1.27e-05	3.27e-06
0.050000	6.42e-04	5.62e-05	1.27e-05	3.27e-06
0.025000	6.42e-04	5.62e-05	1.27e-05	3.27e-06
0.012500	6.42e-04	5.62e-05	1.27e-05	—

(c) Error in pressure, coupled scheme

$\Delta t \backslash h$	0.050000	0.025000	0.012500	0.006250
0.200000	unstable	5.69e-05	1.37e-05	3.79e-06
0.100000	6.15e-04	5.69e-05	1.37e-05	3.79e-06
0.050000	6.15e-04	5.69e-05	1.37e-05	3.79e-06
0.025000	unstable	5.69e-05	—	3.79e-06
0.012500	6.15e-04	5.69e-05	1.37e-05	—

(d) Error in pressure, IPCS

Table 5.15: Error norms in porous domain of stationary, coupled test problem with realistic problem parameters. The IPCS results fulfill less strict convergence criteria. Some results are missing.
**Small oscillations in second or third digit.*

$\Delta t \backslash h$	0.025000	0.012500	0.006250
0.200000	5.49e-01	5.51e-01	5.52e-01
0.100000	2.57e-01	2.59e-01	2.59e-01
0.050000	1.34e-01	1.31e-01	1.31e-01
0.025000	7.71e-02	7.10e-02	7.06e-02
0.012500	4.64e-02	3.81e-02	3.76e-02

(a) Error in viscous velocity

$\Delta t \backslash h$	0.025000	0.012500	0.006250
0.200000	4.25e-04	4.07e-04	4.07e-04
0.100000	2.12e-04	2.03e-04	2.03e-04
0.050000	1.09e-04	9.80e-05	9.74e-05
0.025000	6.49e-05	4.88e-05	4.77e-05
0.012500	4.80e-05	2.57e-05	2.37e-05

(b) Error in viscous pressure

$\Delta t \backslash h$	0.025000	0.012500	0.006250
0.200000	1.75e-07	4.68e-08	4.82e-08
0.100000	1.61e-07	2.88e-08	2.31e-08
0.050000	1.62e-07	2.22e-08	9.81e-09
0.025000	1.62e-07	2.07e-08	4.97e-09
0.012500	1.62e-07	2.04e-08	3.32e-09

(c) Error in porous velocity

$\Delta t \backslash h$	0.025000	0.012500	0.006250
0.200000	1.71e-03	1.71e-03	1.71e-03
0.100000	8.77e-04	8.86e-04	8.85e-04
0.050000	4.31e-04	4.42e-04	4.41e-04
0.025000	2.12e-04	2.21e-04	2.20e-04
0.012500	1.05e-04	1.11e-04	1.10e-04

(d) Error in porous pressure

Table 5.16: Error norms for coupled test problem with realistic problem parameters, given by the coupled scheme.

(h_1, h_2)	$(0.2, 0.1)$	$(0.10, 0.05)$	$(0.050, 0.025)$	$(0.0250, 0.0125)$
$r_u(h_1, h_2)$	1.757	1.850	1.923	1.962
$r_p(h_1, h_2)$	1.909	1.958	1.981	1.991

(a) Convergence rates, coupled scheme

(h_1, h_2)	$(0.2, 0.1)$	$(0.10, 0.05)$	$(0.050, 0.025)$	$(0.0250, 0.0125)$
$r_u(h_1, h_2)$	1.512	1.783	1.900	1.953
$r_p(h_1, h_2)$	1.825	1.906	1.953	1.977

(b) Convergence rates, IPCS

Table 5.17: Convergence rates for stationary test problem on the pure viscous domain with all problem parameters set equal to one.

$(\Delta t_1, \Delta t_2)$	$(0.2, 0.1)$	$(0.10, 0.05)$	$(0.050, 0.025)$	$(0.0250, 0.0125)$
$r_u(\Delta t_1, \Delta t_2)$	0.815	0.941	0.968	0.981
$r_p(\Delta t_1, \Delta t_2)$	0.957	0.995	0.997	0.997

(a) Convergence rates, coupled scheme

$(\Delta t_1, \Delta t_2)$	$(0.2, 0.1)$	$(0.10, 0.05)$	$(0.050, 0.025)$	$(0.0250, 0.0125)$
$r_u(\Delta t_1, \Delta t_2)$	1.235	1.115	1.043	0.998
$r_p(\Delta t_1, \Delta t_2)$	0.201	0.050	0.757	0.999

(b) Convergence rates, IPCS

Table 5.18: Convergence rates in Δt for non-stationary test problem on the pure viscous domain with all problem parameters set equal to one. These rates apply for $h = 0.0125$.

(h_1, h_2)	$(0.050, 0.025)$	$(0.0250, 0.0125)$	$(0.01250, 0.00625)$
$r_u(h_1, h_2)$	3.615	3.665	2.914
$r_p(h_1, h_2)$	2.025	2.002	2.000

(a) Convergence rates, coupled scheme

(h_1, h_2)	$(0.050, 0.025)$	$(0.0250, 0.0125)$	$(0.01250, 0.00625)$
$r_u(h_1, h_2)$	1.511	2.252	2.103
$r_p(h_1, h_2)$	2.027	2.045	1.991

(b) Convergence rates, IPCS

Table 5.19: Convergence rates for stationary test problem with realistic problem parameters on pure viscous domain.

$(\Delta t_1, \Delta t_2)$	(0.050, 0.025)	(0.0250, 0.0125)	(0.01250, 0.00625)	(0.006500, 0.003125)
$r_u(\Delta t_1, \Delta t_2)$	1.222	1.328	1.427	0.989
$r_p(\Delta t_1, \Delta t_2)$	1.097	1.090	1.072	0.920

(a) Convergence rates, coupled scheme

$(\Delta t_1, \Delta t_2)$	(0.01250, 0.00625)	(0.006500, 0.003125)	(0.003125 0.0015625)
$r_u(\Delta t_1, \Delta t_2)$	3.906	1.657	1.619
$r_p(\Delta t_1, \Delta t_2)$	2.556	1.791	1.595

(b) Convergence rates, IPCS

Table 5.20: Convergence rates in Δt for non-stationary test problem with realistic problem parameters on the pure viscous domain. These rates apply for $h = 0.00625$.

(h_1, h_2)	$(0.2, 0.1)$	$(0.10, 0.05)$	$(0.050, 0.025)$	$(0.0250, 0.0125)$
$r_u(h_1, h_2)$	1.484	1.499	1.501	1.501
$r_p(h_1, h_2)$	2.061	2.041	2.026	2.015

Table 5.21: Convergence rates for stationary test problem on pure porous domain with all problem parameters set equal to one. Rates are equal for the IPCS and the coupled scheme.

$(\Delta t_1, \Delta t_2)$	$(0.2, 0.1)$	$(0.10, 0.05)$	$(0.050, 0.025)$	$(0.0250, 0.0125)$
$r_u(\Delta t_1, \Delta t_2)$	0.945	0.947	0.989	0.991
$r_p(\Delta t_1, \Delta t_2)$	0.953	1.000	1.000	1.000

Table 5.22: Convergence rates in Δt for non-stationary test problem on pure porous domain with all problem parameters set equal to one. These rates apply for $h = 0.0125$. Rates are equal for the IPCS and the coupled scheme.

(h_1, h_2)	$(0.2, 0.1)$	$(0.10, 0.05)$	$(0.050, 0.025)$	$(0.0250, 0.0125)$
$r_u(h_1, h_2)$	2.995	2.999	2.999	2.998
$r_p(h_1, h_2)$	4.030	4.123	3.625	1.992

Table 5.23: Convergence rates for stationary test problem with realistic problem parameters on pure porous domain. Rates are equal for the IPCS and the coupled scheme.

$(\Delta t_1, \Delta t_2)$	$(0.2, 0.1)$	$(0.10, 0.05)$	$(0.050, 0.025)$	$(0.0250, 0.0125)$
$r_u(\Delta t_1, \Delta t_2)$	0.327	0.089	0.022	0.005
$r_p(\Delta t_1, \Delta t_2)$	0.950	0.994	0.987	0.969

(a) Convergence rates in Δt

(h_1, h_2)	$(0.2, 0.1)$	$(0.10, 0.05)$	$(0.050, 0.025)$	$(0.0250, 0.0125)$
$r_u(h_1, h_2)$	2.995	2.999	2.999	2.996
$r_p(h_1, h_2)$	4.040	4.299	2.721	-0.134

(b) Convergence rates in h

Table 5.24: Convergence rates in Δt and h for non-stationary test problem with realistic parameters on pure porous domain. Rates in Δt are computed for $h = 0.0125$. Rates in h are computed for $\Delta t = 0.0125$. Rates are equal for the IPCS and the coupled scheme.

(h_1, h_2)	$(0.10, 0.05)$	$(0.050, 0.025)$	$(0.0250, 0.0125)$
$r_{u,v}(h_1, h_2)$	1.793	1.879	1.932
$r_{p,v}(h_1, h_2)$	1.909	1.950	1.975
$r_{u,p}(h_1, h_2)$	1.505	1.505	1.503
$r_{p,p}(h_1, h_2)$	2.051	2.030	2.016

(a) Convergence rates, coupled scehme

(h_1, h_2)	$(0.10, 0.05)$	$(0.050, 0.025)$	$(0.0250, 0.0125)$
$r_{u,v}(h_1, h_2)$	1.782	1.887	1.93
$r_{p,v}(h_1, h_2)$	1.868	1.927	1.97
$r_{u,p}(h_1, h_2)$	1.505	1.505	1.50
$r_{p,p}(h_1, h_2)$	2.048	2.028	2.01

(b) Convergence rates, IPCS

Table 5.25: Convergence rates for coupled, stationary test problem with all problem parameters set equal to one.

$(\Delta t_1, \Delta t_2)$	$(0.2, 0.1)$	$(0.10, 0.05)$	$(0.050, 0.025)$	$(0.0250, 0.0125)$
$r_{u,v}(\Delta t_1, \Delta t_2)$	0.842	0.960	0.973	0.985
$r_{p,v}(\Delta t_1, \Delta t_2)$	0.904	0.969	0.979	0.990
$r_{u,p}(\Delta t_1, \Delta t_2)$	0.929	0.953	0.980	0.989
$r_{p,p}(\Delta t_1, \Delta t_2)$	0.959	0.976	0.994	0.997

(a) Convergence rates, coupled solver

$(\Delta t_1, \Delta t_2)$	$(0.2, 0.1)$	$(0.10, 0.05)$	$(0.050, 0.025)$	$(0.0250, 0.0125)$
$r_{u,v}(\Delta t_1, \Delta t_2)$	1.334	1.254	1.073	1.010
$r_{p,v}(\Delta t_1, \Delta t_2)$	-0.148	0.504	0.814	0.972
$r_{u,p}(\Delta t_1, \Delta t_2)$	0.943	1.043	1.001	0.995
$r_{p,p}(\Delta t_1, \Delta t_2)$	1.031	1.154	1.042	1.002

(b) Convergence rates, IPCS

Table 5.26: Convergence rates in Δt for coupled, non-stationary test problem with all problem parameters set equal to one. These rates apply for $h = 0.025$.

(h_1, h_2)	$(0.050, 0.025)$	$(0.0250, 0.0125)$	$(0.01250, 0.00625)$
$r_{u,v}(h_1, h_2)$	3.720	4.419	4.466
$r_{p,v}(h_1, h_2)$	2.163	2.011	2.000
$r_{u,p}(h_1, h_2)$	2.999	2.997	2.982
$r_{p,p}(h_1, h_2)$	3.514	2.140	1.962

(a) Convergence rates, coupled scheme

(h_1, h_2)	$(0.050, 0.025)$	$(0.0250, 0.0125)$	$(0.01250, 0.00625)$
$r_{u,v}(h_1, h_2)$	1.743	2.360	2.02
$r_{p,v}(h_1, h_2)$	1.981	1.996	2.00
$r_{u,p}(h_1, h_2)$	2.999	2.997	—
$r_{p,p}(h_1, h_2)$	3.434	2.059	1.85

(b) Convergence rates, IPCS

Table 5.27: Convergence rates for coupled, stationary test problem with realistic problem parameters.

$(\Delta t_1, \Delta t_2)$	$(0.2, 0.1)$	$(0.10, 0.05)$	$(0.050, 0.025)$	$(0.0250, 0.0125)$
$r_{u,v}(\Delta t_1, \Delta t_2)$	1.090	0.983	0.893	0.909
$r_{p,v}(\Delta t_1, \Delta t_2)$	1.004	1.058	1.030	1.007
$r_{u,p}(\Delta t_1, \Delta t_2)$	1.064	1.234	0.980	0.583
$r_{p,p}(\Delta t_1, \Delta t_2)$	0.950	1.006	1.003	0.998

(a) Convergence rates in Δt

(h_1, h_2)	$(0.050, 0.025)$	$(0.0250, 0.0125)$
$r_{u,v}(\Delta t_1, \Delta t_2)$	0.590	0.042
$r_{p,v}(\Delta t_1, \Delta t_2)$	1.456	0.361
$r_{u,p}(\Delta t_1, \Delta t_2)$	2.995	2.867
$r_{p,p}(\Delta t_1, \Delta t_2)$	-0.023	0.040

(b) Convergence rates in h

Table 5.28: Convergence rates for the coupled scheme applied to the non-stationary test problem with realistic problem parameters. Convergence rates in Δt are computed for $h = 0.00625$. Convergence rates in h are computed for $\Delta t = 0.0125$.

Chapter 6

Investigations on Two-Dimensional Spinal Canal Flow Model

In this chapter we present investigations done on the two-dimensional spinal canal flow model. First, we investigate the applicability of the numerical schemes and make a conclusion on which is most appropriate for further investigations on realistic, three-dimensional geometries. Then, we investigate the role of unknown structural parameters, α and c_a, appearing in the model equations. Finally, some results are drawn from the simple, two-dimensional model regarding how normal CSF dynamics is altered by the presence of a spinal cord cavity, representing a syrinx or a patent segment of the central canal.

6.1 Key Value Measurement

Solutions are compared by comparing velocity and pressure amplitudes, sampled at specific points in the SAS, spinal cord tissue and spinal cord cavity. In the following, these are referred to as *key value measurements*. Key values are used to investigate relaxation, dependence on discretization parameters, variation with unknown structural parameters, and to compare the numerical schemes. Sample points for key value measurements are illustrated in Fig. 6.1 and summarized in Tbl. 6.1.

Solutions that are not properly relaxed may exhibit a significant difference between positive and negative amplitudes. In this case, key values are presented with ranges such that

$$A = \frac{A_1 + A_2}{2} \pm \frac{|A_1 - A_2|}{2}, \tag{6.1}$$

where A_1 and A_2 denote positive and negative amplitudes, respectively.

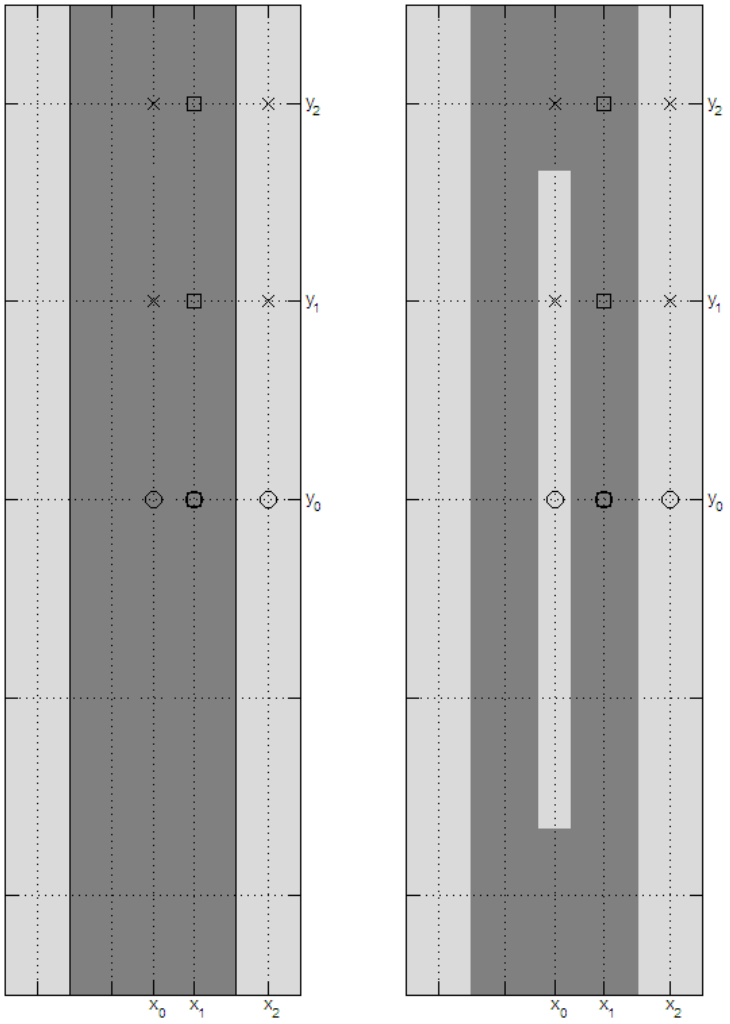

(a) plain domain (b) cavity domain

Figure 6.1: Sample points used in key value measurements. Circles, squares and crosses mark sample points for axial velocity, radial velocity and pressure, respectively. The coordinates are: x_0=0.00, marking the centerline; x_1=0.25 in the plain domain and x=0.30 in the cavity domain, marking the middle between the centerline and the SAS or the cavity boundary and the SAS; x_2=0.70, marking the center of the SAS; y_0=0.00, y_1=1.20 and y_2=2.40, marking points along the y-axis.

Key value	Measure
$u_y(x_0, y_0)$	Axial velocity amplitude in the spinal cord cavity.
$u_y(x_1, y_0)$	Axial velocity amplitude in the spinal cord tissue.
$u_y(x_2, y_0)$	Axial velocity amplitude in the SAS.
$u_x(x_1, y_0)$	Radial velocity amplitude in the spinal cord tissue, at symmetry line.
$u_x(x_1, y_1)$	Radial velocity amplitude in the spinal cord tissue, adjacent to the cavity
$u_x(x_1, y_2)$	Radial velocity amplitude in the spinal cord tissue, above the level of the cavity.
$p(x_0, y_1)$	Pressure amplitude in the spinal cord cavity.
$p(x_0, y_1)$	Pressure amplitude in the SAS, at the level of the spinal cord cavity.
$p(x_0, y_1)$	Pressure amplitude in the tissue above the spinal cord cavity.
$p(x_0, y_1)$	Pressure amplitude in the SAS, above the level of the spinal cord cavity.

Table 6.1: Overview of key values. In this table we refer to the cavity flow domain. Corresponding key values are found in the plain flow domain.

In most samples, differences between positive and negative amplitudes are greater than differences from one period to the next. If there is no well-defined amplitude, that is if there is no clear periodicity or if differences between positive and negative amplitudes are larger than their absolute values, amplitudes are given by the order of magnitude of oscillations.

Radial tissue velocity amplitudes in the plain flow domain and at the symmetry line of the cavity flow domain should from symmetry considerations be equal to zero. These are used to investigate noise in the numerical solutions.

6.2 Comparison of the Numerical Schemes

The numerical schemes are compared by simulations on the two-dimensional spinal canal model. Assuming this to be representative for typical spinal canal flow, we aim to get an indication of the applicability of the different schemes. We first investigate stability. Stable schemes are then compared in efficiency, convergence in the discretization parameters h and Δt, and in accuracy within reasonable ranges of h and Δt.

An overview of the investigated schemes is given in table 6.2. Variants of the IPCS and the Brinkman scheme are given by different choices of the β and γ parameters (Sec. 4.3.3). The schemes are given names for easy referencing.

6.2.1 Preliminaries

Discretization parameters, h and Δt, are varied between 0.1 and 0.01, and 0.1 and 0.001, respectively. Because of limited memory resources, the highest mesh resolution applied with the coupled scheme is given by h=0.025. The total simulation time is six periods, evaluated to yield a sufficient relaxation. Direct linear solvers are applied.

Name	Scheme	β	γ
CPL	Coupled scheme	—	—
IPCSb0g0	IPCS	0	0
IPCSb1g0	IPCS	1	0
IPCSb1g1	IPCS	1	1
IPCSb1g2	IPCS	1	2
BRKMb0	Brinkman scheme	0	—
BRKMb1	Brinkman scheme	1	—

Table 6.2: Schemes included in tests on two-dimensional flow model. Names are given for easy referencing.

6.2.2 Stability

We investigate stability of the different schemes, applied to the two-dimensional flow model. We first consider plain channel flow, that is without an included spinal cord cavity. Only schemes that are stable on this simpler domain is investigated further on the cavity flow problem.

Instabilities are detected by inspection of key value measurements. Solutions that remain stable throughout the first six periods are deemed stable. The degree of instabilities is measured by the time the sampled SAS velocity amplitude exceeds 20 cm/s, 3–4 times greater than its expected value. Tests on the highest resolutions are not performed for schemes that are considered unstable.

Plain Channel Flow

Stability results for the plain channel flow problem are presented in table 6.3. IPCSb1g0, IPCSb1g2 and BRKMb1 yield unstable solutions for all applied $h, \Delta t$-pairs within the ranges $h \geq 0.025$, $\Delta t \geq 0.005$. Furthermore, since instabilities appear earlier with higher resolutions, it is unlikely that solutions will be stable below this range. Note that we are not interested in $h, \Delta t > 0.1$ since this does not give a satisfactory resolution in flow simulations.

The remaining schemes yield stable solutions for $h \leq 0.050$ if the time step is not too short. Higher mesh resolutions allow for shorter time steps. For $h=0.050$, stable solutions are given by $\Delta t=0.100$ with the coupled scheme and $\Delta t \geq 0.050$ with the operator-splitting schemes. For $h=0.025$, $\Delta t \geq 0.005$ is needed for stable solutions with the operator-splitting schemes, while the coupled scheme is stable for the entire Δt-range. With $h=0.010$ we have not considered $\Delta t=0.001$ as this leads to very large computation times; the remaining range of Δt yield stable solutions.

Including a Spinal Cord Cavity

Stability results for the cavity channel flow are presented in table 6.4. All schemes except for IPCSb1g1 remain stable, yielding similar results as for the plain channel flow. Note, however, that IPCSb0g0 is no longer stable for $h=\Delta t=0.050$.

IPCSb1g1 is found to be unstable for all applied $h, \Delta t$-pairs within the ranges $h \geq 0.025$, $\Delta t \geq 0.005$. The results are less conclusive, but we consider it unlikely that stability improves significantly below this range. By inspection of simulation plots, instabilities are found to arise at the cavity ends. The method can be made stable by forcing the velocity to be zero at these interfaces. This is done by imposing Dirichlet conditions on the tentative velocity, combined with $\gamma=0$ in order for the corrected velocity to share this property. Including this fix, IPCSb1g1 has similar stability properties as it did for the plain channel flow (Tbl. 6.4).

$\Delta t \backslash h$	0.100	0.050	0.025
0.100	2.3	OK	OK
0.050	0.8	4.4	OK
0.025	0.9	2.4	OK
0.010	0.8	3.4	OK
0.005	0.3	0.5	OK
0.001	0.2	0.4	OK

(a) CPL

$\Delta t \backslash h$	0.100	0.050	0.025	0.010
0.100	2.7	OK	OK	OK
0.050	1.9	OK	OK	OK
0.025	0.8	5.2	OK	OK
0.010	0.3	0.8	OK	OK
0.005	0.3	0.3	OK	OK
0.001	0.2	0.3	0.9	—

(b) IPCSb0g0

$\Delta t \backslash h$	0.100	0.050	0.025
0.100	1.0	0.8	0.7
0.050	0.7	0.6	0.5
0.025	0.4	0.3	0.3
0.010	0.2	0.2	0.1
0.005	0.1	0.1	0.1

(c) IPCSb1g0

$\Delta t \backslash h$	0.100	0.050	0.025	0.010
0.100	1.9	OK	OK	OK
0.050	1.4	OK	OK	OK
0.025	0.4	3.7	OK	OK
0.010	0.3	0.4	OK	OK
0.005	0.2	0.3	OK	OK
0.001	0.2	0.3	0.9	—

(d) IPCSb1g1

$\Delta t \backslash h$	0.100	0.050	0.025
0.100	1.0	0.8	0.7
0.050	0.7	0.6	0.5
0.025	0.4	0.3	0.3
0.010	0.2	0.2	0.1
0.005	0.1	0.1	0.1

(e) IPCSb1g2

$\Delta t \backslash h$	0.100	0.050	0.025	0.010
0.100	2.2	OK	OK	OK
0.050	2.0	OK	OK	OK
0.025	1.1	2.2	OK	OK
0.010	0.3	0.6	OK	OK
0.005	0.3	0.3	OK	OK
0.001	0.2	0.3	0.9	—

(f) BRKMb0

$\Delta t \backslash h$	0.100	0.050	0.025
0.100	1.0	0.8	0.7
0.050	0.6	0.6	0.5
0.025	0.5	0.3	0.3
0.010	0.2	0.2	0.1
0.005	0.1	0.1	0.1

(g) BRKMb1

Table 6.3: Stability results on plain 2D flow problem. Unstable solutions are given by measured time for the SAS axial speed to exceed 20cm/s. 'OK' denotes solutions that are stable throughout the first six periods. Results for $h = 0.01$, $\Delta t = 0.001$, are not included due to large computation times.

$\Delta t \backslash h$	0.100	0.050	0.025
0.100	2.9	OK	OK
0.050	0.8	3.9	OK
0.025	1.1	5.2	OK
0.010	0.3	1.3	OK
0.005	0.3	0.5	OK
0.001	0.2	0.4	OK

(a) CPL

$\Delta t \backslash h$	0.100	0.050	0.025	0.010
0.100	0.8	OK	OK	OK
0.050	1.1	3.9	OK	OK
0.025	0.4	0.9	OK	OK
0.010	0.3	0.4	OK	OK
0.005	0.4	0.3	OK	OK
0.001	0.2	0.3	0.9	—

(b) IPCSb0g0

$\Delta t \backslash h$	0.100	0.050	0.025
0.100	0.6	1.8	1.2
0.050	0.3	0.6	0.8
0.025	0.2	0.2	0.2
0.010	0.1	0.1	0.1
0.005	0.0	0.0	0.0

(c) IPCSb1g1 (without fix)

$\Delta t \backslash h$	0.100	0.050	0.025	0.010
0.100	2.6	OK	OK	OK
0.050	2.1	OK	OK	OK
0.025	0.5	3.2	OK	OK
0.010	0.3	0.4	OK	OK
0.005	0.2	0.3	OK	OK
0.001	0.2	0.3	0.9	—

(d) IPCSb1g1 (with fix)

$\Delta t \backslash h$	0.100	0.050	0.025	0.010
0.100	0.8	OK	OK	OK
0.050	1.1	OK	OK	OK
0.025	0.4	0.9	OK	OK
0.010	0.3	0.4	OK	OK
0.005	0.4	0.3	OK	OK
0.001	0.2	0.3	0.9	—

(e) BRKMb0

Table 6.4: Stability results on 2D cavity flow problem. Unstable solutions are given by the measured time for the SAS axial speed to exceed 20cm/s. 'OK' denotes solutions that are stable throughout the first six periods. Results for $h = 0.01$, $\Delta t = 0.001$, are not included due to large computation times.

Summary

CPL, IPCSb0g0, IPCSb1g1 (with fix) and BRKMb0 yield stable solutions for $h \leq 0.050$. Temporal resolution is limited by the mesh resolution; higher mesh resolutions allow for shorter time steps.

The β-parameter in the operator-splitting schemes is an important parameter regarding scheme stability. Using $\beta=1$, keeping the extra implicit term in the porous region, leads to instabilities. This can be mended by including an interface term in the pressure correction ($\gamma=1$), but in order for this to work on the cavity domain, we need to add Dirichlet conditions on the cavity inlets. It is uncertain if this scheme will be stable on more complex geometries.

6.2.3 Efficiency

Measured CPU-time per time step for the cavity flow problem is presented in table 6.5. For the most part, time usage is not significantly dependent on Δt. Exceptions occur for the shortest time steps: $\Delta t=0.001$ applied to CPL yields shorter computation times; $\Delta t=0.005$ applied to IPCSb1g1 and IPCSb0g0 yields longer computation times. Comparing efficiency, these odd values are not taken into consideration.

The operator-splitting schemes are more efficient than the coupled scheme. For $h=0.050$ the average CPU-time per time step is 2 s for the operator-splitting schemes and 3 s for the coupled scheme; corresponding results for $h=0.025$ are 12–13 s against 22 s. Comparing the operator-splitting schemes for the highest mesh resolution, the Brinkman scheme is more efficient yielding CPU-times of about 140 compared to about 160 for the IPCS schemes.

Computation times increase rapidly with increased mesh resolution. From $h=0.050$ to $h=0.025$, CPU-time multiplies by 6–7. From $h=0.025$ to $h=0.010$, CPU-time given by the operator-splitting schemes multiplies by 11–13.

6.2.4 Convergence

We investigate the dependence on discretization parameters, h and Δt, to get an indication of what these need to be for a properly converged solution. Solutions are compared by key value measurements, tabulated at the end of this section. An overview is given in table 6.6. In the following, we are only concerned with accuracies of up to three digits.

CPL

The error in the temporal discretization is investigated by comparing solutions for $h=0.025$ with Δt ranging from 0.1 to 0.001. Measured key values are collected in table 6.7. Within the given accuracy, the only observed Δt-dependence is in SAS and cavity velocity amplitudes. The mean SAS

$\Delta t \backslash h$	0.050	0.025
0.100	3.16 ± 0.01	22.41 ± 0.10
0.050	—	22.43 ± 0.19
0.025	—	22.31 ± 0.17
0.010	—	22.27 ± 0.14
0.005	—	22.09 ± 0.16
0.001	—	15.46 ± 1.52
mean	3.2	22.3*

(a) CPL

$\Delta t \backslash h$	0.050	0.025	0.010
0.100	2.09 ± 0.02	12.93 ± 0.07	165.03 ± 2.96
0.050	2.07 ± 0.05	12.85 ± 0.16	164.34 ± 1.76
0.025	—	12.84 ± 0.15	164.75 ± 2.55
0.010	—	12.79 ± 0.12	167.02 ± 6.62
0.005	—	12.82 ± 0.15	181.76 ± 21.54
mean	2.1	12.8	165*

(b) IPCSb1g1

$\Delta t \backslash h$	0.050	0.025	0.010
0.100	2.01 ± 0.02	12.22 ± 0.05	158.03 ± 1.82
0.050	—	12.13 ± 0.18	157.84 ± 1.93
0.025	—	12.10 ± 0.14	158.52 ± 2.74
0.010	—	12.12 ± 0.11	159.40 ± 2.84
0.005	—	12.12 ± 0.16	168.84 ± 6.43
mean	2.0	12.1	158*

(c) IPCSb0g0

$\Delta t \backslash h$	0.050	0.025	0.010
0.100	2.09 ± 0.02	12.48 ± 0.06	137.12 ± 0.40
0.050	2.08 ± 0.05	12.42 ± 0.18	136.78 ± 1.07
0.025	—	12.38 ± 0.14	136.64 ± 0.94
0.010	—	12.36 ± 0.10	136.69 ± 1.14
0.005	—	12.38 ± 0.13	136.80 ± 1.11
mean	2.1	12.4	137

(d) BRKMb0

Table 6.5: Measured CPU-time per time step for the cavity flow problem. Only stable discretizations are included. Ranges are given by two standard deviations.
** Odd value excluded in mean.*

Scheme	h	Δt	Table
CPL	0.025	0.1–0.001	6.7
	0.050, 0.025	0.1	6.8
IPCSb1g1	0.025	0.1–0.005	6.9
	0.010	0.1–0.005	6.10
IPCSb0g0	0.025	0.1–0.005	6.11
/BRKMb0	0.010	0.1–0.005	6.12

Table 6.6: Overview of key value measurements used in convergence investigations on the two-dimensional spinal canal model.

velocity amplitude varies by maximum 2% and is constant for $\Delta t \leq 0.025$. Differences between positive and negative amplitudes decrease with decreasing Δt; however, tests show that this quantity is more dependent on the total simulation time. Cavity velocity amplitudes increase by 3% from Δt=0.100 to Δt=0.001; the difference between the shortest time steps is less than 0.2%.

The only available solutions for investigations of the error in the spatial discretization are given by h=0.050 and h=0.025 with Δt=0.1. Key value measurements for these discretizations are collected in table 6.8. With h=0.050, we observe small oscillations in key values that do not improve with increased simulation times. These are in many cases of equal size as the corresponding difference between the two mesh resolutions, making it difficult to get a good measure of the error in the spatial discretization.

Radial tissue velocities in the plain domain or at the symmetry line of the cavity domain decrease by three orders of magnitude from h=0.050 to h=0.025. From symmetry considerations, these velocities should be zero, and variations in these quantities are considered as noise. As long as these are small compared to other velocities their values are unimportant. However, with h=0.050 these are of the same size as tissue velocities, possibly explaining the observed oscillations.

The measured pressure amplitude inside the spinal cord cavity decreases by three orders of magnitude from h=0.050 to h=0.025. This could also be due to noise, but, since this quantity drives the flow inside the spinal cord cavity, it should not be considered equal to zero. Higher mesh resolutions are needed for a better accuracy; however, if only compared to the much higher pressure amplitudes in the spinal cord tissue and SAS, h=0.025 might be sufficient. Differences in the remaining key values are of equal size as the oscillations observed with h=0.050. Comparing mean values for the two resolutions, we observe differences of 5–6% in 'non-zero' radial tissue velocities and of 2% or less for the remaining samples.

IPCSb1g1

Key value measurements for h=0.025 and h=0.010 with Δt ranging from 0.1 to 0.005 are collected in tables 6.9 and 6.10, respectively. Considering first the plain flow domain, there are few variations with h and Δt. The mean SAS velocity amplitude varies with Δt approximately as for CPL; the maximal difference is of 2%, and for $\Delta t \leq 0.010$ there is no variation within the given accuracy. Comparing SAS velocities for the two mesh resolutions, the mean value differs by 0.2% for the shortest time steps. For h=0.025 we in addition observe a small Δt-dependence on the tissue velocity amplitude, $u_y(x_1, y_0)$, not present for the higher mesh resolution; however, for $\Delta t \leq 0.01$ the two mesh resolutions yield the same result.

Considering the cavity flow domain, we observe a large Δt-dependence on key values within the tissue and in the spinal cord cavity; moreover, these values do not converge for $\Delta t \geq 0.005$. Comparing the shortest time steps, cavity velocity and pressure amplitudes decrease by 40% from h=0.010 to h=0.005; tissue velocities differ by 10–20%, converging more rapidly for the higher mesh resolution. The sampled pressure amplitude inside the tissue differs by 4% between the shortest time steps. SAS velocity and pressure amplitudes remain approximately unaltered compared to the plain flow domain.

IPCSb0g0 and BRKMb0

IPCSb0g0 and BRKMb0 yield identical results. Sampled key values for h=0.025 and h=0.010 with Δt ranging from 0.1 to 0.005 are collected in tables 6.11 and 6.12, respectively. The two mesh resolutions yield approximately equal results. This is except for radial velocities in the plain flow domain, which are up to three orders of magnitude smaller with the higher mesh resolution. However, these are in both cases small compared to all other velocities.

We observe a large Δt-dependence of velocities within the tissue and inside the spinal cord cavity; moreover, these values do not converge for $\Delta t \geq 0.005$. Tissue velocities decrease by up to three orders of magnitude from Δt=0.100 to Δt=0.005, and comparing the shortest time steps differences in amplitudes are of 70–80%. Cavity velocities first increase with a decreased Δt until a maximum is reached at Δt=0.025; then amplitudes decrease rapidly, the difference in amplitude between the shortest time steps of 80%.

Velocities in the SAS are less dependent on Δt. In the plain flow domain we observe the same behavior as with CPL and IPCSb1g1; the maximal difference is of 2%, and for $\Delta t \leq 0.010$ there is no variation within the given accuracy. In the cavity flow domain SAS velocity amplitudes first decrease and then increase, oppositely to the cavity velocity.

Pressure samples in the plain flow domain are independent of Δt. In the

cavity domain SAS pressures show similar behavior as the SAS velocity samples. Measured pressure amplitudes inside the spinal cord cavity decreases rapidly with smaller time steps, differing by 80% comparing the shortest time steps.

Summary

The coupled scheme is the only scheme that yields a satisfactory convergence within the applied ranges of h and Δt. Furthermore, a good accuracy is obtained even for the largest time steps. However, errors in the spatial discretization is difficult to measure from these tests.

Solutions from the operator-splitting schemes are highly dependent on Δt, and do not converge within the given range. For IPCSb0g0 and BRKMb0 this is most prominent for tissue and cavity velocities which decrease rapidly comparing the smallest time steps. IPCSb1g1 converges properly for the plain flow domain; however, with the introduction of a spinal cord cavity, velocities within the cavity decrease rapidly between the smallest time steps.

Amplitude	$u_y(x_0, y_0)$	$u_y(x_1, y_0)$	$u_y(x_2, y_0)$	$u_x(x_1, y_0)$	$u_x(x_1, y_1)$	$u_x(x_1, y_2)$
$\Delta t = 0.100$	6.66×10^{-8}	6.66×10^{-8}	5.44 ± 0.26	$\sim 10^{-11}$	$\sim 10^{-11}$	$\sim 10^{-11}$
$\Delta t = 0.050$	6.66×10^{-8}	6.66×10^{-8}	5.34 ± 0.15	$\sim 10^{-11}$	$\sim 10^{-11}$	$\sim 10^{-11}$
$\Delta t = 0.025$	6.66×10^{-8}	6.66×10^{-8}	5.37 ± 0.10	$\sim 10^{-11}$	$\sim 10^{-11}$	$\sim 10^{-11}$
$\Delta t = 0.010$	6.66×10^{-8}	6.66×10^{-8}	5.37 ± 0.06	$\sim 10^{-11}$	$\sim 10^{-11}$	$\sim 10^{-11}$
$\Delta t = 0.005$	6.66×10^{-8}	6.66×10^{-8}	5.37 ± 0.06	$\sim 10^{-11}$	$\sim 10^{-11}$	$\sim 10^{-11}$
$\Delta t = 0.001$	6.66×10^{-8}	6.66×10^{-8}	5.37 ± 0.05	$\sim 10^{-11}$	$\sim 10^{-11}$	$\sim 10^{-11}$

(a) Velocity measurements, plain flow

Amplitude	$u_y(x_0, y_0)$	$u_y(x_1, y_0)$	$u_y(x_2, y_0)$	$u_x(x_1, y_0)$	$u_x(x_1, y_1)$	$u_x(x_1, y_2)$
$\Delta t = 0.100$	6.10×10^{-6}	3.33×10^{-8}	5.45 ± 0.26	$\sim 10^{-11}$	2.00×10^{-7}	8.31×10^{-8}
$\Delta t = 0.050$	6.15×10^{-6}	3.33×10^{-8}	5.34 ± 0.15	$\sim 10^{-11}$	2.00×10^{-7}	8.31×10^{-8}
$\Delta t = 0.025$	6.23×10^{-6}	3.33×10^{-8}	5.37 ± 0.09	$\sim 10^{-11}$	2.00×10^{-7}	8.31×10^{-8}
$\Delta t = 0.010$	6.25×10^{-6}	3.33×10^{-8}	5.37 ± 0.06	$\sim 10^{-11}$	2.00×10^{-7}	8.30×10^{-8}
$\Delta t = 0.005$	6.26×10^{-6}	3.33×10^{-8}	5.37 ± 0.06	$\sim 10^{-11}$	2.00×10^{-7}	8.31×10^{-8}
$\Delta t = 0.001$	6.27×10^{-6}	3.33×10^{-8}	5.37 ± 0.05	$\sim 10^{-11}$	2.00×10^{-7}	8.31×10^{-8}

(b) Velocity measurements, cavity flow

Amplitude	$p(x_0, y_1)$	$p(x_2, y_1)$	$p(x_0, y_2)$	$p(x_2, y_2)$
$\Delta t = 0.100$	4.00	4.00	8.00	8.00
$\Delta t = 0.050$	4.00	4.00	8.00	8.00
$\Delta t = 0.025$	4.00	4.00	8.00	8.00
$\Delta t = 0.010$	4.00	4.00	8.00	8.00
$\Delta t = 0.005$	4.00	4.00	8.00	8.00
$\Delta t = 0.001$	4.00	4.00	8.00	8.00

(c) Pressure measurements, plain flow

Amplitude	$p(x_0, y_1)$	$p(x_2, y_1)$	$p(x_0, y_2)$	$p(x_2, y_2)$
$\Delta t = 0.100$	$\sim 10^{-4}$	4.00	6.36	8.00
$\Delta t = 0.050$	$\sim 10^{-4}$	4.00	6.36	8.00
$\Delta t = 0.025$	$\sim 10^{-4}$	4.00	6.36	8.00
$\Delta t = 0.010$	$\sim 10^{-4}$	4.00	6.36	8.00
$\Delta t = 0.005$	$\sim 10^{-4}$	4.00	6.36	8.00
$\Delta t = 0.001$	$\sim 10^{-4}$	4.00	6.36	8.00

(d) Pressure measurements, cavity flow

Table 6.7: Key value measurements for CPL with $h = 0.025$, both with and without an included spinal cord cavity. Velocities are given in cm/s, pressure in Pa.

Amplitude	$u_y(x_0, y_0)$	$u_y(x_1, y_0)$	$u_y(x_2, y_0)$	$u_x(x_1, y_0)$	$u_x(x_1, y_1)$	$u_x(x_1, y_2)$
$h = 0.050$	$(6.54 \pm 0.09)\times10^{-8}$	$(6.58 \pm 0.04)\times10^{-8}$	5.39 ± 0.34	$\sim 10^{-8}$	$\sim 10^{-8}$	$\sim 10^{-8}$
$h = 0.020$	6.66×10^{-8}	6.66×10^{-8}	5.44 ± 0.26	$\sim 10^{-11}$	$\sim 10^{-11}$	$\sim 10^{-11}$

(a) Velocity measurements, plain flow

Amplitude	$u_y(x_0, y_0)$	$u_y(x_1, y_0)$	$u_y(x_2, y_0)$	$u_x(x_1, y_0)$	$u_x(x_1, y_1)$	$u_x(x_1, y_2)$
$h = 0.050$	$(6.01 \pm 0.07)\times10^{-6}$	$(3.35 \pm 0.01)\times10^{-8}$	5.39 ± 0.37	$\sim 10^{-8}$	$(1.91 \pm 0.03)\times10^{-7}$	$(7.86 \pm 0.01)\times10^{-8}$
$h = 0.025$	6.10×10^{-6}	3.33×10^{-8}	5.45 ± 0.26	$\sim 10^{-11}$	2.00×10^{-7}	8.31×10^{-8}

(b) Velocity measurements, cavity flow

Amplitude	$p(x_0, y_1)$	$p(x_2, y_1)$	$p(x_0, y_2)$	$p(x_2, y_2)$
$h = 0.050$	4.06 ± 0.14	3.94 ± 0.09	8.00 ± 0.07	7.91 ± 0.09
$h = 0.025$	4.00	4.00	8.00	8.00

(c) Pressure measurements, plain flow

Amplitude	$p(x_0, y_1)$	$p(x_2, y_1)$	$p(x_0, y_2)$	$p(x_2, y_2)$
$h = 0.050$	$\sim 10^{-1}$	3.93 ± 0.09	6.37 ± 0.09	7.91 ± 0.09
$h = 0.025$	$\sim 10^{-4}$	4.00	6.36	8.00

(d) Pressure measurements, cavity flow

Table 6.8: Key value measurements for CPL with $\Delta t = 0.1$, both with and without an included spinal cord cavity. Velocities are given in cm/s, pressure in Pa. Ranges are given by the difference between positive and negative amplitudes in the sixth period. However, this difference is mostly caused by oscillations and is to be considered a measure of the size of these oscillations.

Amplitude	$u_y(x_0, y_0)$	$u_y(x_1, y_0)$	$u_y(x_2, y_0)$	$u_x(x_1, y_0)$	$u_x(x_1, y_1)$	$u_x(x_1, y_2)$
$\Delta t = 0.100$	6.67×10^{-8}	9.69×10^{-8}	5.47 ± 0.27	$\sim 10^{-11}$	$\sim 10^{-11}$	$\sim 10^{-11}$
$\Delta t = 0.050$	6.67×10^{-8}	6.95×10^{-8}	5.35 ± 0.15	$\sim 10^{-11}$	$\sim 10^{-11}$	$\sim 10^{-11}$
$\Delta t = 0.025$	6.67×10^{-8}	6.69×10^{-8}	5.37 ± 0.09	$\sim 10^{-11}$	$\sim 10^{-11}$	$\sim 10^{-11}$
$\Delta t = 0.010$	6.67×10^{-8}	6.67×10^{-8}	5.38 ± 0.06	$\sim 10^{-11}$	$\sim 10^{-11}$	$\sim 10^{-11}$
$\Delta t = 0.005$	6.67×10^{-8}	6.67×10^{-8}	5.38 ± 0.04	$\sim 10^{-11}$	$\sim 10^{-11}$	$\sim 10^{-11}$

(a) Velocity measurements, plain flow

Amplitude	$u_y(x_0, y_0)$	$u_y(x_1, y_0)$	$u_y(x_2, y_0)$	$u_x(x_1, y_0)$	$u_x(x_1, y_1)$	$u_x(x_1, y_2)$
$\Delta t = 0.100$	5.79	$(3.09 \pm 0.01)\times10^{-6}$	5.47 ± 0.27	$\sim 10^{-9}$	$\sim 10^{-8}$	$\sim 10^{-10}$
$\Delta t = 0.050$	5.19	7.43×10^{-7}	5.34 ± 0.15	$\sim 10^{-10}$	$\sim 10^{-10}$	$\sim 10^{-8}$
$\Delta t = 0.025$	4.29	1.77×10^{-7}	5.37 ± 0.09	$\sim 10^{-11}$	$(1.15 \pm 0.78)\times10^{-7}$	$\sim 10^{-8}$
$\Delta t = 0.010$	2.71	5.03×10^{-8}	5.38 ± 0.06	$\sim 10^{-10}$	$(1.57 \pm 0.46)\times10^{-7}$	$\sim 10^{-8}$
$\Delta t = 0.005$	1.62	3.91×10^{-8}	5.38 ± 0.04	$\sim 10^{-8}$	$(1.78 \pm 0.18)\times10^{-7}$	$(7.08 \pm 0.42)\times10^{-8}$

(b) Velocity measurements, cavity flow

Amplitude	$p(x_0, y_1)$	$p(x_2, y_1)$	$p(x_0, y_2)$	$p(x_2, y_2)$
$\Delta t = 0.100$	4.00	4.00	8.00	8.00
$\Delta t = 0.050$	4.00	4.00	8.00	8.00
$\Delta t = 0.025$	4.00	4.00	8.00	8.00
$\Delta t = 0.010$	4.00	4.00	8.00	8.00
$\Delta t = 0.005$	4.00	4.00	8.00	8.00

(c) Pressure measurements, plain flow

Amplitude	$p(x_0, y_1)$	$p(x_2, y_1)$	$p(x_0, y_2)$	$p(x_2, y_2)$
$\Delta t = 0.100$	$\sim 10^{0}$	4.00	7.96 ± 0.25	8.00
$\Delta t = 0.050$	$\sim 10^{0}$	4.00	7.80 ± 0.22	8.00
$\Delta t = 0.025$	2.94 ± 0.65	4.00	7.47 ± 0.17	8.00
$\Delta t = 0.010$	1.86 ± 0.04	4.00	6.96 ± 0.12	8.00
$\Delta t = 0.005$	1.11	4.00 ± 0.01	6.66 ± 0.07	8.00

(d) Pressure measurements, cavity flow

Table 6.9: Key value measurements for IPCSb1g1 with $h = 0.025$, both with and without an included spinal cord cavity. Velocities are given in cm/s, pressure in Pa.

Amplitude	$u_y(x_0, y_0)$	$u_y(x_1, y_0)$	$u_y(x_2, y_0)$	$u_x(x_1, y_0)$	$u_x(x_1, y_1)$	$u_x(x_1, y_2)$
$\Delta t = 0.100$	6.67×10^{-8}	6.67×10^{-8}	5.47 ± 0.27	$\sim 10^{-11}$	$\sim 10^{-11}$	$\sim 10^{-11}$
$\Delta t = 0.050$	6.67×10^{-8}	6.67×10^{-8}	5.35 ± 0.15	$\sim 10^{-11}$	$\sim 10^{-11}$	$\sim 10^{-11}$
$\Delta t = 0.025$	6.67×10^{-8}	6.67×10^{-8}	5.37 ± 0.09	$\sim 10^{-11}$	$\sim 10^{-11}$	$\sim 10^{-11}$
$\Delta t = 0.010$	6.67×10^{-8}	6.67×10^{-8}	5.37 ± 0.06	$\sim 10^{-11}$	$\sim 10^{-11}$	$\sim 10^{-11}$
$\Delta t = 0.005$	6.67×10^{-8}	6.67×10^{-8}	5.37 ± 0.05	$\sim 10^{-11}$	$\sim 10^{-11}$	$\sim 10^{-11}$

(a) Velocity measurements, plain flow

Amplitude	$u_y(x_0, y_0)$	$u_y(x_1, y_0)$	$u_y(x_2, y_0)$	$u_x(x_1, y_0)$	$u_x(x_1, y_1)$	$u_x(x_1, y_2)$
$\Delta t = 0.100$	5.85	6.66×10^{-8}	5.47 ± 0.27	$\sim 10^{-9}$	$\sim 10^{-8}$	$\sim 10^{-10}$
$\Delta t = 0.050$	5.40	6.31×10^{-8}	5.35 ± 0.15	$\sim 10^{-9}$	$\sim 10^{-7}$	$\sim 10^{-8}$
$\Delta t = 0.025$	4.62	5.71×10^{-8}	5.37 ± 0.09	$\sim 10^{-12}$	$(1.14 \pm 0.95)\times10^{-7}$	$\sim 10^{-8}$
$\Delta t = 0.010$	2.75	4.43×10^{-8}	5.37 ± 0.06	$\sim 10^{-10}$	$(1.62 \pm 0.32)\times10^{-7}$	$(5.92 \pm 0.60)\times10^{-8}$
$\Delta t = 0.005$	1.65	3.88×10^{-8}	5.37 ± 0.05	$\sim 10^{-8}$	$(1.78 \pm 0.13)\times10^{-7}$	$(6.82 \pm 0.27)\times10^{-8}$

(b) Velocity measurements, cavity flow

Amplitude	$p(x_0, y_1)$	$p(x_2, y_1)$	$p(x_0, y_2)$	$p(x_2, y_2)$
$\Delta t = 0.100$	4.00	4.00	8.00	8.00
$\Delta t = 0.050$	4.00	4.00	8.00	8.00
$\Delta t = 0.025$	4.00	4.00	8.00	8.00
$\Delta t = 0.010$	4.00	4.00	8.00	8.00
$\Delta t = 0.005$	4.00	4.00	8.00	8.00

(c) Pressure measurements, plain flow

Amplitude	$p(x_0, y_1)$	$p(x_2, y_1)$	$p(x_0, y_2)$	$p(x_2, y_2)$
$\Delta t = 0.100$	$\sim 10^0$	4.00	8.00 ± 0.19	8.00
$\Delta t = 0.050$	$\sim 10^0$	4.00	7.85 ± 0.23	8.00
$\Delta t = 0.025$	3.19 ± 0.96	4.00	7.51 ± 0.22	8.00
$\Delta t = 0.010$	1.84 ± 0.21	4.00	6.96 ± 0.08	8.00
$\Delta t = 0.005$	1.10 ± 0.03	4.00	6.71 ± 0.04	8.00

(d) Pressure measurements, cavity flow

Table 6.10: Key value measurements for IPCSb1g1 with $h = 0.010$, both with and without an included spinal cord cavity. Velocities are given in cm/s, pressure in Pa.

Amplitude	$u_y(x_0, y_0)$	$u_y(x_1, y_0)$	$u_y(x_2, y_0)$	$u_x(x_1, y_0)$	$u_x(x_1, y_1)$	$u_x(x_1, y_2)$
$\Delta t = 0.100$	4.12×10^{-1}	4.12×10^{-1}	5.47 ± 0.27	$\sim 10^{-5}$	$\sim 10^{-5}$	$\sim 10^{-4}$
$\Delta t = 0.050$	1.03×10^{-1}	1.03×10^{-1}	5.35 ± 0.15	$\sim 10^{-5}$	$\sim 10^{-5}$	$\sim 10^{-4}$
$\Delta t = 0.025$	2.61×10^{-2}	2.61×10^{-2}	5.37 ± 0.09	$\sim 10^{-5}$	$\sim 10^{-5}$	$\sim 10^{-5}$
$\Delta t = 0.010$	4.19×10^{-3}	4.19×10^{-3}	5.38 ± 0.06	$\sim 10^{-6}$	$\sim 10^{-6}$	$\sim 10^{-6}$
$\Delta t = 0.005$	1.05×10^{-3}	1.05×10^{-3}	5.38 ± 0.04	$\sim 10^{-6}$	$\sim 10^{-6}$	$\sim 10^{-6}$

(a) Velocity measurements, plain flow

Amplitude	$u_y(x_0, y_0)$	$u_y(x_1, y_0)$	$u_y(x_2, y_0)$	$u_x(x_1, y_0)$	$u_x(x_1, y_1)$	$u_x(x_1, y_2)$
$\Delta t = 0.100$	5.72 ± 0.01	3.91×10^{-1}	5.01 ± 0.38	$\sim 10^{-2}$	$\sim 5 \times 10^{-2}$	$\sim 6 \times 10^{-2}$
$\Delta t = 0.050$	7.55 ± 0.01	$(9.90 \pm 0.02)\times10^{-2}$	4.62 ± 0.15	$\sim 10^{-2}$	$\sim 7 \times 10^{-2}$	$\sim 4 \times 10^{-2}$
$\Delta t = 0.025$	11.21	$(2.28 \pm 0.94)\times10^{-2}$	4.53 ± 0.14	$\sim 10^{-1}$	$\sim 9 \times 10^{-2}$	$\sim 5 \times 10^{-2}$
$\Delta t = 0.010$	2.69	1.49×10^{-3}	5.65 ± 0.06	$\sim 10^{-4}$	1.77×10^{-2}	$(6.87 \pm 0.06)\times10^{-3}$
$\Delta t = 0.005$	0.53	4.87×10^{-4}	5.43 ± 0.04	$\sim 10^{-5}$	3.41×10^{-3}	1.40×10^{-3}

(b) Velocity measurements, cavity flow

Amplitude	$p(x_0, y_1)$	$p(x_2, y_1)$	$p(x_0, y_2)$	$p(x_2, y_2)$
$\Delta t = 0.100$	4.00	4.00	8.00	8.00
$\Delta t = 0.050$	4.00	4.00	8.00	8.00
$\Delta t = 0.025$	4.00	4.00	8.00	8.00
$\Delta t = 0.010$	4.00	4.00	8.00	8.00
$\Delta t = 0.005$	4.00	4.00	8.00	8.00

(c) Pressure measurements, plain flow

Amplitude	$p(x_0, y_1)$	$p(x_2, y_1)$	$p(x_0, y_2)$	$p(x_2, y_2)$
$\Delta t = 0.100$	3.98 ± 0.50	3.86 ± 0.80	7.86 ± 0.50	7.74 ± 0.19
$\Delta t = 0.050$	4.33 ± 0.04	3.61 ± 0.11	7.74 ± 0.22	7.58 ± 0.10
$\Delta t = 0.025$	6.33 ± 0.17	2.86 ± 0.82	8.16 ± 0.21	7.73 ± 0.02
$\Delta t = 0.010$	1.61 ± 0.04	4.15	5.97 ± 0.01	8.09
$\Delta t = 0.005$	0.32 ± 0.01	4.03	6.28	8.02

(d) Pressure measurements, cavity flow

Table 6.11: Key value measurements for IPCSb0g0/BRKMb0 with $h = 0.025$, both with and without an included spinal cord cavity. Velocities are given in cm/s, pressure in Pa.

Amplitude	$u_y(x_0, y_0)$	$u_y(x_1, y_0)$	$u_y(x_2, y_0)$	$u_x(x_1, y_0)$	$u_x(x_1, y_1)$	$u_x(x_1, y_2)$
$\Delta t = 0.100$	4.12×10^{-1}	4.12×10^{-1}	5.47 ± 0.27	$\sim 10^{-6}$	$\sim 10^{-6}$	$\sim 10^{-6}$
$\Delta t = 0.050$	1.03×10^{-1}	1.03×10^{-1}	5.35 ± 0.15	$\sim 10^{-6}$	$\sim 10^{-6}$	$\sim 10^{-6}$
$\Delta t = 0.025$	2.61×10^{-2}	2.61×10^{-2}	5.37 ± 0.09	$\sim 10^{-7}$	$\sim 10^{-7}$	$\sim 10^{-6}$
$\Delta t = 0.010$	4.19×10^{-3}	4.19×10^{-3}	5.37 ± 0.06	$\sim 10^{-8}$	$\sim 10^{-8}$	$\sim 10^{-7}$
$\Delta t = 0.005$	1.05×10^{-3}	1.05×10^{-3}	5.37 ± 0.05	$\sim 10^{-9}$	$\sim 10^{-9}$	$\sim 10^{-8}$

(a) Velocity measurements, plain flow

Amplitude	$u_y(x_0, y_0)$	$u_y(x_1, y_0)$	$u_y(x_2, y_0)$	$u_x(x_1, y_0)$	$u_x(x_1, y_1)$	$u_x(x_1, y_2)$
$\Delta t = 0.100$	5.73 ± 0.01	3.91×10^{-1}	5.01 ± 0.45	$\sim 10^{-2}$	$\sim 5 \times 10^{-2}$	$\sim 6 \times 10^{-2}$
$\Delta t = 0.050$	7.55 ± 0.01	$(9.90 \pm 0.02)\times10^{-2}$	4.60 ± 0.09	$\sim 10^{-2}$	$\sim 7 \times 10^{-2}$	$\sim 4 \times 10^{-2}$
$\Delta t = 0.025$	11.30	$(2.27 \pm 0.96)\times10^{-2}$	4.53 ± 0.06	$\sim 10^{-1}$	$\sim 9 \times 10^{-2}$	$\sim 5 \times 10^{-2}$
$\Delta t = 0.010$	2.66	1.49×10^{-3}	5.64 ± 0.07	$\sim 10^{-4}$	1.75×10^{-2}	$(6.79 \pm 0.06)\times10^{-3}$
$\Delta t = 0.005$	0.53	4.87×10^{-4}	5.43 ± 0.05	$\sim 10^{-5}$	3.40×10^{-3}	1.39×10^{-3}

(b) Velocity measurements, cavity flow

Amplitude	$p(x_0, y_1)$	$p(x_2, y_1)$	$p(x_0, y_2)$	$p(x_2, y_2)$
$\Delta t = 0.100$	4.00	4.00	8.00	8.00
$\Delta t = 0.050$	4.00	4.00	8.00	8.00
$\Delta t = 0.025$	4.00	4.00	8.00	8.00
$\Delta t = 0.010$	4.00	4.00	8.00	8.00
$\Delta t = 0.005$	4.00	4.00	8.00	8.00

(c) Pressure measurements, plain flow

Amplitude	$p(x_0, y_1)$	$p(x_2, y_1)$	$p(x_0, y_2)$	$p(x_2, y_2)$
$\Delta t = 0.100$	3.97 ± 0.49	3.86 ± 0.78	7.86 ± 0.49	7.74 ± 0.18
$\Delta t = 0.050$	4.33 ± 0.06	3.59 ± 0.12	7.73 ± 0.23	7.57 ± 0.09
$\Delta t = 0.025$	6.38 ± 0.16	2.83 ± 0.84	8.16 ± 0.20	7.72 ± 0.01
$\Delta t = 0.010$	1.60 ± 0.04	4.15	5.98 ± 0.01	8.09
$\Delta t = 0.005$	0.32 ± 0.01	4.03	6.29	8.02

(d) Pressure measurements, cavity flow

Table 6.12: Key value measurements for IPCSb0g0/BRKMb0 with $h = 0.010$, both with and without an included spinal cord cavity. Velocities are given in cm/s, pressure in Pa.

6.2.5 Solutions

We compare solutions given by the different schemes. As indicated in the previous section, solutions given by the operator-splitting schemes do not converge within the applied Δt-range. By comparing these to the coupled scheme solutions, we get an indication of how short time steps are needed in order to obtain satisfactory results.

Key values are compared for the highest available resolutions, that is h=0.025 and Δt=0.001 for the coupled scheme, and h=0.010 and Δt=0.005 for the operator splitting schemes. The results are collected in tables 6.13 and 6.14. Key values are marked if differing by more than 10% compared to the higher resolutions.

Plain Channel Flow

Measured key values for the plain channel flow are collected in table 6.13. The schemes yield equal results for the pressure and for SAS velocities. Comparing tissue velocities, CPL and IPCSb1g1 differ only in the last digit. Tissue velocities given by IPCSb0g0 and BRKMb0 have not converged properly in the temporal discretization. Compared to the results given by CPL and IPCSb1g1, these are four orders of magnitude too large, indicating that a very short time step is necessary for a satisfactory result.

Including Spinal Cord Cavity

Measured key values for the cavity flow domain are collected in table 6.14. Presented velocity and pressure amplitudes inside the cavity have not converged for any of the operator-splitting schemes. Compared to the CPL results, these are 4–5 orders of magnitude too large, indicating that a very small time step is needed in order to obtain a sufficient accuracy.

Comparing tissue velocities, results for CPL and IPCSb1g1 are of equal order of magnitude. As observed in the plain flow problem, presented tissue velocities for IPCSb0g0 and BRKMb0 have not converged and are four orders of magnitude larger than for CPL and IPCSb1g1. The schemes yield approximately equal results for the SAS pressure samples. Comparing SAS velocities, CPL and IPCSb1g1 yield equal results. With IPCSb0g0 and BRKMb0 we measure a slightly higher value; however, this exhibits a larger Δt-dependence than the CPL and IPCSb1g1 results.

6.2.6 Summary and Discussion

The results presented in this section indicate that the coupled scheme is the only tested scheme applicable for spinal canal flow problems.

Amplitude	$u_y(x_0, y_0)$	$u_y(x_1, y_0)$	$u_y(x_2, y_0)$
CPL	6.66×10^{-8}	6.66×10^{-8}	5.37 ± 0.05
IPCSb1g1	6.67×10^{-8}	6.67×10^{-8}	5.37 ± 0.05
IPCSb0g0	$1.05\times10^{-3*}$	$1.05\times10^{-3*}$	5.37 ± 0.05
BRKMb0	$1.05\times10^{-3*}$	$1.05\times10^{-3*}$	5.37 ± 0.05

(a) Axial velocity measurements

Amplitude	$p(x_0, y_1)$	$p(x_2, y_1)$	$p(x_0, y_2)$	$p(x_2, y_2)$
CPL	4.00	4.00	8.00	8.00
IPCSb1g1	4.00	4.00	8.00	8.00
IPCSb0g0	4.00	4.00	8.00	8.00
BRKMb0	4.00	4.00	8.00	8.00

(b) Pressure measurements

Table 6.13: Key value measurements for the different schemes on the plain channel flow domain.
**Not properly converged (differ by more than 10% with a change in h or Δt).*

Amplitude	$u_y(x_0, y_0)$	$u_y(x_1, y_0)$	$u_y(x_2, y_0)$
CPL	6.27×10^{-6}	3.33×10^{-8}	5.37 ± 0.05
IPCSb1g1	1.65^*	3.88×10^{-8}	5.37 ± 0.05
IPCSb0g0	0.53^*	$4.87\times10^{-4*}$	5.43 ± 0.05
BRKMb0	0.53^*	$4.87\times10^{-4*}$	5.43 ± 0.05

(a) Axial velocity measurements

Amplitude	$u_x(x_1, y_1)$	$u_x(x_1, y_2)$
CPL	2.00×10^{-7}	8.31×10^{-8}
IPCSb1g1	$(1.78 \pm 0.13)\times10^{-7}$	$(6.82 \pm 0.27)\times10^{-8}$
IPCSb0g0	$3.40\times10^{-3*}$	$1.39\times10^{-3*}$
BRKMb0	$3.40\times10^{-3*}$	$1.39\times10^{-3*}$

(b) Radial velocity measurements

Amplitude	$p(x_0, y_1)$	$p(x_2, y_1)$	$p(x_0, y_2)$	$p(x_2, y_2)$
CPL	$\sim 10^{-4*}$	4.00	6.36	8.00
IPCSb1g1	$(1.10 \pm 0.03)^*$	4.00	6.71 ± 0.04	8.00
IPCSb0g0	$(0.32 \pm 0.01)^*$	4.03	6.29	8.02
BRKMb0	$(0.32 \pm 0.01)^*$	4.03	6.29	8.02

(c) Pressure measurements

Table 6.14: Key value measurements for the different schemes on the cavity flow domain.
**Not properly converged (differ by more than 10% with a change in h or Δt).*

Applicability of the Coupled Scheme

Solutions given by the coupled scheme show a sufficient convergence within the applied ranges of h and Δt. There is little dependence on Δt, indicating that a large time step can be applied. Dependence on h has not been measured properly due to noise for the higher mesh resolution. However, differences in mean values between the two resolutions are small. Furthermore, many key values are equal to those given by IPCSb1g1 with a higher mesh resolution, indicating that the error in the spatial discretization is small.

Comparing key values of h=0.050 and h=0.025, the measured pressure amplitude inside the spinal cord cavity varies by several orders of magnitude. However, in the latter case this is very small. Assuming that pressure values inside the cavity are only compared to the much larger values in the tissue and SAS, it may be sufficient to apply h=0.025.

Applicability of the Operator-Splitting Schemes

The β-parameter for the IPCS and the Brinkman scheme is a switch used to either include or omit an implicit term in the porous region, which is proportional to $\frac{\mu \Delta t}{K}$. Since K is very small for spinal cord tissue ($10^{-15}\,\mathrm{m}^2$), omitting this term could lead to large errors unless Δt is very small. However, as we have seen, including this term yields instabilities. These can be partly mended by adding an interface term in the pressure correction (γ=1). However, in order to obtain stable solutions for the cavity flow domain, we need to add extra Dirichlet conditions, forcing the velocity to be zero at the cavity ends. It is uncertain if stable solutions can be obtained in more complex flow domains.

Flow simulations on the two-dimensional spinal canal model show that setting β=0, i.e. omitting the implicit term, velocities inside the spinal cord tissue are several orders of magnitude too large if the time step is not very small. With β=1, solutions on the simple channel flow domain agree well with those given by the coupled scheme. However, including a spinal cord cavity, observed cavity velocities are several orders of magnitude too large. Furthermore, mass conservation is seemingly not fulfilled; the microscopic velocities measured in the tissue ($\sim 10^{-8}$) should not allow for the observed magnitude of flow inside the cavity ($\sim 10^{0}$).

Our results indicate that a very short time step is needed in order to obtain a sufficient accuracy with the operator-splitting schemes. However, because of instabilities the temporal resolution is limited by h, such that higher mesh resolutions are needed with shorter time steps. Thus, in addition to increasing the total number of time steps, a small time step demands a high mesh resolution, making each step expensive to compute.

In conclusion, the operator schemes are not applicable, yielding too large velocities in the spinal cord tissue and/or inside the spinal cord cavity. These

velocities decrease rapidly with shorter time steps; however, a sufficiently small time step would yield too long computation times. The IPCS with β=γ=1 may be applicable on flow domains without any cavities. However, it is uncertain if stable solutions can be obtained in more complex geometries; furthermore, our results indicate that conservation of mass may not be fulfilled at interfaces between viscous and porous domains.

The Brinkman Scheme Compared to the IPCS

Comparing the Brinkman scheme and the IPCS with β=γ=0, these yield almost identical results. It is probable that an interface term could be added to the Brinkman scheme in order to imitate IPCSb1g1. However, this has not been investigated. Compared to the IPCS, the Brinkman scheme is much easier to implement, and it shows some advantages regarding efficiency for higher mesh resolutions.

6.3 The Role of Unknown Structural Parameters

Structural parameters, α and c_a, are unknown quantities for spinal cord tissue. Investigations presented here indicate that these parameters are unimportant when studying spinal canal flow. Furthermore, removal of the BJS interface term from the variational formulation is justified.

6.3.1 Preliminaries

We apply the coupled scheme with discretization parameters, $h = 0.025$ and $\Delta t = 0.001$, and a direct linear solver. Solutions are evaluated at the eighth simulation period, compared by key value measurements.

6.3.2 Structural Parameter, α

The α-parameter origins from the BJS interface condition and appears in the variational formulation as an interface term between viscous and porous regions. We investigate the effect of removing this term altogether, applying α=0. As α occurs together with the inverse of the permeability, which is of the order $10^{-15}\,\mathrm{m}^2$, an increase in α is assumed not to have an effect.

With the change from α=1 to α=0, key value measurements change by less than 10^{-4}%. It is thus reasonable to assume that the BJS interface term can be omitted. This is a great advantage for applications on complex geometries since it becomes unnecessary to compute tangent vectors at the interfaces.

6.3.3 Structural Parameter, c_a

The c_a-parameter occurs in front of the inertial term in the non-stationary extension of Darcy's law. We investigate the importance of this parameter, as well as the need to include the non-stationary term altogether.

Comparing key values for $c_a = 0$, equivalent to omitting the inertial term, differences in key values are less than $10^{-4}\%$. This is also the case for tests with c_a-values up to $10^3/\phi$, indicating that the inertial extension is not needed.

6.4 Flow Simulations: The Effect of Spinal Cord Cavities on Normal CSF Dynamics

We present results given by the two-dimensional spinal canal model. This is a highly simplified model, simulating normal spinal canal flow. However, the results indicate how pressure and velocity distributions are affected by the presence of a spinal cord cavity, representing a syrinx or a patent segment of the central canal.

6.4.1 Preliminaries

We apply the coupled scheme with discretization parameters, h=0.025 and Δt=0.001. Solutions are evaluated at the eighth simulation period. The accuracy depends on the variation with the discretization parameters, and if the solution is properly relaxed. This is evaluated by comparison of key value measurements.

6.4.2 Flow Simulations

Still frames from the two-dimensional spinal canal flow simulations, both with and without a spinal cord cavity, are included in Fig. 6.2. The velocity peaks 1/4 period after the maximal pressure difference over the channel inlets. With the given scale, only flow in the SAS is apparent; furthermore, there is no apparent difference between the plain flow domain and the cavity flow domain. Pressure distributions are greatly affected by the presence of a spinal cord cavity. With a homogeneous cord there are no radial gradients and pressure varies linearly along the length of the channel. Introducing a cavity, SAS pressure distributions are unaffected (Figs. 6.3a–b); however, an approximately constant pressure inside the cavity affects pressure distributions within the cord (Figs. 6.3c–d). In particular, constant radial pressure gradients are introduced in the tissue separating the cavity and the SAS (Figs. 6.3e–f). Gradients are of opposite signs at each end of the cavity, changing direction twice during each cycle. Pressure differences, and thus

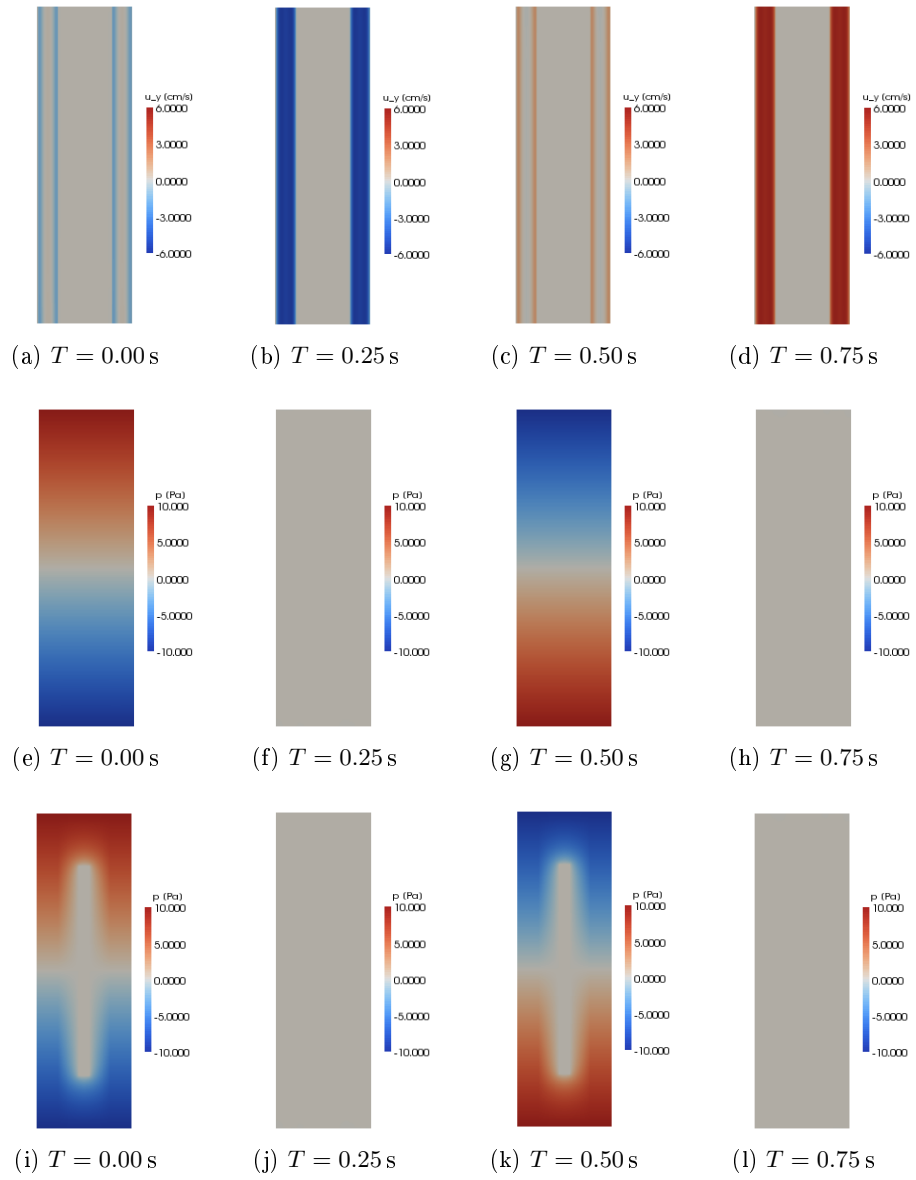

(a) $T = 0.00\,\mathrm{s}$ (b) $T = 0.25\,\mathrm{s}$ (c) $T = 0.50\,\mathrm{s}$ (d) $T = 0.75\,\mathrm{s}$

(e) $T = 0.00\,\mathrm{s}$ (f) $T = 0.25\,\mathrm{s}$ (g) $T = 0.50\,\mathrm{s}$ (h) $T = 0.75\,\mathrm{s}$

(i) $T = 0.00\,\mathrm{s}$ (j) $T = 0.25\,\mathrm{s}$ (k) $T = 0.50\,\mathrm{s}$ (l) $T = 0.75\,\mathrm{s}$

Figure 6.2: Still frames from 2D spinal canal flow simulations, corresponding to maximal amplitudes in velocity and in pressure difference over the channel throughout one period. At this scale axial velocity fields (a–d) are equal whether a cavity is present or not. The pressure field is modified by the presence of a spinal cord cavity. Simulations with no cavity (e–h) show an even pressure across the channel. Including a cavity (i–l), radial pressure gradients are introduced.

Amplitude	Plain Flow	Cavity Flow
$u_y(x_0, y_0)$	7×10^{-8}	6×10^{-6}
$u_y(x_1, y_0)$	7×10^{-8}	3×10^{-8}
$u_y(x_2, y_0)$	5	5
$u_x(x_1, y_0)$	0	0
$u_x(x_1, y_1)$	0	2×10^{-7}
$u_x(x_1, y_2)$	0	8×10^{-8}

Table 6.15: Measured axial and radial velocity amplitudes in key points of 2D spinal canal flow domains. These are given in cm/s. Amplitudes of the order 10^{-11}cm/s are set equal to zero.

also forces on the cord, are largest near the cavity ends. Furthermore, a longer cavity should yield larger gradients.

Velocities inside the cavity and in the spinal cord tissue are small and do not show in Fig. 6.2. To assess these quantities, we compare key value measurements of velocities within the cord (Tbl. 6.15). These show preferential flow inside the cavity compared to the spinal cord tissue and radial flow between the cavity and SAS. Radial velocity distributions are further illustrated in Fig. 6.4. Flow into the cord in areas of high SAS pressures is balanced by a corresponding outflow in areas of low SAS pressures. Radial velocities are greatest near the ends of the cavity, in agreement with the observed pressure distributions.

The results are as expected from simple theoretical considerations. The observed flow field with the homogeneous cord follows from symmetry. Introducing a cavity, the symmetry is broken. Because of the low tissue permeability, fluid inside the cavity must remain approximately stationary; for a free, viscous fluid, this yields an approximately constant pressure inside the cavity, leading to the observed pressure distributions.

6.4.3 Evaluation of Accuracy

Relaxation

The slowest relaxation is observed for SAS velocities, which differ in amplitude for upwards and downwards flow. In the eighth period there is a 0.7% difference between positive and negative SAS amplitudes. Comparing the seventh and eighth period, all key value measurements change by less than 0.1%.

Dependence on h and Δt

We expect a poor accuracy for pressure inside the cavity (cf. Sec. 6.2.4). However, we are only concerned with comparing this value to the much

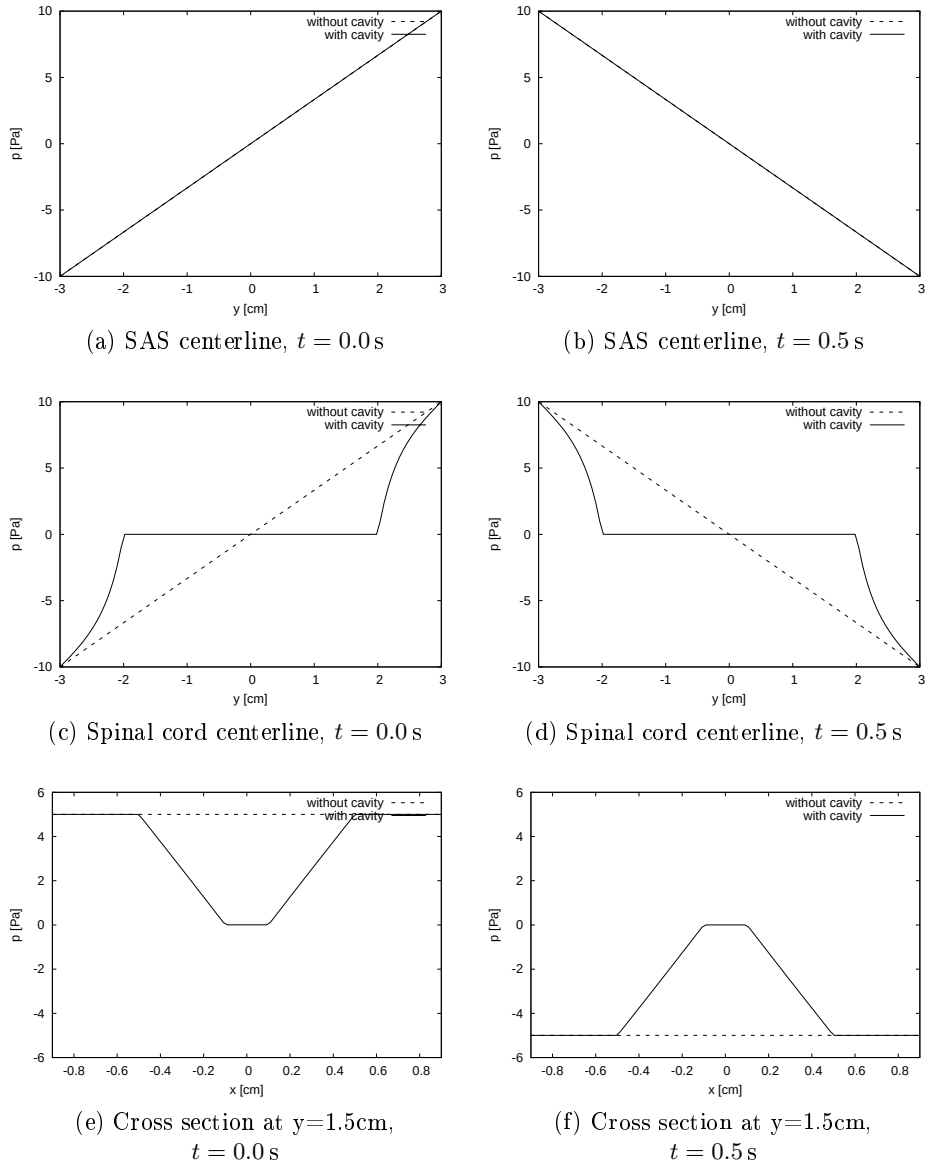

(a) SAS centerline, $t = 0.0\,\mathrm{s}$

(b) SAS centerline, $t = 0.5\,\mathrm{s}$

(c) Spinal cord centerline, $t = 0.0\,\mathrm{s}$

(d) Spinal cord centerline, $t = 0.5\,\mathrm{s}$

(e) Cross section at y=1.5cm, $t = 0.0\,\mathrm{s}$

(f) Cross section at y=1.5cm, $t = 0.5\,\mathrm{s}$

Figure 6.3: Pressure line plots at times of maximal pressure difference between channel inlets. Plots along the centerlines of the SAS (a–b) and spinal cord (c–d) show a modification of pressure distributions within the cord. This is further illustrated by a radial line plot at the centerline between the cavity center and the cavity end (e–f), showing constant pressure gradients between the SAS and the cavity.

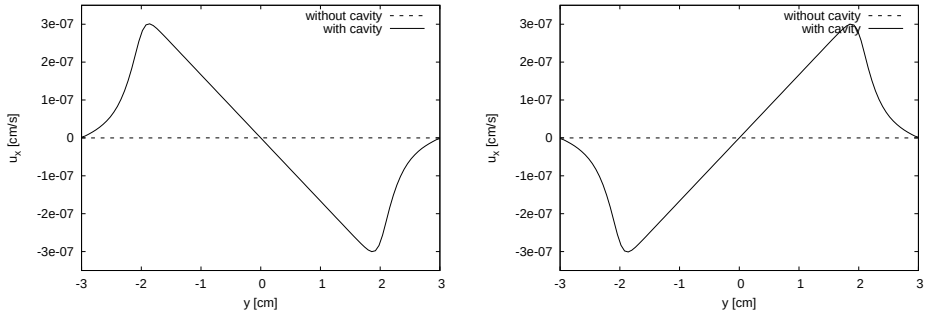

(a) $t = 0.0\,\mathrm{s}$ (b) $t = 0.5\,\mathrm{s}$

Figure 6.4: Radial velocities in the tissue between the cord centerline and the SAS (x=x_1). Positive values denote flow towards the SAS; negative values denote inwards flow.

larger pressure amplitudes in the tissue and SAS. In this respect, the cavity pressure can be considered equal to zero.

Increasing the time step to $\Delta t = 0.005$, key values change by less than 0.1%. We have less control of the h-dependence. However, from the discussions in sections 6.2.4 and 6.2.6, we expect this to be small, and at least not affecting the qualitative results.

Chapter 7

Discussion and Conclusions

Our study has implications on the appropriate form of the model equations and the applicability of the proposed numerical schemes. Furthermore, investigations on a simple, two-dimensional model indicate how normal spinal canal flow dynamics are affected by the presence of a spinal cord cavity, representing a patent segment of the central canal or a cyst.

Model Equations and Numerical Schemes

In this study, a non-stationary extension of Darcy's law was considered, motivated by the possibly large errors occurring with quasi-stationary descriptions of periodic flows. However, flow experiments indicate that the stationary form is sufficient.

We consider the coupled scheme appropriate for porous and viscous modeling in the spinal canal. Furthermore, flow experiments indicate that the Beavers-Joseph-Saffman interface term can be removed from the variational formulation. This is a great advantage for applications on complex geometries since it makes the computation of interface tangent vectors unnecessary.

The investigated operator-splitting schemes are not applicable. In initial numerical experiments, the IPCS showed similar performance as the coupled scheme. However, in flow experiments the operator-splitting schemes yielded several orders of magnitude too large cavity and tissue velocities within reasonable ranges of the time discretization parameter.

Altered Flow Dynamics with the Presence of a Spinal Cord Cavity

The presence of a spinal cord cavity alters pressure distributions within the cord. In particular, radial pressure gradients are introduced in the tissue between the cavity and the SAS. Since pressure gradients are related to stress, this implies a strain on the spinal cord. Thus, the result may be of impor-

tance for theories that propose strain as the primary cause of syringomyelia.

The applied model is a great simplification of the actual problem; it may not reflect reality. We model the spinal cord as a rigid structure. With a deformable cord, radial pressure gradients would not only drive flow, but act to compress and distend the cord. Furthermore, it is likely that an inhomogeneous or anisotropic permeability yields more complex pressure distributions within the cord tissue.

Future Research

The aim of this thesis work was to apply the viscous and porous model to patient-specific or idealized geometries of the spinal canal. Finding the coupled scheme appropriate, the natural next step is to use this scheme to solve problems on the more realistic geometries. However, it is first necessary to develop an iterative linear solver.

Bibliography

Beavers, G. S. and D. D. Joseph (1967). Boundary conditions at a natural permeable wall. *Jour. of Fluid Mechanics 30*, 197–207.

Bertram, C. D. (2010). Evaluation by fluid/structure-interaction spinal-cord simulation on the effects of subarachnoid-space stenosis on an adjacent syrinx. *Journal of Biomechanical Engineering 132*.

Bertram, C. D., A. R. Brodbelt, and M. A. Stoodley (2005). The origins of syringomyelia: Numerical models of fluid/structure interactions in the spinal cord. *J Biomech Eng 127*, 1099–1109.

Bilston, L. E., M. A. Stoodley, and D. F. Fletcher (2009). The influence of the relative timing of arterial and subarachnoid space pulse waves on spinal perivascular cerebrospinal fluid flow as a possible factor in syrinx development. *J Neurosurg*.

Bloomfield, I. G., I. H. Johnston, and L. E. Bilston (1998). Effects of proteins, blood cells and glucose on the viscosity of cerebrospinal fluid. *Pediatr Nerosurg 28*, 246–251.

Carpenter, P. W., K. Berkouk, and A. D. Lucey (2003). Pressure wave propagation in fluid-filled co-axial tubes. part 2. mechanisms for the pathogenesis of syringomyelia. *J Biomech Eng 125*, 857–63.

Cheng, S., E. C. Clarke, and L. E. Bilston (2008). Rheological properties of the tissues of the central nervous system: A review. *Medical Engineering & Physics 30*, 1318–1337.

Cousins, J. and V. Haughton (2009). Motion of the cerebellar tonsils in the foramen magnum during the cardiac cycle. *Am J Neuroradiol 30*, 1587–88.

Elman, H., D. Silvester, and A. Wathen (2005). *Finite Elements and Fast Iterative Solvers: with applications in incompressible fluid dynamics*. Numerical mathematics and scientific computation. Oxford University Press.

Gray, H. (2000). *Gray's Anatomy of the Human Body* (twentieth ed.). Bartleby.com.

Greitz, D. (2006). Unraveling the riddle of syringomyelia. *Nerosurg Rev 29*, 251–264.

Gresho, P. M. and R. L. Sani (1998). *Incompressible Flow and the Finite Element Method, Volume 2: Isothermal Laminar Flow.* John Wiley & Sons, Ltd.

Gupta, S., M. Soellinger, P. Boesinger, D. Poulikakos, and V. Kurtcuoglu (2009). Three-dimensional computational modeling of subject-specific cerebrospinal fluid flow in the subarachnoid space. *Journal of Biomechanical Engineering 131.*

Haughton, V., F. R. Korosec, J. E. Medow, M. T. Dolar, and B. J. Iskandar (2003). Peak systolic and diastolic CSF velocity in the foramen magnum in adult patients with Chiari I malformations and in normal control participants. *Am. J. Neuroradiol. 24*, 169–176.

Heiss, J. D., N. Patronas, H. L. DeVroom, T. Shawker, R. Ennis, W. Kammerer, et al. (1999). Elucidating the pathophysiology of syringomyelia. *J Neurosurg 91*, 553–562.

Hentschel, S., K.-A. Mardal, A. E. Løvgren, S. Linge, and V. Haughton (2010). Characterization of cyclic CSF flow in the foramen magnum and upper cervical spinal canal with MR flow imaging and computational fluid dynamics. *Am. J. Neuroradiol. 31*, 997–1002.

Juntunen, M. and R. Stenberg (2009). Analysis of finite element methods for the Brinkman problem. *Calcolo 47*(3), 129–147.

Kaczmarek, M., R. P. Subramaniam, and S. R. Neff (1997). The hydromechanics of hydrocephalus: Steady-state solutions for cylindrical geometry. *Bulletin of Mathematical Biology 59*(2), 295–323.

Karper, T., K.-A. Mardal, and R. Winther (2008). Unified finite element discretizations of coupled Darcy-Stokes flow. *Numerical methods for partial differential equations 25*(2), 311–326.

Karper, T. K. (2006). Mixed finite element methods for coupled darcy-stokes flow. Master's thesis, University of Oslo.

Langtangen, H. P., K.-A. Mardal, and R. Winther (2002). Numerical methods for incompressible viscous flow. *Advances in Water Resources.*

Larson, M. G. and F. Bengzon (2010). The finite element method: Theory, implementation, and practice. lecture notes.

Levine, D. N. (2004). The pathogenesis of syringomyelia associated with lesions at the foramen magnum: a critical review of existing theories and proposal of a new hypothesis. *J Neurol Sci 220*, 3–21.

Linge, S. O., V. Haughton, A. E. Løvgren, K. A. Mardal, A. Helgeland, and H. P. Langtangen (2011). Effect of tonsillar herniation on cyclic CSF flow studied with computational flow analysis. *Am J Neuroradiol*.

Linge, S. O., V. Haughton, A. E. Løvgren, K. A. Mardal, and H. P. Langtangen (2010). CSF flow dynamics at the craniovertebral junction studied with an idealized model of the subarachnoid space and computational flow analysis. *Am. J. Neuroradiol. 31*, 185–192.

Loth, F., M. A. Yardimci, and N. Alperin (2001). Hydrodynamic modeling of cerebrospinal fluid motion within the spinal cavity. *ASME J. Biomech. Engrg. 123*, 71–73.

Mardal, K.-A. and H. P. Langtangen (2003). Mixed finite elements. In H. P. Langtangen and A. Tveito (Eds.), *Advanced Topics in Computational Partial Differential Equations*. Springer.

Mardal, K.-A., X.-C. Tai, and R. Winther (2002). A robust finite element method for darcy-stokes flow. *SIAM J. Numer. Anal. 40*(5), 1605–1631.

Milhorat, T. H., R. M. Kotzen, and A. P. Anzil (1994). Stenosis of central canal of spinal cord in man: incidence and pathological findings in 232 autopsy cases. *J Neurosurg 80*, 716–722.

Nicholson, C. (2001). Diffusion and related transport mechanisms in brain tissue. *Rep. Prog. Phys 64*, 815–884.

Nield, D. A. and A. Bejan (2006). *Convection in Porous Media* (third ed.). Springer Science+Business Media, Inc.

Oldfield, E. H., K. Muraszko, T. H. Shawker, and N. J. Patronas (1994). Pathophysiology of syringomyelia associated with chiari i malformation of the cerebellar tonsils. *J Neurosurg 80*, 3–15.

Philip, J. R. (1956). Transient fluid motions in saturated porous media. *Australian Journal of Physics 10*, 43–53.

Quigley, M. F., B. J. Iskandar, M. A. Quigley, M. N. Nicosia, and V. Haughton (2004). Cerebrospinal fluid flow in foramen magnum: Temporal and spatial patterns at MR imaging in volunteers and in patients with Chiari I malformation. *Radiology 232*, 229–236.

Roldan, A., O. Wieben, V. Haughton, T. Osswald, and N. Chesler (2009). Characterization of CSF hydrodynamics in the presence and absence of tonsillar ectopia by means of computational flow analysis. *Am. J. Neuroradiol. 30*, 941–946.

Saffman, P. G. (1973). On the boundary conditions at the interface of a porous medium. *Studies in Applied Mathematics 1*, 93–101.

Shah, S., V. Haughton, and A. M. del Rio (2011). CSF flow through the upper cervical spinal canal in Chiari I malformation. *Am J Neuroradiol 32*, 1149–53.

Smith, J. H. and J. A. C. Humphrey (2007). Interstitial transport and transvascular fluid exchange during infusion into brain and tumor tissue. *Microvascular Research 73*, 58–73.

Støverud, K.-H., K.-A. Mardal, V. Haughton, and H. P. Langtangen (2011). CSF flow in Chiari I and syringomyelia from the perspective of computational fluid dynamics. *The Neuroradiology Journal 24* (20-23).

Valen-Senstad, K., K.-A. Mardal, A. Logg, H. Narayanan, and M. Mortensen (2011). A comparison of some finite element schemes for the incompressible Navier–Stokes equations. In A. Logg, K.-A. Mardal, and G. N. Wells (Eds.), *Automated Scientific Computing*, Chapter 19. Springer-Verlag.

Whitaker, S. (1986). Flow in porous media I: A theoretical derivation of Darcy's law. *Transport in porous media 1* (1), 3–25.

White, F. M. (2008). *Fluid Mechanics* (sixth ed.). McGraw-Hill.

Xie, X., J. Xu, and G. Xue (2008). Uniformly-stable finite element methods for Darcy-Stokes-Brinkman models. *J. Comput. Math 26* (3), 437–455.

Yasui, K., Y. Hashizume, M. Yoshida, T. Kameyama, and G. Sobue (1999). Age-related morphologic changes of the central canal of the human spinal cord. *Acta Neuropathol 97*, 253–259.